2011

Use of Innovative Computer Technology and Optical Texture Properties in the Analysis of Pavement Digital Images

Saumya Priyadari Amarasiri
University of South Florida, samarasi@mail.usf.edu

Use of Innovative Computer Technology and Optical Texture Properties in the Analysis of Pavement Digital Images

by

Saumya Priyadari Amarasiri

A dissertation submitted in partial fulfillment
of the requirements for the degree of
Doctor of Philosophy
Department of Civil and Environmental Engineering
College of Engineering
University of South Florida

Co-Major Professor: Manjriker Gunaratne, Ph.D.
Co-Major Professor: Sudeep Sarkar, Ph.D.
Dmitry Goldgof, Ph.D.
John Lu, Ph.D.
Kandethody Ramachandran, Ph.D.
Qing Lu, Ph.D

Date of Approval:
May 20, 2011

Keywords: Computer Vision, Texture, Cracks, Wear, Modeling, BRDF

ACKNOWLEDGEMENTS

I profusely thank Dr. Gunaratne for his guidance and the extension of knowledge in making this work a reality. He was a great mentor. Also I thank Dr. Sarkar for his knowledge and intuition in Computer applications in Civil Engineeering. The efforts of Ms. Catherine Burton of Dean's office are very much appreciated. I also thank all my fellow graduate students.

TABLE OF CONTENTS

LIST OF TABLES

LIST OF FIGURES

ABSTRACT

Digital image based automated pavement crack detection and classification technology has seen vast improvements in the recent years. In spite of these developments, although pavement crack lengths and widths can be evaluated using state-of-the-art software with a reasonable accuracy, no reported evidence is found in extending this technology to evaluate crack depths. Hence a preliminary study was carried out to model the digital image formation of cracked concrete pavements based on the Bidirectional Reflection Distribution Function. It was revealed that a definitive theoretical relationship exists among the crack widths and depths and the maximum pixel intensity contrasts in the images of cracks. The above relationships fortified by appropriate calibration were verified using actual crack data not used in the calibration that can be useful in predicting crack depths. Secondly, a number of innovative techniques in computer vision such as image characterization using quantification of optical texture properties of images and a number of widely used optical texture related techniques for characterization of digital images which have not been exploited adequately in pavement evaluation, were introduced highlighting their useful applications in pavement evaluation. One such application, the automated and accurate detection of correspondences in progressive images of the same pavement captured during different times, would be essential for close monitoring of cracks or wear at the project-level. Two reliable methods for determining correspondences among pavement images illustrated in this work are; (1) texture masking and minimum texture distance method applicable to locations with no

significant distress, and (2) homogeneous coordinates based geometrical matching and the maximum texture distance to detect the locations of distress and be applied to detect exact locations of crack propagation and excessive pavement wear. Thirdly, the BRDF based pavement image formation model revealed that quantifiable changes in the *brightness* of images occurs due to pavement wear-related changes in texture depth and spacing (wavelength). The traffic induced pavement wearing process was simulated by gradual smoothening of the modeled surfaces and then images corresponding to each wearing stage were generated. The theoretically predicted variation of the image *brightness* due to wear was experimentally verified using images from a gradually worn out concrete specimen. Finally it was illustrated how the *brightness* evaluation of wheel path images has the potential to be a screening tool to monitor the degradation of macrotexture and hence the skid-resistance of pavements at the network level.

CHAPTER 1: INTRODUCTION

Digital image-based automated pavement evaluation has been gradually replacing the manual pavement evaluation due to its improved efficiency and operational safety. Automated pavement evaluation implemented in real-time or post-processing of digital images of asphalt or concrete pavements has become a routine practice in many transportation agencies worldwide (Cheng et al., (1999), Huang and Xu (1996), Lee and Kim (2005), Wang (2007)). Typical evaluation vehicles include an exterior line-scan camera that captures grayscale images of the pavement and a computer mounted inside the vehicle for acquisition, storage and analysis of the captured images. The grayscale images are composed of individual pixels having intensity values in the range of 0 to 255, representing colors from black to white respectively. A lighting system attached to the rear bumper of the survey vehicle provides adequate illumination for acquisition of images irrespective of natural lighting. In more recently developed imaging vehicles, the lamp-based artificial illumination has been replaced by laser lights to overcome the issues of non-uniform illumination and shadows (National Optical Institute, 2008).

When digital pavement images are processed, a pixel intensity contrast is observed at cracks with the intensities inside the crack being significantly lower compared to the outside, if the cracks are not filled with sand or clay. The consequent color contrast is exploited in automated state-of-the-art pavement evaluation software to identify cracks. Automated assessment of the extent and severity of cracks based on the respective

evaluation of crack lengths and widths, becomes a useful input to pavement condition evaluation.

1.1 Research Objectives

Assessment of crack depths would be useful in determining rehabilitation strategies and when it is required to identify milling depths for asphalt pavement resurfacing projects, since engineers depend on pavement core samples. Digital image-based evaluations reach well short of evaluation of depth of cracks. It is believed that if the image formation process is modeled using appropriate optics it would lead to the revelation of even more useful information such as shallow crack depths, from the digital images. It was unable to locate any published literature where attempts have been made to model the formation of digital images of cracked or jointed pavements using principles of optics. Theferefore, the first objective of this research is to model the image formation procedure to uncover the relationship between crack depths and the intensity contrast between cracks and uncracked pavement.

The second research objective is based on the realization that although the application of optical texture differentiation techniques is scarce in pavement evaluation literature, the established optical texture analysis techniques may be used effectively in monitoring small-scale texture changes in pavement sections of interest. If a sequence of images is collected under the same scale and orientation, and the changes in texture between the images of the location of interest at two conditions are relatively low compared to the texture difference between the images of that location and non-corresponding locations,

then texture similarity measures can be used for correspondence of a sequence of images. If the sequence of images is collected under different resolutions, there is noticeable wander of the vehicle resulting in deviations in orientation, or the changes in texture exceed a threshold limit, then an alternative non-optical method; the method of homogeneous coordinates, can be used for correspondence.

Presently the wet skid-resistance of localized areas of highway pavements is evaluated by the Locked-wheel Skid-Tester (LWST) at a slip speed of 65 km/hr (ASTM E 274-06), while the Runway Friction Testers (RFT), Grip testers and mu meters are employed to evaluate the wet skid resistance continuously over selected runway sections at designated slip speeds. Since the wet friction estimates vary from one device to another, the "spot-measuring" and relatively precise Dynamic Friction Tester (DFT) is considered to provide the standard friction values at a slip speed of 60 km/h (ASTM 1911-09a). However, neither of the above devices can be used for rapid screening of pavements for skid resistance deficiencies at the *highway network level*. The above need can only be addressed with techniques that can monitor the continuous changes in skid-resistance along an entire pavement network based on evaluating the degradation of its macro-texture in particular. Alternatively, the digital images of a pavement embody the entire set of 3-D macrotexture parameters that characterizes wet skid-resistance of a pavement and the pixel intensity contrasts due to contaminants. Therefore, the analysis of optical properties embedded in pavement images can reveal both attributes of reduced skid-resistance; i.e degradation texture and contamination. The third objective of the

dissertation research is related to the potential of using appropriately calibrated images of wheel paths to predict the corresponding changes in macro-texture and skid resistance.

1.2 Literature Review

In published research, analysis related to processing of digital images has been focused mostly on automated detection of type, extent and severity of cracks (Ayenu-Prah and Attoh-Okine, 2008, Chou and Cheng, 1994, Huang and Xu, 2006, Lee and Kim, 2005, Liu et al., 2008, Wang, 2000). Since the current state-of-the-art of automation in crack analysis has proven to be satisfactory mostly for quality assurance of network-level crack evaluations and warranty project-level general crack evaluations (Gunaratne et al., 2008), extensive and vigorous research is being conducted to further advance the frontiers of distress evaluation through innovative techniques. Use of fuzzy sets (Cheng et al., 1999), neural networks (Cheng et al.,2001), stereovision (Wang, 2007), wavelet transform (Zhou et al.,2006), and Finite Ridgelet Transform (Gang et al.,2007) are some such innovations.

Complex algorithms with high levels of computing power are required for most automated crack type determination and crack evaluation systems. Nonetheless, most automated crack type determination systems as well as evaluation systems have not provided accurate results acceptable to public highway agencies. Hence, currently there is no automated crack evaluation system that can be adopted as part of a national standard. Many offline image processing techniques such as digital filters, adaptive thresholds, and expert systems can be readily found in the literature (Huang and Xu , 2006).

A crack type index (CTI) was developed by Lee and Kim (2005) to identify the crack

types as longitudinal, transverse, and alligator cracks using tiles. A tile is defined as a sub-image of a whole digital image and the CTI is based on the vertical and horizontal spatial distribution of image tiles rather than image pixels. Block cracks and multiple cracks were validated by combining the CTI method with an existing index called the Unified Crack Index (UCI).

It is possible to measure crack quantities rapidly from the tile-based computation because it significantly reduces the computational complexity over pixel-based computation. Also, when there is a significant degree of noise in the pavement image, a pixel-based approach would produce unreliable results. In addition, since isolated crack pixels will be ignored as background noise, the tile-based UCI system would be relatively stable. Each pixel is binarized by applying this threshold value to each tile. A tile is considered as a crack tile if the percentage of crack pixels in a tile is greater than another predefined threshold value. Finally, the UCI is calculated by dividing the number of crack tiles by the total number of tiles of the entire image.

An image processing algorithm customized for high-speed, real-time inspection of pavement cracking was presented by Huang and Xu (2006). A pavement image is divided into grid cells of 8x8 pixels, and each cell is classified as a noncrack or crack cell using the grayscale information of the pixels bordering the grid. Whether a crack cell can be regarded as a basic element (or seed) depends on its contrast with the neighboring cells. If they fall on a linear string, a number of crack seeds can be called a *crack cluster*. A crack cluster is a dark strip in the original image that may or may not be a part of a real crack.

Additional conditions to verify a crack cluster are the contrast, width, and length of the strip.

Automated real time crack analysis based on fuzzy logic, and fuzzy set theory was proposed by Cheng et al. (1999). In this analysis, a sample space reduction and interpolation approach was used to determine the threshold pixel intensity values for crack detection in pavement images, rapidly and accurately. There are three stages in the procedure of determining the threshold values. The first is to create the original sample space by collecting a large number of pavement images. Second, the sample space is reduced to achieve a faster rate of processing. Finally, the threshold value of a pavement image is estimated by applying the proposed thresholding approach to the reduced sample space.

Wang (2000) has developed a real time image processing software called Automated Distress Analyzer (ADA) that analyzes pavement images. This software is separated into two parts. One part of the software analyzes cracks such as longitudinal, transverse, block and alligator cracking. The other software analyzes distresses such as rutting and roughness. The images of the pavement surface are obtained by using two simultaneous cameras, each with a resolution of 1300 x 1024. Then the two images are interlaced to combine them to form a single image. The real time distress data is produced using the computing facilities on board the data vehicle and multimedia databases are generated. The speed of collection and analysis of data is above 60 mph. The three protocols used to analyze multipass data sets of pavement images from a roadway section are, (1) the

AASHTO interim distress protocol (AASHTO, 2001), (2) the World Bank's Universal Cracking Indicator (CI) (Peterson and Uddin, 1994), and the (3) Texas Department of Transportation's (TxDOT) method.

A novel approach was presented by Chou et al. (1994) to apply moment invariants of distress and neural networks to analyze pavement images. Once features are obtained by calculating moment invariants from different types of distress, back propagation neural network is used to classify them. In this method, the quality of images is determined by the illumination in addition to the object's reflectance. Pavement image processing is improved by using fuzzy image processing methods. Moment invariants under changes of size (scale), position (translation), and orientation (rotation) extracted from cracks' features are used to better classify the cracks.

Also interactive crack detection software that incorporates both automated and manual crack detection algorithms have been developed. When the images are loaded onto this software, the type of pavement surface as well as the types of distresses should be specified. When a crack is observed in the image, the user must first decide the type of crack, on a manual basis. Once the type and severity are specified, the length of the crack is specified by dragging the mouse along that crack. Then the software automatically determines the extent of the crack on an automatic basis.

Evaluation of crack depths plays an important role in pavement management systems. Although automated digital image analysis has been mostly focused on crack detection,

in literature methods of automated crack depth detection based on digital images could not be found. However in a study by Mei et al. (2004) neural networks were used to estimate the depths of shallow cracks in asphalt pavements automatically and dynamically without destructing the pavement structure. In this method a laser measurement unit is used to collect crack geometry data and a neural network is used to map crack depth, crack opening geometry and other pavement parameters.

Skid resistance on pavements is also an important issue in pavement management systems. It was found that the specific influence of pavement texture on skid-resistance and tire wear has been investigated by Britton et al. (1974), Leu and Henry (1978) and Balmer (1978). Consequent to the above studies, a single model correlating skid resistance to both macrotexture and microtexture evaluations was first introduced by Leu and Henry (1978). More recently, Gendy and Shalaby (2007) found that the complete characterization of skid resistance must involve all three attributes; size, spacing and shape of both macrotexture and microtexture. Microtexture which can be detected indirectly in the field by the British Portable Skid Tester (BPT) (ASTM E303-93) governs the dry friction produced by adhesion at low tire speeds. On the other hand, macrotexture produces hysteresis friction at high tire speeds and in addition reduces the possibility of hydroplaning by facilitating the drainage of water. Macrotexture can be evaluated using the mean texture depth (MTD) or the mean profile depth (MPD) (ASTM E 1845-01). Although state-of-the-art laser profiling techniques (LRIS,2008) can provide accurate evaluations of pavement macrotexture, laser evaluations can become unreliable due to contamination. In the literature, only one laser system (DSC 111,2008) is reported

to have the capability to distinguish contaminants such as water, frost, snow, slush and black ice from pavement material.

1.3 Description of Dissertation Chapters

In the second chapter of the dissertation the modeling of crack and joint depths using digital images are discussed. The Ward's reflection model which is described in this chapter is used to relate optical reflection properties to correlate image intensities to crack and joint depths. The objectives of the study documented in this chapter are to (Huang and Xu, 2006) model the intensity contrast at cracks and joints using reflection properties of the intact pavement surface and cracks, and (Lee and Kim, 2005) use the model to predict depths of cracks, joints and other irregular features to distinguish each feature.

The objectives of the third chapter are to identify optical texture characterization features that are relevant to pavement images, use texture similarity measures and homogeneous coordinates for correspondence of a sequence of images and investigate the applicability of the above techniques in monitoring pavement wear as well as widening and elongation of cracks, at the project-level.

In the fourth chapter of this dissertation, the Ward' reflection model is used again to model macrotexture and wear of concrete pavements with time. Theoretical simulations were performed and experimentally verified using actual images of concrete sections.

CHAPTER 2: MODELING OF CRACK AND JOINT DEPTHS IN DIGITAL IMAGES OF CONCRETE PAVEMENTS USING OPTICAL REFLECTION PROPERTIES

2.1 Modeling of Pavement Surface Radiance

2.1.1 Reflection Properties of Surfaces

Light incident on a surface could reflect completely in the opposite direction as dictated by the law of reflection or scatter in many directions. Surfaces where light reflection is solely in the opposite direction are known as *specular* surfaces while *diffusive* surfaces reflect light in all directions including the specular direction. Generally most surfaces have both specular and diffusive properties, reflecting light in all directions but more so in the specular direction. The reflection properties of a pavement surface depend on the texture of the surface determined by the constituents of the pavement mix and the surface geometry. Hence the reflection properties can be used to model the unique characteristics of pavement surfaces including their distress features.

2.1.2 Bidirectional Reflection Distribution Function (BRDF)

The intensity of light reflection (radiance) from any point on a surface in the direction of the camera depends on the intensity of incident light (irradiance), the local reflectance properties and the orientation of the surface at that point to the direction of incidence. The complex relationship between the radiance and irradiance of a surface can be best described by the Bidirectional Reflection Distribution Function (BRDF). When the intensity and direction of the radiant light are known BRDF of the surface can be used to

determine the intensity of the light that reflects from the surface in any given direction. BRDF is defined as the ratio of radiance in a given direction $(\overline{R})$ to the irradiance on that surface from another direction $(\overline{I})$ (Ward, 1992) (Eqn. 1(a)).

$$BRDF(\overline{I},\overline{R}) = \rho(\overline{I},\overline{R}) = \frac{L_r(\overline{R})}{L_i(\overline{I})\cos\theta_i d\omega} \tag{1a}$$

where $L_r(\overline{R})$ is the radiance (reflected flux per unit normal area per unit solid angle)

$L_i(\overline{I})$ is the irradiance (incident flux per unit normal area per unit solid angle)

θ_i is the polar angle between the incident vector and the surface normal

$d\omega$ is the solid angle subtended at the surface point by the incident light source

The *total* radiance at a point on the surface in the $\overline{R}$ direction due to all the light entering the hemisphere encompassing a solid angle of 2π surrounding that point can be expressed as,

$$L_r(\overline{R}) = \int_0^{2\pi} \rho(\overline{I},\overline{R}) L_i(\overline{I})\cos\theta_i d\omega \tag{1b}$$

Therefore in 3D, the above relationship is based on two incident and two reflected angles defining the directions $\overline{I}$ and $\overline{R}$ as expressed in Eqn. 2,

$$L_r(\theta_r,\phi_r) = \int_0^{2\pi}\int_0^{\pi/2} \rho(\theta_i,\phi_i;\theta_r,\phi_r) L_i(\theta_i,\phi_i)\cos\theta_i \sin\theta_i d\theta_i d\phi_i \tag{2}$$

where

ϕ_i is the azimuth angle of the incident vector projected on to the surface plane

θ_r is the polar angle between the reflected vector and the surface normal

ϕ_r is the azimuth angle of the reflected vector projected on to the surface plane

$L_r(\theta_r, \phi_r)$ is the reflected radiance (watts/steradian/meter^2)

$L_i(\theta_i, \phi_i)$ is the incident radiance (watts/steradian/meter^2)

$\rho(\theta_i, \phi_i; \theta_r, \phi_r)$ is the BRDF (steradian^{-1}) given by equation 1b

The most common functions that are used to represent BRDF of a surface are the tensor products of the spherical harmonics, Zernike polynomials, and spherical wavelets (Rusinkiewicz, 1998). However, most of the basic functions require a large number of coefficients to describe even moderately specular BRDFs. In addition, the above methods do not require any less storage even under isotropic BRDF conditions. Rusinkiewicz (1998) proposed a method for decomposing BRDFs by changing variables more efficiently. In the Rusinkiewicz (1998) transformation, the BRDF is represented as a half angle between incident and reflection directions, and the difference angle between the half angle and incident angle ($\bar{h}$ in Fig. 1). Kautz and McCool (1999) used single value decomposition (SVD) and normalized decomposition (ND) for the BRDF function. On the other hand, simplified models are also available for approximate evaluation of BRDF such as Phong (1975), He (1991), Cook and Torrance (1981), and Ward (1992) models.

2.1.3 Ward's Reflection Model for BRDF

In the work reported here, the Ward's reflection model (1992) is used due to its simplicity and physically meaningful parameters. Although Ward (1992) formulated reflection models for both anisotropic and isotropic surfaces, in this preliminary analysis the isotropic model given by Equation (3) has been assumed for simplicity.

$$\rho(\theta_i,\phi_i;\theta_r,\phi_r) = \frac{\rho_d}{\pi} + \rho_s \cdot \frac{1}{\sqrt{\cos\theta_i \cos\theta_r}} \cdot \frac{\exp\left[-\tan^2 \delta / \alpha^2\right]}{4\pi\alpha^2} \tag{3}$$

$$\bar{h} = d\bar{i} + d\bar{r} \tag{4}$$

where

ρ_d is the diffuse reflectance (steradian^{-1})

ρ_s is the specular reflectance (steradian^{-1})

δ is the angle between vectors $\hat{n}$ and $\hat{h}$ in Figure 1 ($\hat{n}$ is the unit normal to the surface, $\hat{h}$ is the half vector between the unit incident vector $d\hat{i}$ and unit reflection vector $d\hat{r}$ as illustrated and defined in Eqn. (4)).

α is the standard deviation of the surface slope or the square root of the slope variance.

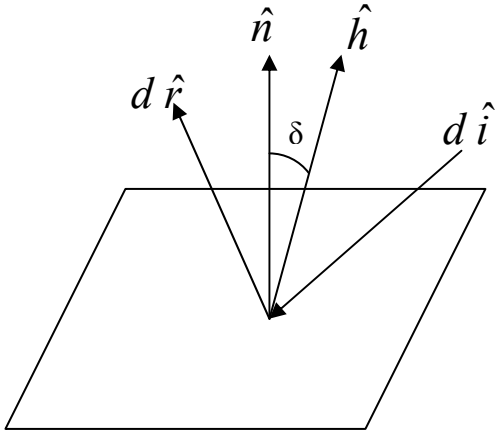

FIGURE 1 Illustration for Ward's Reflection Model

2.1.4 Selection of Surface Parameters for Ward's Model

The three dominant parameters in the Ward's reflection model (Eqn. 3) are ρ_d, ρ_s and α. The parameter α represents the randomness in the orientation of the tiny fractals that form the surface. Typically surfaces with relatively lower α values can be considered specular because smooth surfaces that are characterized by low slope variances (α) reflect

light mostly in the specular direction with much lower reflection components in the other directions. As α increases, more and more light reflects in the directions other than the specular direction and the surface assumes diffusive characteristics. Thus a very low but a non-singular α value as high as 0.0001 defines a surface with high specularity for all practical purposes, where as a relatively high value of 0.2 portrays a highly random fractal orientation and hence a diffusive surface. However, once a limiting high value of α is reached, one can expect the reflection to reduce in all directions due to obscurity and internal reflection caused by the interference from the surface profile itself. Although the parameter α could depend on both the macrotexture and the microtexture of a pavement, it is more sensitive to the microtexture.

On the other hand, the parameters ρ_s and ρ_d determine the respective magnitudes of the *total* specularity and the *total* diffusivity that are inherent to that surface. As seen in Eqn. (3) the specular component is assumed to be a Gaussian distribution with its standard deviation related to α. Typical values of ρ_d and ρ_s for different surfaces are reported in Ward (1992). However, the specific values of ρ_s, ρ_d, and α in the model are estimated based on comparing the model predictions to corresponding experimental data. *Gonioreflectometers* are commonly used to measure the BRDF of a given surface. It is recommended to use at least 2500 data points to sample BRDF at every 10^0 on isotropic surfaces and at least 100,000 data points to sample BRDF on non-isotropic surfaces (Joshi et al., 2007)**.** Marschner et al. (2000) presented an image based process for measuring the BRDF of a surface with an apparatus consisting of two cameras, a light source, and a test sample of known shape.

2.2 Modeling of the Image Intensity Variation Across Cracks

For modeling purposes a crack can be considered simply as a discontinuity with a V-shaped (triangular) cross-section on a homogeneous pavement surface. In the following formulation it is demonstrated how the contrast and the pixel intensity variation across the image of a pavement discontinuity can be modeled. In this formulation the light source attached to the rear bumper of the imaging vehicle is considered as a transverse *line light* source that provides uniform and continuous illumination. As the vehicle moves forward, the *line-scan* camera scans the pavement in a plane perpendicular to the direction of travel capturing the image of a strip of the entire width of the pavement at a given instant. This line strip is considered to be one pixel in width and completely illuminated by the above light source at the image capturing instant. As shown in Figures 2, 3 and 5, at any instant, the camera (C) only points to a single point (P) of the pavement when imaging the pavement. Hence it can be assumed that the pixel intensity corresponding to the image of P is due to the reflection from the incident illumination at P from the entire light source (L). Other assumptions made in this formulation are that (1) the heights of the light source and the camera are relatively larger than the crack depths, and (2) two cameras are used with each one pivoted immediately above each wheel path. These two assumptions ensure the maximum contrast to be obtained in the images of cracks and preclude the need to consider inter-reflection within the cracks.

2.2.1 Case 1 - Modeling the BRDF of Longitudinal Cracks

For this case, as shown in Fig. 2, the analysis can be performed in 2D assuming the cross-section of the crack to be invariant in the z (longitudinal) direction. Hence the z ($\bar{k}$) axis

that comes out of the paper is not shown in Fig. 2. The following vectors can be defined at any point P(*px,py*) with respect to illumination due to an element of length δx* of the light source at L(lx, h) where h is the height of the light source above the pavement.

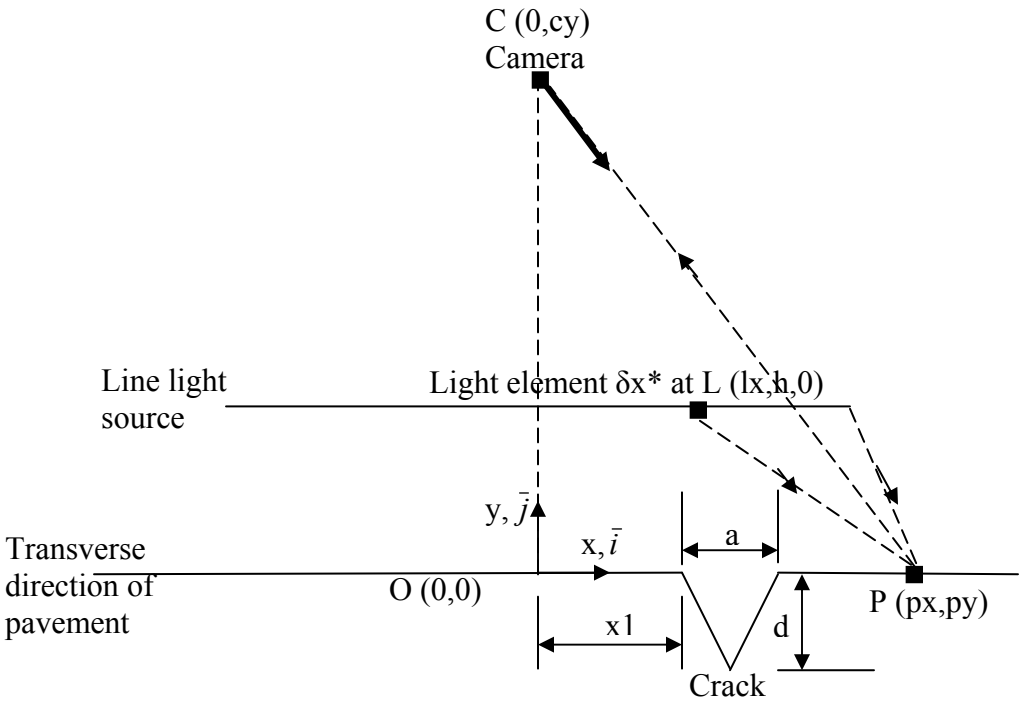

FIGURE 2 Configuration of the Radiance from a Longitudinal Crack

Incident vector, $\bar{I} = (px - lx)\underline{i} + (py - l)\underline{j}$ (5a)

Reflected vector, $\bar{R} = -(px)\underline{i} + (cy - py)\underline{j}$ (5b)

The following relationships are valid in the respective domains.

Outside the crack

$py = 0$ (6a)

Unit normal to the pavement surface, $\bar{n} = \underline{j}$ (6b)

Inside the crack

For $|x1| < |px| < |x1 + a/2|$

$$py = -\left|2\left(\frac{d}{a}\right)(px - x1)\right| \tag{7a}$$

$$\text{Unit normal, } \bar{n} = \frac{d}{\sqrt{d^2 + a^2/4}}\underline{i} + \frac{a/2}{\sqrt{d^2 + a^2/4}}\underline{j} \tag{7b}$$

For $|x1 + a/2| < px < |x1 + a|$

$$py = -\left|2\left(\frac{d}{a}\right)(|x1| + a - |px|)\right| \tag{8a}$$

$$\text{Unit normal, } \bar{n} = -\frac{d}{\sqrt{d^2 + a^2/4}}\underline{i} + \frac{a/2}{\sqrt{d^2 + a^2/4}}\underline{j} \tag{8b}$$

The above results can be used to obtain the variables θ_i, θ_r and δ (Eqn. (3)) for Case (1) as shown in the section on converting BRDF to pavement surface radiance (Eqns. (15a)-(15c)).

2.2.2 Case 2 - Modeling the BRDF of Transverse Cracks

Since the geometry of a transverse crack varies along transverse planes perpendicular to the travel direction where both illumination and imaging occur, variations along the longitudinal direction (z) must be considered in this analysis.

The following vectors can be defined at any point P(*px,py,pz*) with respect to illumination due to an element of length δx* of the light source at L(lx, h).

$$\text{Incident vector, } \bar{I} = (px - lx)\underline{i} + (py - l)\underline{j} + (pz)\underline{k} \tag{9a}$$

$$\text{Reflected vector, } \bar{R} = -(px)\underline{i} + (cy - py)\underline{j} + (pz)\underline{k} \tag{9b}$$

The following relationships are valid in the respective domains.

Outside the Crack

$$py = 0 \tag{10a}$$

Unit normal to the pavement surface, $\bar{n} = \underline{j}$ (10b)

Inside the Crack

For $0 < pz < a/2$

$$py = -2\left(\frac{d}{a}\right)z \tag{11a}$$

$$\bar{n} = \frac{a/2}{\sqrt{d^2 + a^2/4}}\underline{j} + \frac{d}{\sqrt{d^2 + a^2/4}}\underline{k} \tag{11b}$$

For $a/2 < pz < a$

$$py = -2\left(\frac{d}{a}\right)(a - z) \tag{12a}$$

$$\bar{n} = \frac{a/2}{\sqrt{d^2 + a^2/4}}\underline{j} - \frac{d}{\sqrt{d^2 + a^2/4}}\underline{k} \tag{12b}$$

The above results can be used to obtain the variables θ_i, θ_r and δ (Eqn. (3)) for Case (2) as shown in the section on converting BRDF to pavement surface radiance (Eqns. (15a)-(15c)).

Furthermore, in both Cases 1 and 2, provisions were made in the computer code *BRDFimage* that programmed the above analysis to account for the possibility of obscurity of some locations inside cracks with respect to the camera and the light source.

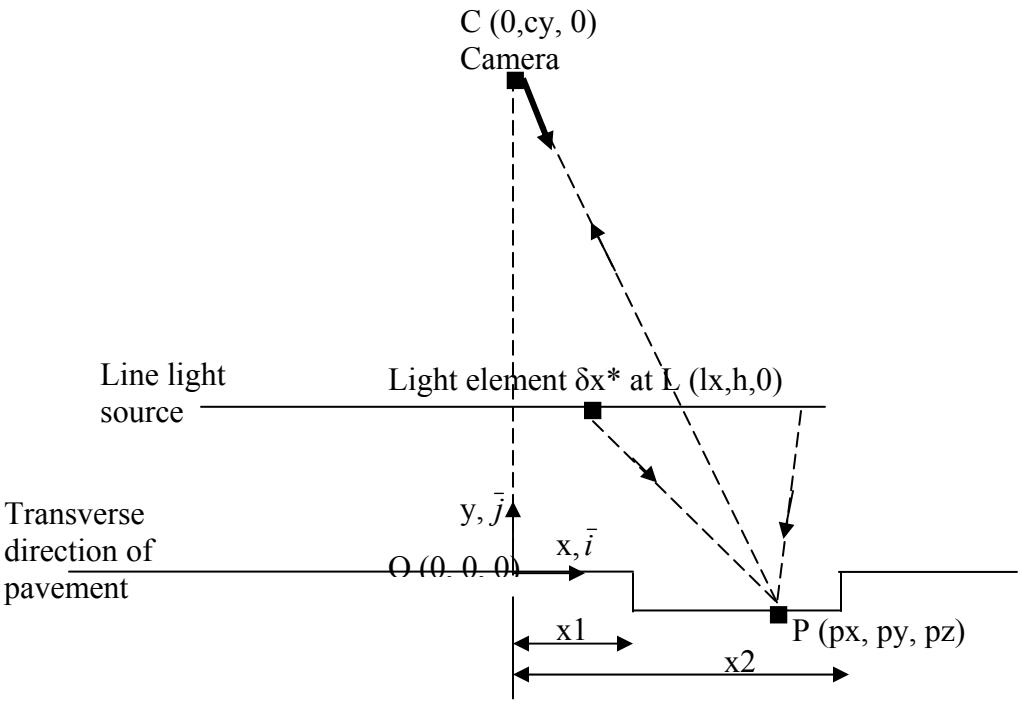

FIGURE 3 Configuration of the Radiance from a Transverse Crack

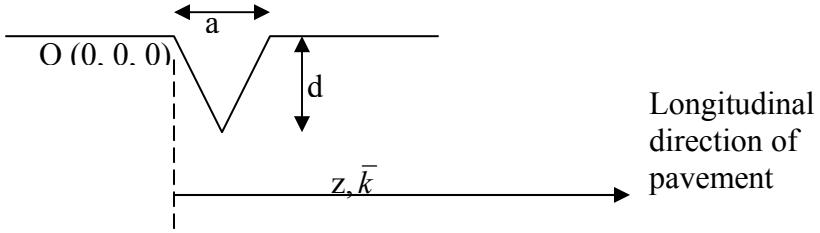

FIGURE 4 Cross-Sectional View of a Transverse Crack

2.2.3 Case 3 - Modeling the BRDF of Joints

The following vectors can be defined at any point P(*px,py,pz*) with respect to illumination due to an element of length δx* of the light source at L(lx, h)

Incident vector, $\bar{I} = (px - lx)\underline{i} + (py - l)\underline{j}$ (13a)

Reflected vector, $\bar{R} = -(px)\underline{i} + (cy - py)\underline{j}$ (13b)

The following relationships are valid in the respective domains.

Inside and outside the joint

$py = 0$ (14a)

Unit normal to the pavement surface $\bar{n} = \underline{j}$ (14b)

The above results can be used to obtain the variables θ_i, θ_r and δ (Eqn. (3)) for Case (3) as shown in the section on converting BRDF to pavement surface radiance (Eqns. (15a)-(15c)).

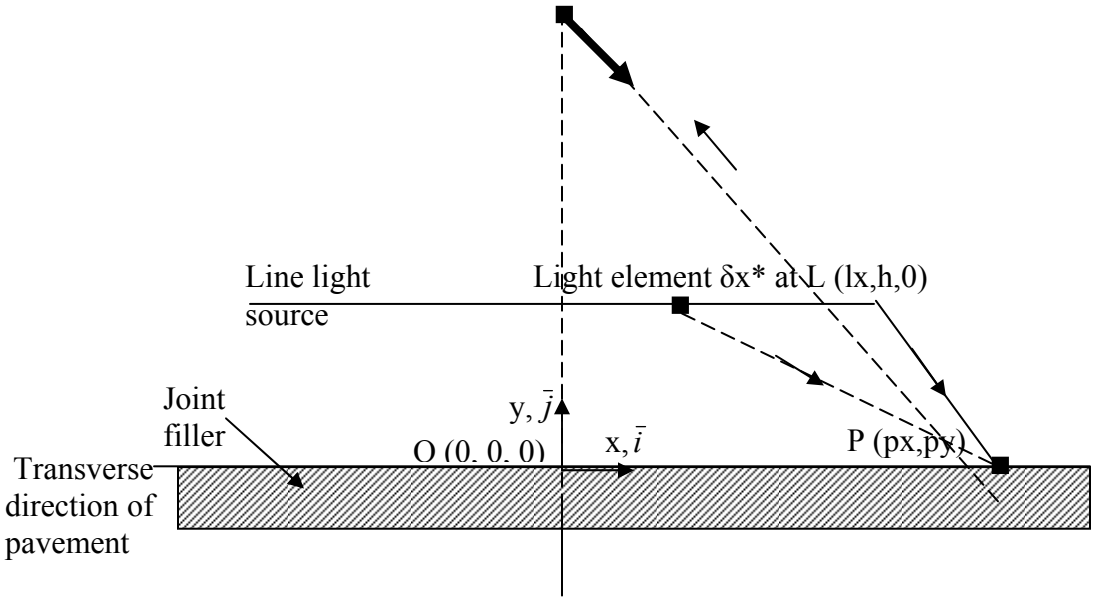

FIGURE 5 Configuration of the Radiance from a Joint

2.2.4 Conversion of BRDF to Pavement Surface Radiance

For all the above Cases (1)-(3), in relation to the Ward's model (Eqn. 3),

$\text{Cos } \theta_i = -\bar{I}.\bar{n}$ (15a)

$\text{Cos } \theta_r = \bar{R}.\bar{n}$ (15b)

$\text{Cos } \delta = (-\bar{I}/|\bar{I}| + \bar{R}/|\bar{R}|).\bar{n}/|-\bar{I} + \bar{R}|$ (15c)

Therefore, the BRDF ($\rho(px,py,pz)$) on the pavement surface and the crack surfaces can be evaluated by substituting from Eqn. (15) in Eqn. (3). Finally, the radiance of P can be determined from Eqn. (1b) using the following additional relationships. It can be seen from Fig. 6 that the solid angle subtended at P by the light source element δx* at L(lx, h) is given by (normal component of area/square of distance)

$$\delta\omega = \frac{[b(\delta x^*)]\cos\theta_L}{D^2} \tag{16a}$$

$\cos\theta_L = \bar{I}.\bar{k}$

where

θ_L is the angle between the line light source and the normal to the incident light vector

δx* is the considered length of the light source element at L(lx, h)

D is the distance LP

b is the width of line light source

If the light intensity attenuation is assumed to be inversely proportional to the distance, then from Fig. 6 it can also be seen that

$$L(\bar{I}) = \frac{h^2 L^*}{D^2} \tag{16b}$$

L* is the irradiance at the point Q on the pavement immediately underneath the light source. Finally, by substituting from Eqns. (16a) and (16b) in Eqn. (1b),

$$L_R(px, py, pz) = \int_{-l/2}^{l/2} \rho(px, py, pz, x^*).\frac{h^2 L^* \cos\theta_i}{D^2}.\frac{[b(dx^*)]\cos\theta_L}{D^2} \tag{16c}$$

where l is the total length of the light source.

2.2.5 Conversion of Pavement Radiance to Image Intensities

The image of a pavement feature is formed when the light reflected from that feature (object) enters the camera lens (aperture) and is refracted to the CCD sensor. A schematic diagram of the optics of image formation is shown in Figure 6. The relationship between the radiance from any given object on the surface of the pavement and the intensity of the image can be expressed using the following formulation.

The parameters f, d_c and D_c are the focal length, aperture diameter and the distance between the camera center and the imaged point (P) respectively. δO is the area surrounding P from which light is reflected to the corresponding area δI of the image.

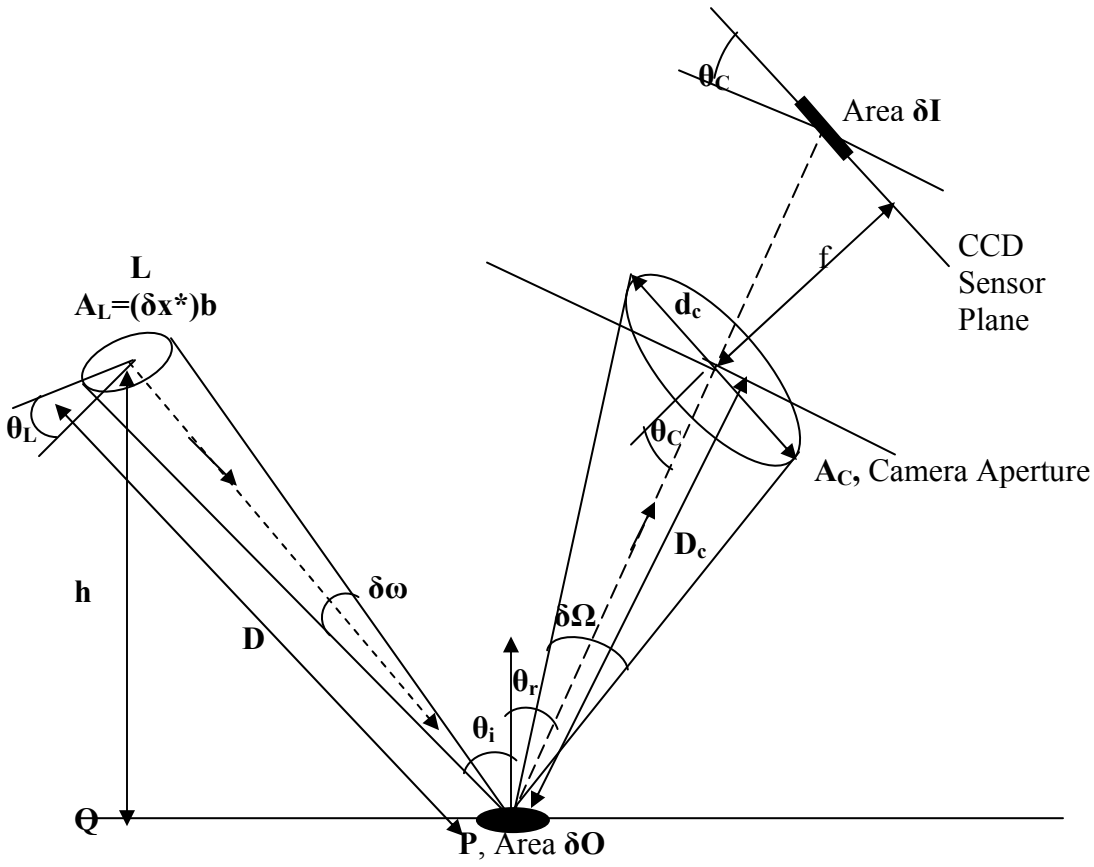

FIGURE 6 Illustration of the Image Formation Process

The flux leaving the pavement surface area δO toward the camera is given by

$$F = L_R \delta O \delta\Omega \tag{17}$$

where L_R is the radiance at δO

$$\delta\Omega = A_c \frac{\cos\theta_r}{D_C{}^2} \tag{18}$$

A_C is the area of the camera and $D_c = |\overline{R}|$ (from Eqns. (5b), (9b) or (13b))

If it is assumed that there is no loss of photo energy at the camera, and the intensity at the image point δI is E, then

$$F = E.\delta I \tag{19a}$$

Substituting from Eqn. (19a) in Eqn. (17),

$$E\delta I = L_R \delta O \delta\Omega \tag{19b}$$

Using Eqn. (18), Eqn. (19b) can be rewritten as

$$E\delta I = L_R (\delta O) A_c \frac{\cos\theta_r}{D_C{}^2}$$

Or

$$E = L_R \frac{\delta O}{\delta I} A_c \frac{\cos\theta_r}{D_C{}^2} \tag{19c}$$

From basic optics it follows that the light originating from the object δO and passing through the center of the camera lens continues without refraction to form the image δI. Hence the solid angles subtended at the camera center O by δO and δI are equal and opposite. Then by evaluating each solid angle one obtains,

$$\frac{(\delta O)\cos\theta_r}{D_C{}^2} = \frac{(\delta I)\cos\theta_C}{(f/\cos\theta_C)^2}$$

Or

$$\frac{\delta O}{\delta I} = \frac{\cos^3 \theta_C . {D_C}^2}{f^2 \cos \theta_r} \tag{20}$$

where θ_C is the angle between the normal to the aperture of the camera and the reflected vector from point P. Substituting in Eqn. (19c) from Eqn. (20),

$$E = L_R . \frac{\cos^3 \theta_C}{f^2} . A_C \tag{21}$$

For a line-scan camera since θ_C is equal to zero because the camera is oriented toward the imaging location and A_c and f are constants, the intensity E of the image corresponding to the surface point P is proportional to the radiance of P (or L_R). Hence it can be deduced that Eqn. (16c) itself can be used conveniently to model the relative pixel intensities in a pavement image.

2.3 Analysis of Model Predictions

In the theoretical simulation of the image formation, the line light source and the camera were assumed to be 4 ft and 9 inches respectively above the pavement surface. The widths (a) and depths (d) of the modeled cracks were selected in the ranges of 1 mm to 10 mm, and 0.5 mm to 20 mm respectively encompassing the ranges of corresponding values for most *shallow* cracks found in concrete pavements. Typical ρ_d, ρ_s and α values (Ward, 1992) were used in the reflection model for the intact pavement surface as well as cracks and joints. The relatively high roughness inside cracks and joints due to the high variability in the orientations of surface fractals requires higher ρ_d and α values to be assumed inside cracks and joints compared to the respective values of the neighboring

pavement surface areas. The main objective of the image model calibration is to establish two specific average sets of values for the parameters ρ_d, ρ_s and α for a given pavement surface and a considered type of shallow cracks on it.

For a given crack width, as the depth of the crack increases the illumination of the tip of the crack decreases due to lower amount of light reaching it and hence the minimum intensity within the crack, which occurs at the tip, decreases. This results in an increased image pixel intensity reduction (contrast) between the outside and the tip of the crack for higher crack depths. The formulated model can be used to observe the variation of the pixel intensity reduction from the outside to the tip of the crack (i.e. the maximum pixel intensity drop in the crack) with the depth, for different crack widths. For two selected sets of ρ_d, ρ_s and α values from Table 1; (0.6, 0.4 and 0.1) for the uncracked surface and (0.8, 0.2, and 0.2) for the surface inside a longitudinal crack, this variation is shown in Figure 7. During the simulation the intensity outside the crack is assumed to be 170 in the gray scale range of 0-255, based on average measurements of intensities on the pavement surface at the given lighting conditions. It can be observed from Figure 7 that for all crack widths ranging from 1 to 10 mm, the reduction in intensity reaches a limiting value when the depth of the crack tip is approximately twice the width of the crack. It must be noted that, theoretically, the limiting value of the maximum reduction in pixel intensity $(\Delta I_{max})_{ult}$ must be equal to the pixel intensity of the uncracked surface (170 in this case) corresponding to the scenario of zero pixel intensity at the crack tip. However, the family of curves in Fig. 7 reaches limiting values between 140 and160 at finite crack depths.

TABLE 1 Ranges of Optical Parameters for Pavements

Location	Ward's Reflection Parameters		
	ρ_d (steradians^{-1})	ρ_s (steradians^{-1})	**A**
Uncracked Pavement Surface	0.5-0.8	0.2-0.5	0.1-0.2
Inside Cracks	0.7-0.9	0.1-0.3	0.1-0.2
Inside Joints	0.5-0.9	0.1-0.5	0.1-0.2

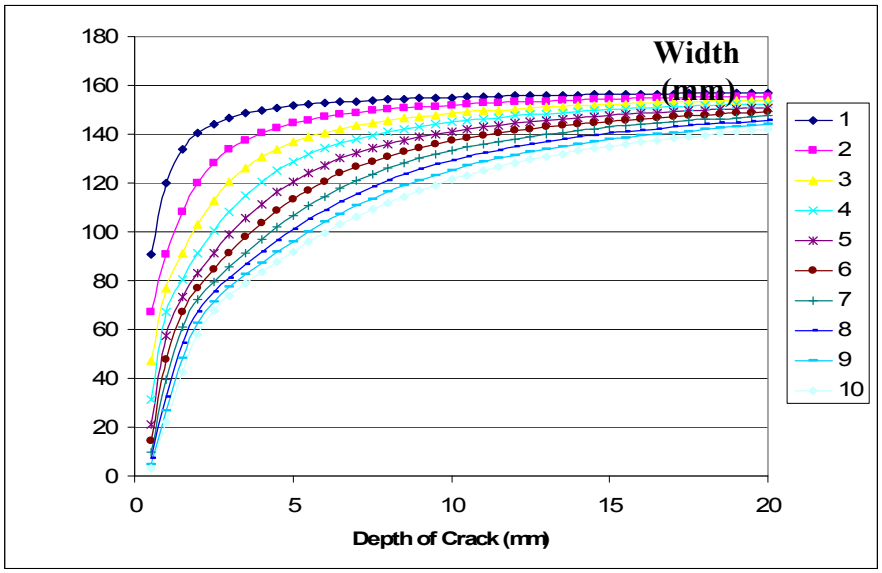

FIGURE 7 Maximum Pixel Intensity Reduction Vs the Depth for Longitudinal Cracks Predicted by the Reflection Model

It can also be noted in Figure 7 that the initial slope (*f(a)*) depends on the width of the crack (*a*). Therefore, in order to develop an equation for the family of curves shown in Figure 7 the relationship between the initial slope and the crack width can be expressed by Equation 22.

$$f(a) = ka^m \tag{22}$$

where k and m are parameters governed by the optical properties of ρ_s, ρ_d and α of the intact surface and the cracks. The logarithmic form of Equation (22) can be expressed by Equation (23).

$$\ln(f(a)) = \ln(k) + m\ln(a) \tag{23}$$

Figure 8 shows the plot of Equation (23) corresponding to data in Figure 7. One remarkable finding of the analysis is that the selected format (Eqn. 22) to express the initial slope of such families of curves for both longitudinal and transverse cracks consistently produced high R^2 values for any selected set of ρ_d, ρ_s and α values. When the values of k and m are determined from the intercept and slope of the fitted line in Figure 7, Equation (22) can be rewritten as,

$$f(a) = 366a^{-0.97} \tag{24}$$

When the initial slopes are expressed analytically (Eqn. 22) the family of curves in Figure 7 can be modeled using the following hyperbolic relationship based on the constant ultimate intensity difference $(\Delta I_{max})_{ult}$ reached by the curves.

$$\Delta I_{\max} = \frac{d}{\frac{1}{f(a)} + \frac{d}{\Delta I_{\max})_{ult}}} \tag{25}$$

where d is the depth of the tip. Based on Figure 7 and Equation (24) the specific form of Eqn. (25) for longitudinal cracks for the selected sets of (ρ_d, ρ_s and α) can be given by,

$$\Delta I_{\max} = \frac{d}{\frac{a^{0.97}}{366} + \frac{d}{\Delta I_{\max)_{ult}}}} \tag{26}$$

A similar analytical procedure was adopted to model the variation of the maximum pixel intensity reduction in transverse cracks as well, with increasing crack depths. The family of curves (Figure 9) predicted by the reflection model corresponding to the selected set of ρ_d, ρ_s and α values can be expressed by,

$$\Delta I_{\max} = \frac{d}{\frac{a^{1.27}}{106} + \frac{d}{(\Delta I_{\max)_{ult}} - 55)}} + 55 \tag{27}$$

The above analytical development with respect to Figures 7 and 9 shows that the maximum pixel intensity reduction in a longitudinal or transverse crack predicted by theoretical simulation can be expressed using a simple mathematical format.

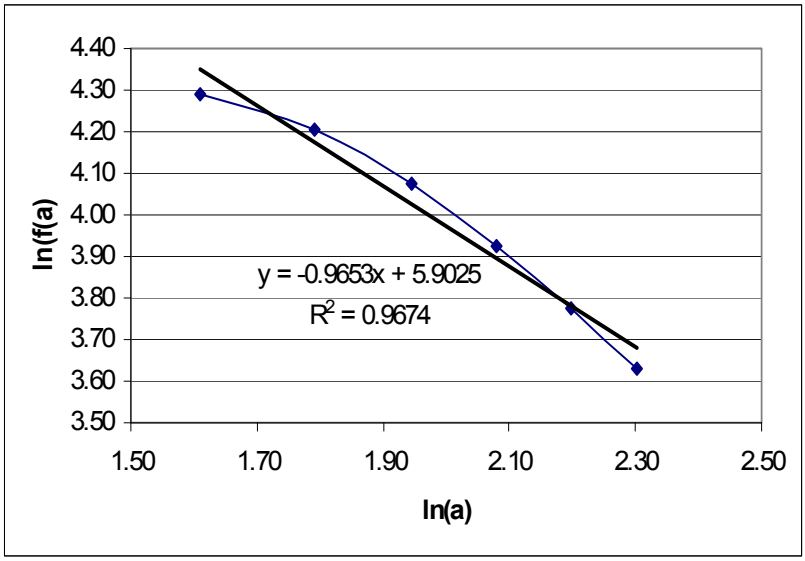

FIGURE 8 Plot of ln(f(a)) Vs ln(a) for Longitudinal Crack (Uncracked Area $\rho_d = 0.6, \rho_s 0.4$ and α =0.1, Inside Crack $\rho_d = 0.8, \rho_s 0.2$ and α =0.2)

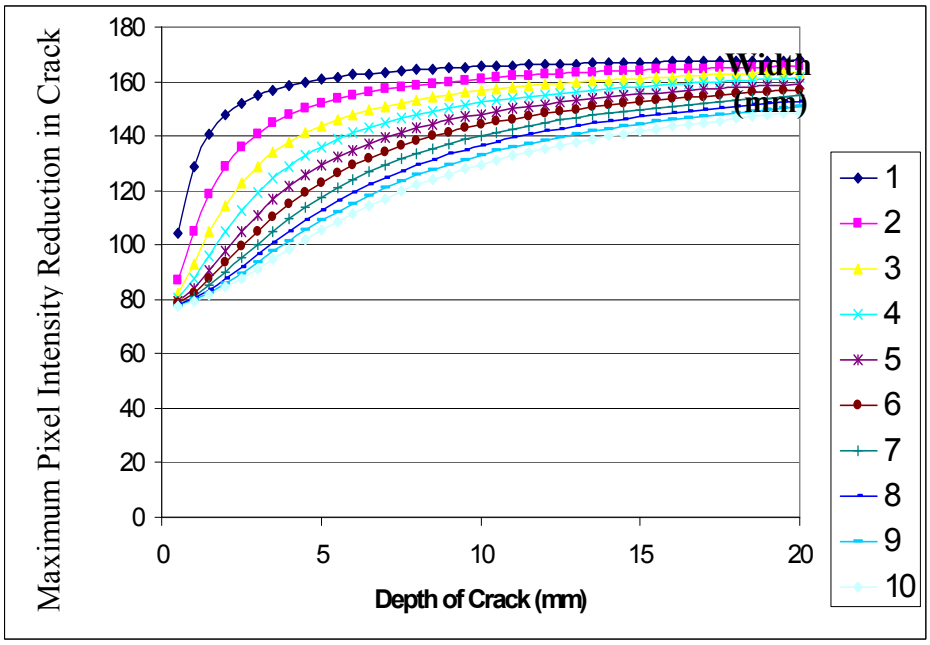

FIGURE 9 Maximum Pixel Intensity Reduction Vs the Depth for Transverse Cracks Predicted by the Reflection Model

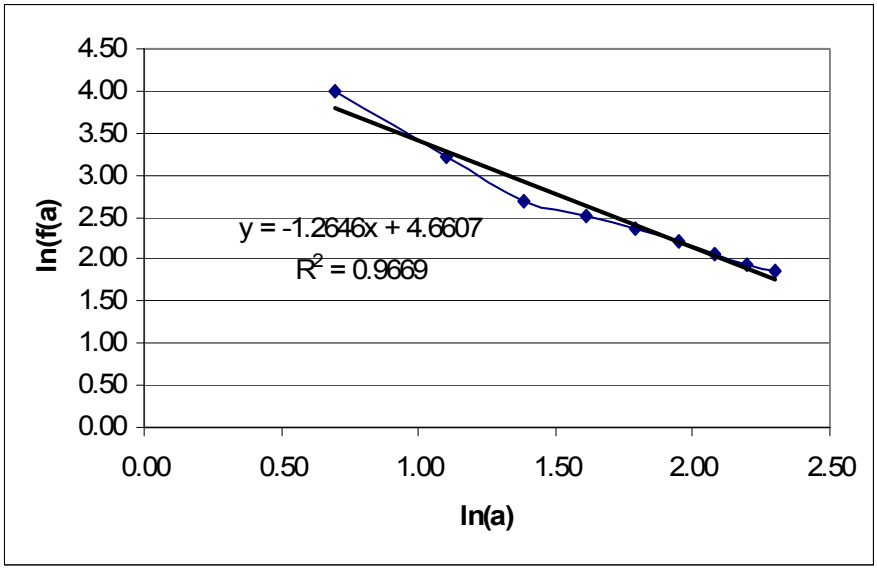

FIGURE 10 Plot of ln(f(a)) Vs ln(a) for Transverse Crack (Uncracked Area $\rho_d = 0.6, \rho_s 0.4$ **and** α **=0.1, Inside Crack** $\rho_d = 0.9, \rho_s 0.1$ **and** α **=0.2)**

2.4 Calibration of the Model

2.4.1 Experimental Setup

In order to calibrate the formulated reflection model (*BRDFimage*), the digital images of actual concrete pavement cracks with comparable dimensions were compared to digital images created using the above model. For this purpose, a surface was concreted and V-shaped cracks of desired dimensions were formed on it under regulated conditions before the concrete hardened. Crack widths and depths in the ranges of 1-10 mm and 0.5-20mm were selected to match the modeled cracks. Table 2 shows locations of the camera and the light source with respect to the 3D coordinate axis system in Figs 2, 3 and 5 in the experimental setup. In this study the optimum positions for the light source and the camera were selected (Table 2) to provide the highest contrast between the uncracked and cracked areas. When imaging a given crack it was placed at the origin of coordinates with the camera oriented toward it while the pavement surface was set to be in the x-z plane.

TABLE 2 Locations of the Camera, Light Source and the Crack with Respect to the Pavement Surface

Entity	Coordinates		
	X	Y	Z
Camera	0	229 mm	0
Line light source	-610 to +610 mm	1220 mm	-5 to +5 mm
Lowest point of crack	0	Depth of crack	0

The crack widths were measured using a Vernier caliper while crack depths were gauged using a thin wire. It must be noted that cracks and joints had to be artificially formed in this preliminary phase of the research such that *a/d* ratios could be regulated well and uniform conditions could be achieved along the cracks and joints. Uniformity was further ensured by smoothing the concrete surface with a sand paper. A sample of captured digital images of a longitudinal crack, a transverse crack and a joint are shown in Figures 11(a), 12(a) and 13(a) respectively.

2.4.2 Results of Model Calibration

Predictions of the maximum pixel intensity reduction for a number of modeled longitudinal and transverse cracks were selected from Figures 7 and 9 for comparison with those of the corresponding actual images. A sample of the modeled images is shown in Figures 11(b), 12(b) and 13(b) against their experimental counter-parts. In order to form a rational basis for comparison of the actual images and the corresponding modeled images, the intensities of the two sets of images (modeled and actual) were normalized with respect to the intensities of the immediate (uncracked) outside vicinity of the crack.

Then the pixel intensity distributions within the digital images of actual cracks were compared to those of the modeled images.

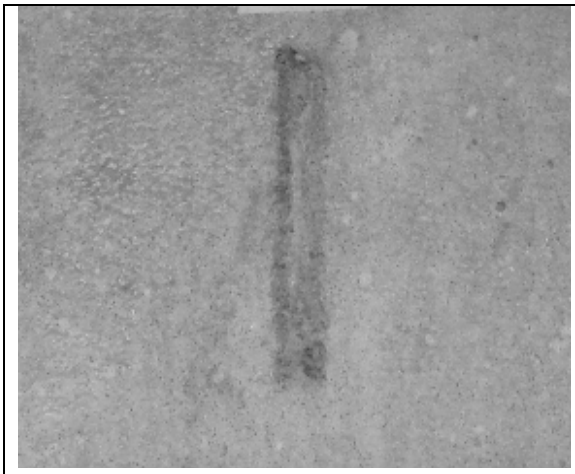

FIGURE 11(a) Digital Image of Longitudinal Concrete Crack a=5.4mm, d=2.5mm

FIGURE 11(b) Modeled Digital Image of the Crack in Figure 11(a)

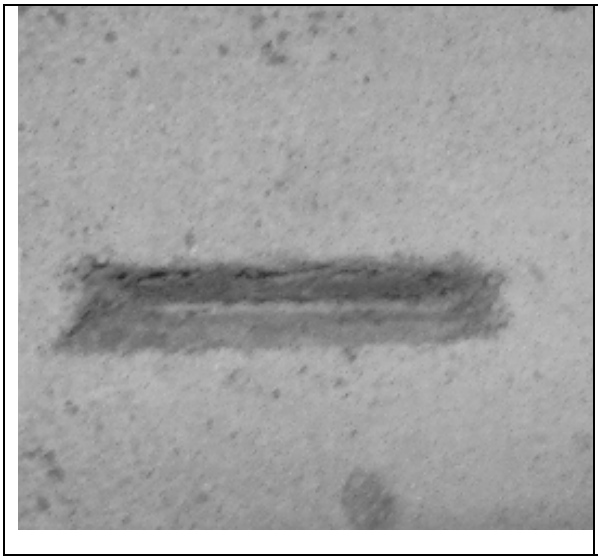

FIGURE 12(a) Digital Image of Transverse Concrete Crack a=9mm, d=7.3mm

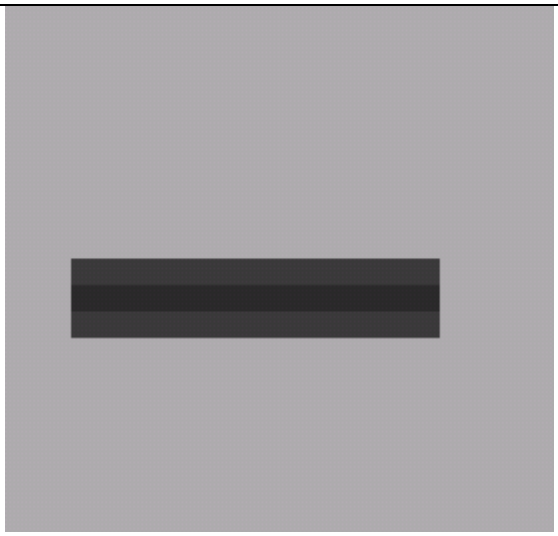

FIGURE 12(b) Modeled Digital Image of the Crack in Figure 12(a)

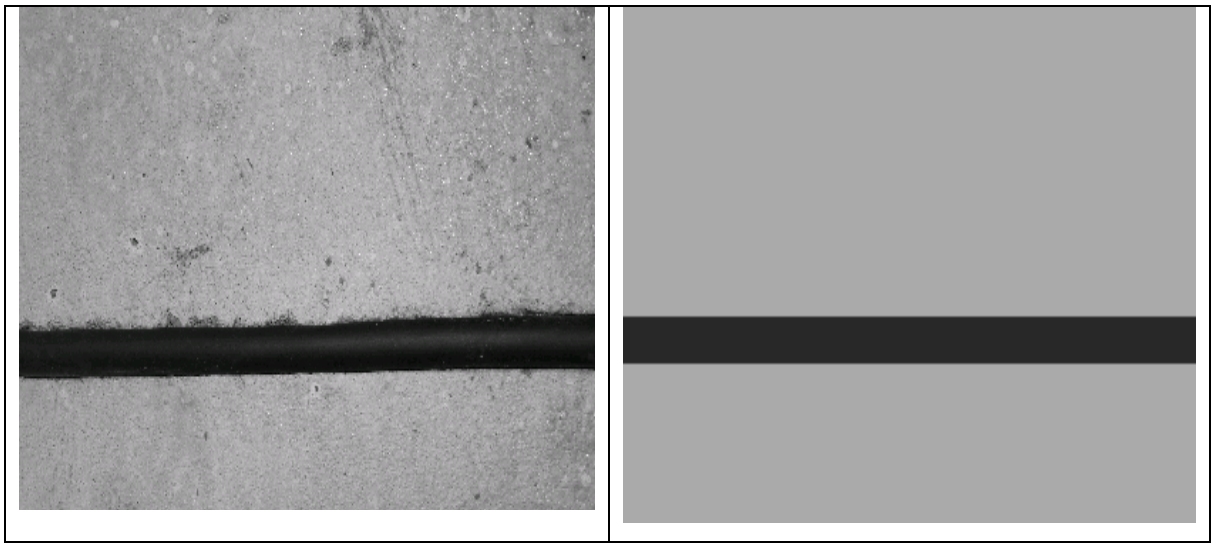

FIGURE 13(a) Digital Image of Concrete Joint

FIGURE 13(b) Modeled Digital Image of the Joint in Figure 13(a)

The comparison of the distribution of intensities across experimental and modeled cracks for selected longitudinal and transverse cracks and a joint are shown in Figures 14 - 16. From the plots in Figures 14 - 16 it can be observed that the intensities inside actual cracks are distributed more randomly compared to those in the surrounding area. The general randomness is due to the non-homogeneity of the concrete mix and one can expect this non-homogeneity to be even more pronounced inside the cracks due to their irregular walls. In contrast, the pixel intensity variation predicted by the reflection model shows an abrupt decrease in pixel intensity up to the crack bottom (Fig. 14(b), 15(b) and 16(b)). This is because one simplifying assumption made in the optical modeling is that both surfaces; inside and outside the crack are individually homogeneous. As a result intensity contrast at the boundaries of cracks and the joint of the modeled images are clearer than those of the corresponding images of actual crack and the joint (Figs. 14(a), 15(a) and 16(a)). Therefore, when the optimum optical parameters (ρ_d , ρ_s and α) for the new model were determined during the calibration, only the minimum pixel intensity

values of the actual cracks were chosen from Figs. 14(a), 15(a) and 16(a) for comparison with the intensities of the modeled images.

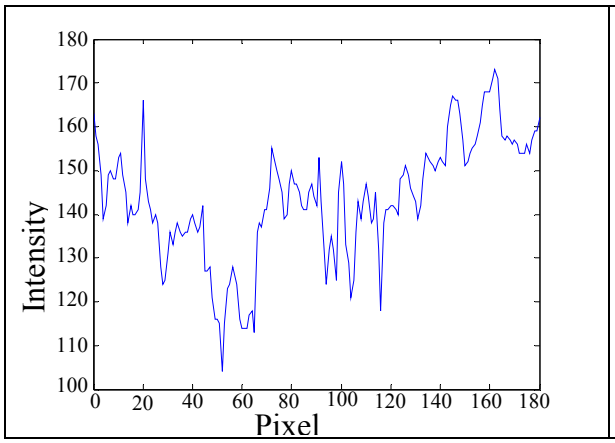

FIGURE 14(a) Intensity Distribution Across Longitudinal Crack a=5.4mm, d=2.5mm

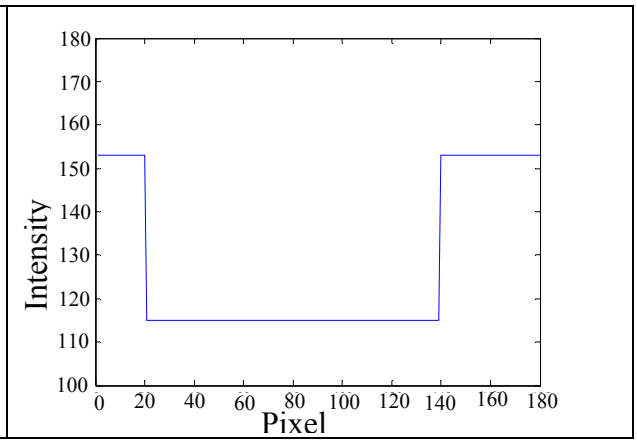

FIGURE 14(b) Intensity Distribution Across Modeled Crack of Figure 11(a)

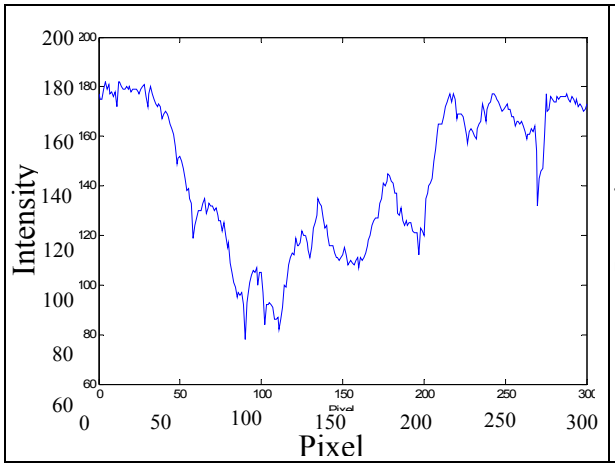

FIGURE 15(a) Intensity Distribution Across Transverse Crack a=9mm, d=7.3mm

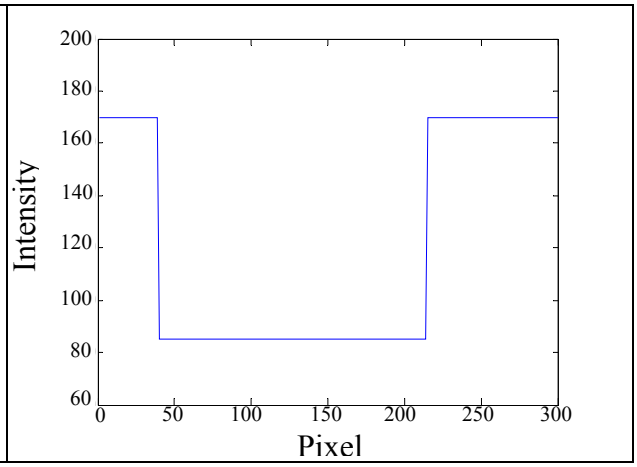

FIGURE 15(b) Intensity Distribution Across Modeled Crack of Figure 15(a)

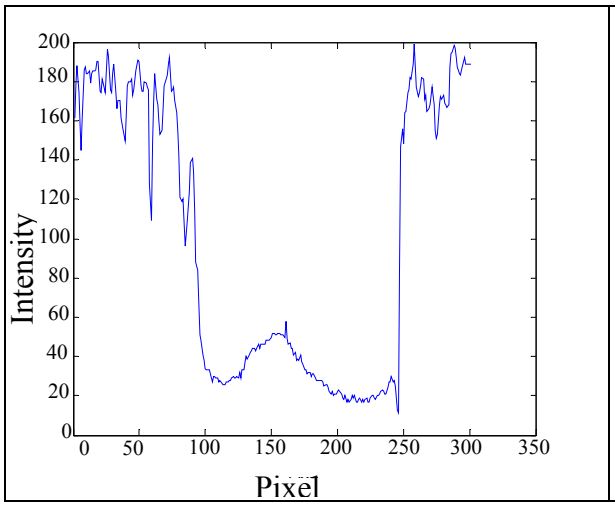

FIGURE 16(a) Intensity Distribution Across Concrete Joint (1 pixel = 0.04 mm)

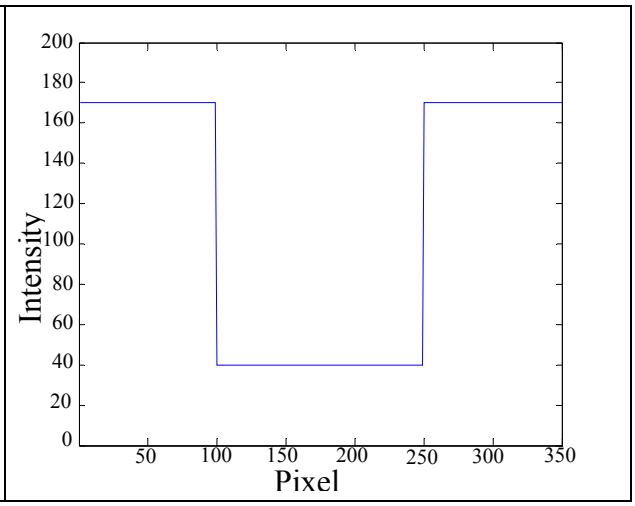

FIGURE 16(b) Intensity Distribution Across Modeled Joint of Figure 16(a) (1 pixel = 0.04 mm)

All in all, Figs. 14-16 show that despite the randomness in the intensity profile in actual cracks and joints due to the inherent non-homogeneity, the intensity profiles in the images of cracks and joints can be simulated reasonably well based on the calibrated reflection model. Similarly, the parameters needed in the new model to predict the intensity variation of joints were also estimated using the intensity distributions across joints. Based on the above described calibration the optimum values of ρ_d, ρ_s and α obtained for the three cases considered are given in Table 3.

TABLE 3 Estimated Parameters for the Model

Type of Feature	Location	Ward's Reflection Parameters		
		ρ_d	ρ_s	α
Longitudinal Crack	Inside	0.8	0.2	0.2
	Outside	0.6	0.4	0.1
Transverse Crack	Inside	0.9	0.1	0.2
	Outside	0.6	0.4	0.1
Joint	Inside	0.9	0.1	0.2
	Outside	0.6	0.4	0.1

As seen in Table 3 it was observed that the model could be calibrated with invariant reflection properties both outside and inside the cracks and joints.

2.5 Verification of the Model

The predictive equations (26 and 27) were verified by plotting the maximum intensity reductions and depths of additional experimental cracks that were not used in the calibration procedure, on the plots generated by Eqns. (26) and (27). For this exercise, based on the definition of $\Delta I)_{max)ult}$ in Eqns. (26) and (27), it would be replaced by the pixel intensity of the uncracked pavement that can be extracted from the images of the experimental cracks. Knowing $\Delta I)_{max)ult}$, for a crack with a known width, the corresponding prediction curve can be generated using Equations 26 and 27. While the curves in Figures 17 and 18 illustrate the respective predictions of Eqns. (26) and (27) for longitudinal and transverse cracks, the discrete points on the same figures show the data obtained from the experimental cracks. It was seen that 80% of the overall predictions yielded errors less than 50% and 52% of the predictions yielded errors lower than 30%. The error was defined as the difference between the actual and predicted depths over the actual depth of cracks. The errors were seen to be more significant for shallow depths possibly indicating that the main source of the errors could have been the estimation of the widths and actual depths of cracks using manual methods.

Furthermore, Figs 19(a) and 19(b) illustrate the correlation between the model predicted crack depths and the measured crack depths. From Figs 19(a) and 19(b) it is seen that there is a satisfactory correlation (high R^2) between the predicted crack depths and the

actual ones with about 0.7 mm of systematic underprediction. However, these results can be improved by modeling the random variations of the image intensity in the uncracked and cracked areas. As seen in Figs. 14(a), 15(a) and 16(a), the random variations in the actual images certainly affect the accurate determination of the maximum intensity contrast in particular and hence the model predicted crack depths. The observed extent of matching between the model predictions and the actual data is encouraging in view of the simplifying assumptions made in the model especially with respect to homogeneity, isotropy, and the regular geometry of cracks.

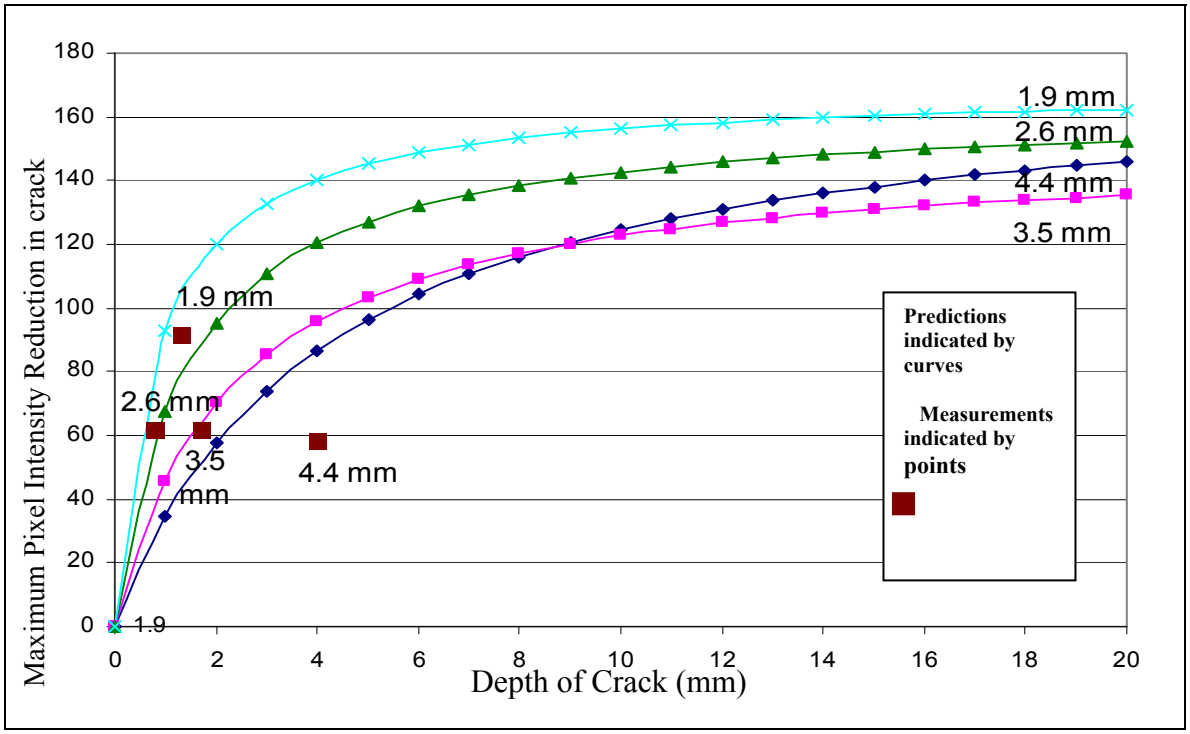

FIGURE 17(a) Predicted and Measured Maximum Intensity Reduction in Experimentally Created Longitudinal Cracks (Widths Lower than 5mm)

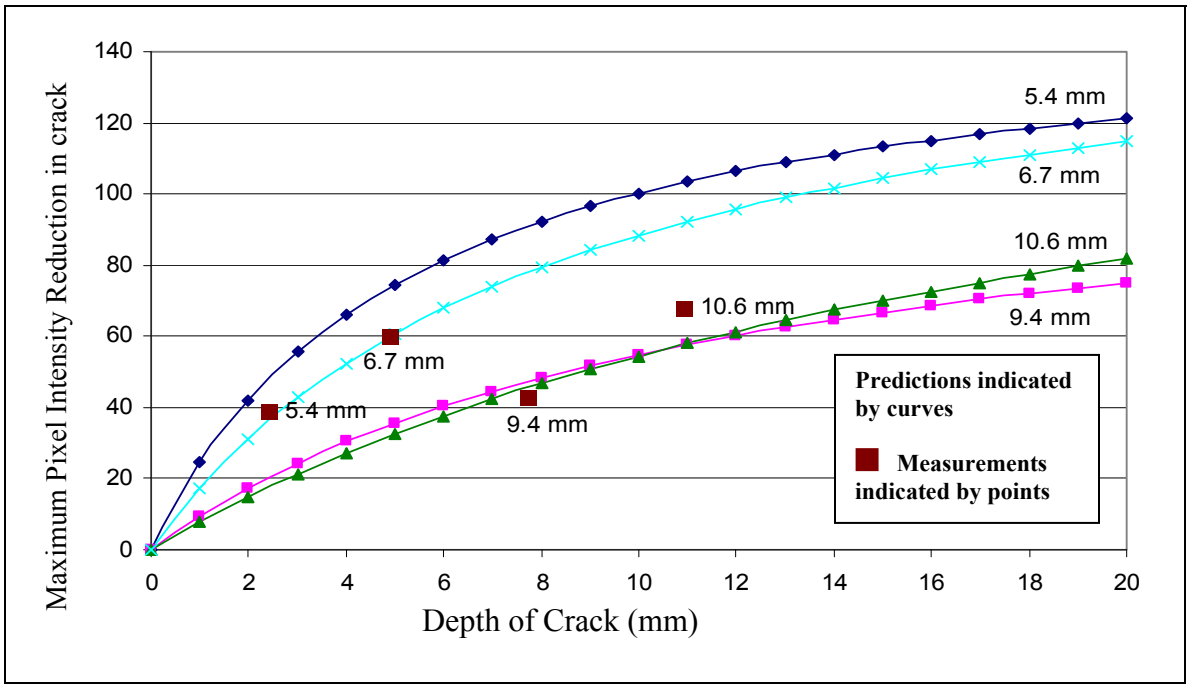

FIGURE 17(b) Predicted and Measured Maximum Intensity Reduction in Experimentally Created Longitudinal Cracks (Widths Larger than 5mm)

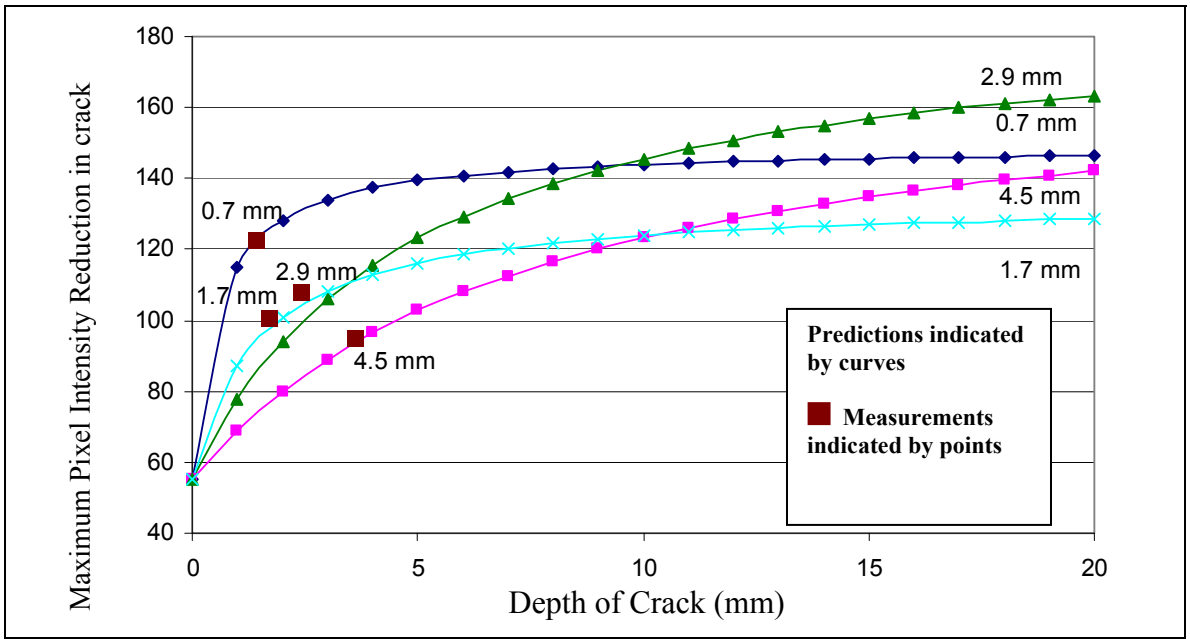

FIGURE 18(a) Predicted and Measured Maximum Intensity Reduction in Experimentally Created Transverse Cracks (Widths Lower than 5mm)

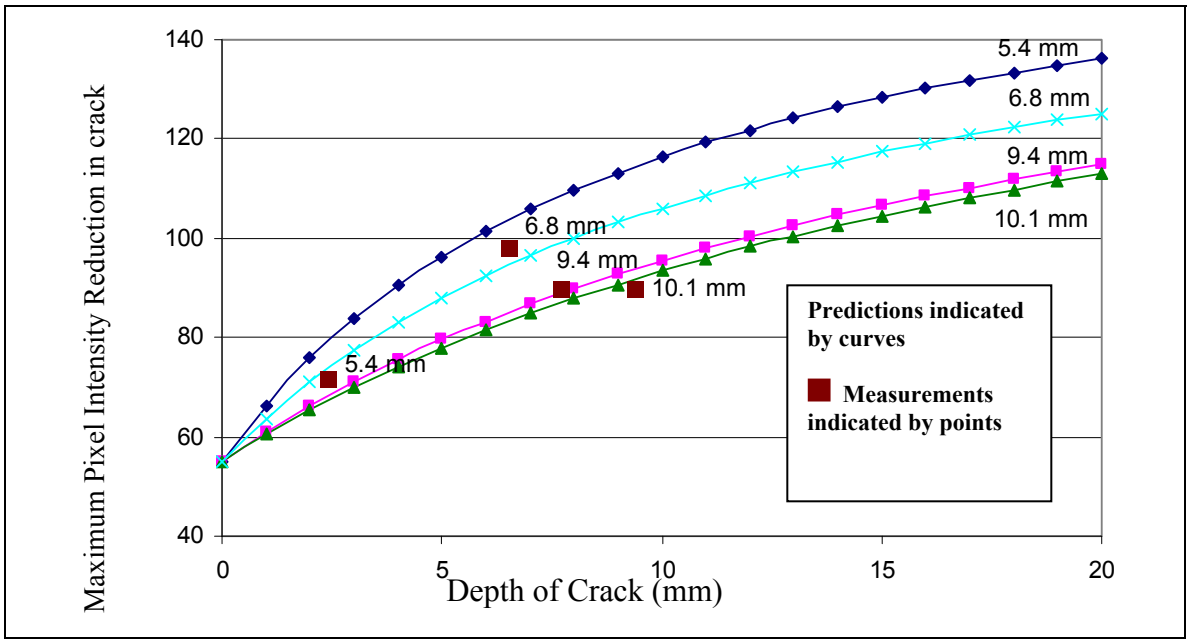

FIGURE 18(b) Predicted and Measured Maximum Intensity Reduction in Experimentally Created Transverse Cracks (Widths Larger than 5mm)

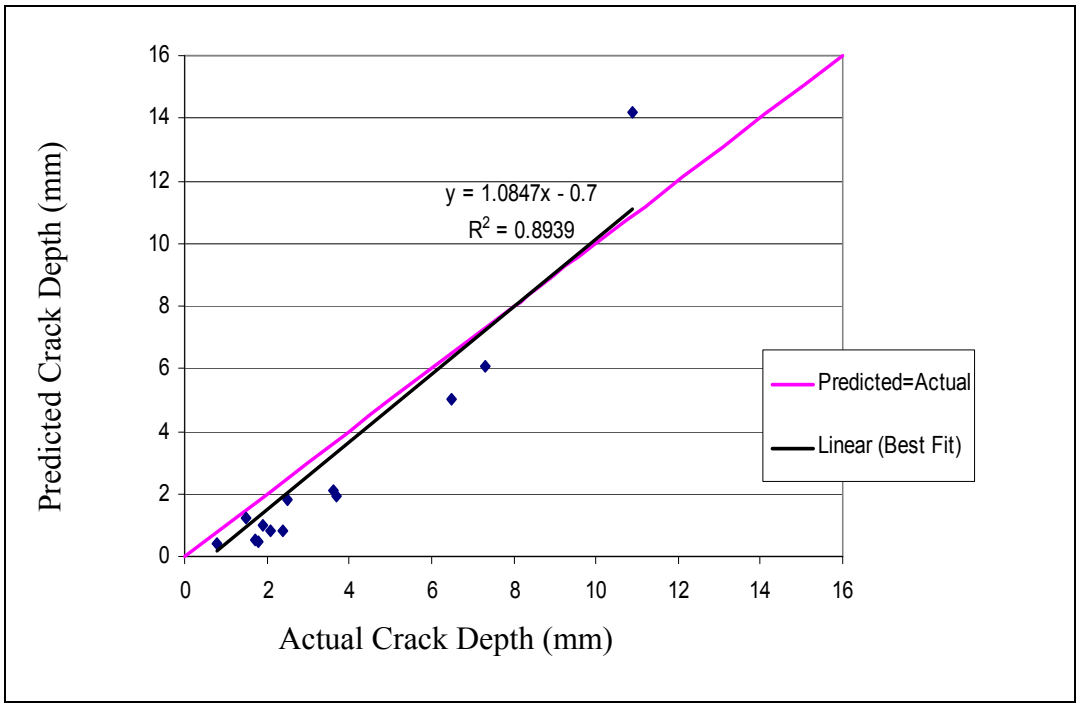

FIGURE 19(a) Variation of Predicted Crack Depths Vs Actual Crack Depths for Longitudinal Cracks

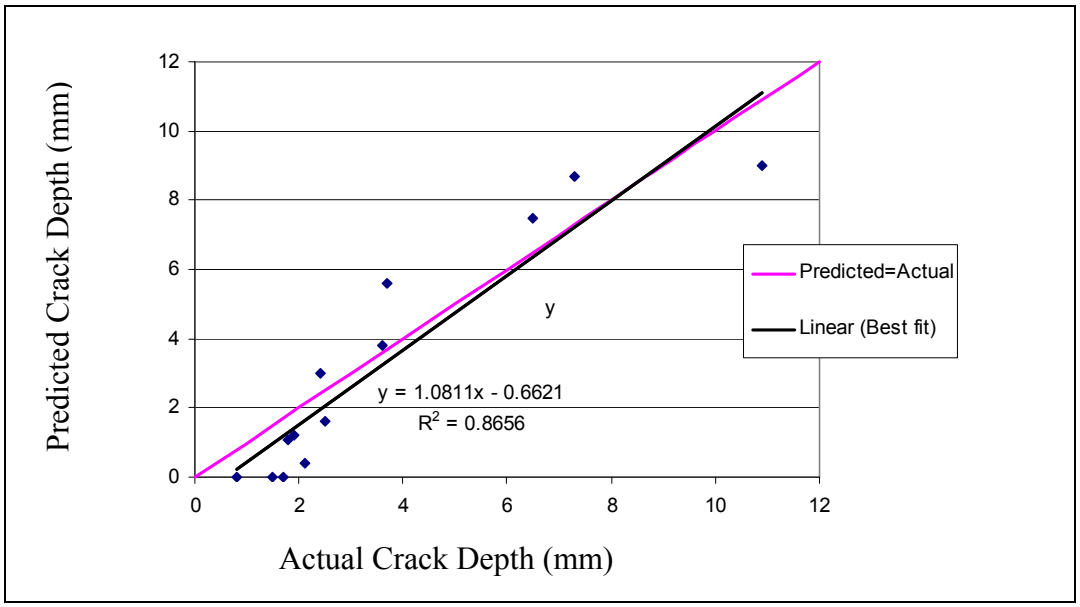

FIGURE 19(b) Variation of Predicted Crack Depths Vs Actual Crack Depths for Transverse Cracks

One realizes that the intensity contrast in the image of a joint is either due to the difference in reflection properties between the filler material and the pavement or the abrupt 90^0 surface slope change that occurs in the case of joints with missing fillers. Hence the images of joints would exhibit a high gradient of pixel intensity variation or rate of change of intensity per pixel. The above fact becomes evident from the comparison of Figs.(14a) and (15a) with (16a). Therefore, cracks can be differentiated from joints based on the gradient of the pixel intensity variation.

2.6 Potential Application in Pavement Rehabilitation

Most sealing and repair strategies of cracked concrete pavements depend on the depths of cracks. Also, in the case of cracked asphalt pavements a knowledge of crack depths is essential to determine milling depths prior to resurfacing. At present, milling depths are determined by the 95^{th} percentile of the crack depth distribution established by three core

samples retrieved from the existing pavement. Currently no non-destructive evaluation method is available to determine even shallow crack depths in an entire pavement network in a speedy manner Hence evaluation of approximate crack depths based on the processing of crack images would be invaluable to pavement maintenance decision making.

Furthermore, when state-of-the-art crack identification software are used to evaluate cracks in *superpave* pavements topped with open graded friction courses, some surface irregularities can be misidentified as small cracks. Even in the case of concrete pavement evaluation, spalling and other surface defects can interfere with crack identification. Therefore, the procedure formulated in this dissertation for identification of shallow crack depths up to 1 cm would be useful in differentiating between cracks and other defects which are generally limited only to the surface.

Based on the results of this preliminary investigation, the following simplified procedure can be recommended for determination of approximate depths of shallow cracks in *concrete* pavements

1. Use currently established procedures to acquire digital images of the pavement section to be evaluated.
2. Using a number of selected "benchmark" cracks in the above section, calibrate the model parameters ρ_d, ρ_s and α as described for different types of cracks (transverse, longitudinal) and joints.

3. Estimate the width (a) of any other crack of which the depth is desired, based on the number of pixels in which an intensity contrast is seen in its image.

4. Knowing the crack width (a) and the pixel intensity of the uncracked area ($\Delta I_{max)ult}$) plot the variation of the maximum theoretical pixel intensity reduction (ΔI_{max}) with the crack depth (d) using Equation (26) (for longitudinal cracks) or Equation (27) (for transverse cracks).

5. Select the depth that produces the maximum pixel intensity difference that closely matches the one obtained from the actual digital image. This is the approximate depth of the considered crack.

It is realized that the field implementation of the new technique is not completely assured at this preliminary phase of research. Also it must be emphasized that the new technique is not meant to replace any of the other image processing techniques that are currently in use, but rather it introduces a novel method of assessing the depths of cracks from images. As in the case of any other crack evaluation procedure, the technique must be improved by accounting for the random variations in pixel intensity, image noise, etc. When the current procedure is refined and programmed efficiently to make it more practical, it would provide an invaluable non-destructive means of evaluating crack depths in pavements and certainly supplement the existing crack evaluation techniques.

CHAPTER 3: OPTICAL TEXTURE BASED TOOLS FOR MONITORING PAVEMENT SURFACE WEAR AND CRACKS WITH TIME USING DIGITAL IMAGES

3.1 Application of Texture Analysis in Pavement Evaluation

For periodic project-level pavement crack growth or wear evaluations, the relevant pavement sections must be imaged at regular time intervals, often under different illuminations, and subsequently the features of interest in one image have to be matched and compared to the corresponding features of previous images of the same locations. Although the approximate locations of a multiple sequence of images can be corresponded using the GPS and DMI (Distance Measuring Instrument) equipped in modern imaging vehicles, the above tracking methods cannot be used to detect the exact location of the pavement to match the level of resolution of the imaging camera. Furthermore, currently available automated crack evaluation techniques are not designed to monitor the rate of crack growth or wearing of the pavement in specific locations of interest.

The techniques presented in this dissertation are recommended only for project-level studies where selected areas of pavement sections have to be monitored for cracks or wearing. From the images of the relevant pavement sections that are obtained during the initial survey time, specific locations have to be earmarked where changes are required to be continuously monitored with time. When images captured at the same locations at different times are first identified using the GPS and DMI the images corresponding to

the earmarked areas can be selected approximately. It is in the more precise or refined matching of the earmarked pavement details that the tools described in this dissertation can be quite useful.

3.1.1 Imaging Vehicle

Most of the images used in this study were obtained by the Multi Purpose Survey Vehicle (MPSV) of the Florida Department of Transportation (FDOT) (Figure 20(a)). MPSV uses a Basler 103 linescan camera (1 in Figure 20(a)) and an artificial lighting system (2 in Figure 20(a)) consisting of ten 150 kW lamps. Two parameters that affect the illumination of pavement images are natural and artificial lighting. When state-of-the-art laser lighting techniques are adopted for image acquisition such as that reported in Wang (2007), the issue of shadows could be minimized. Another parameter that causes variability of the images is the orientation of the pavement camera at the time of image capture. Although the pavement camera is rigidly fixed to the MPSV and oriented vertically downward (Figure 20(a)), the orientation of the features of interest in the image could change due to the random wandering of the survey vehicle during repeated runs. Sample asphalt and concrete pavement images collected by this vehicle are shown in Figures 20(b) and 20(c) respectively.

FIGURE 20(a) FDOT Multi Purpose Survey Vehicle (MPSV) Used for Pavement Imaging

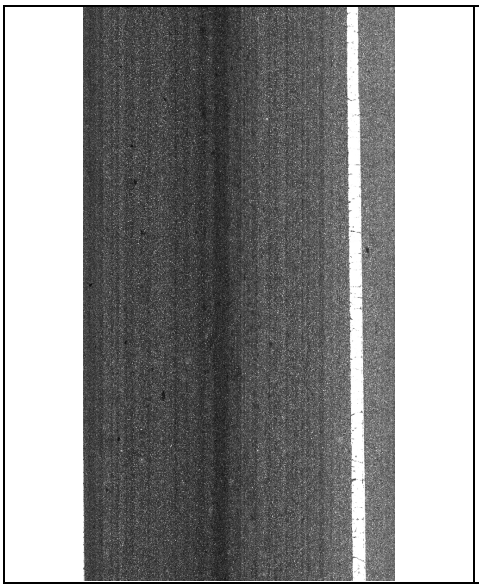

FIGURE 20(b) Sample Asphalt Image Collected by MPSV

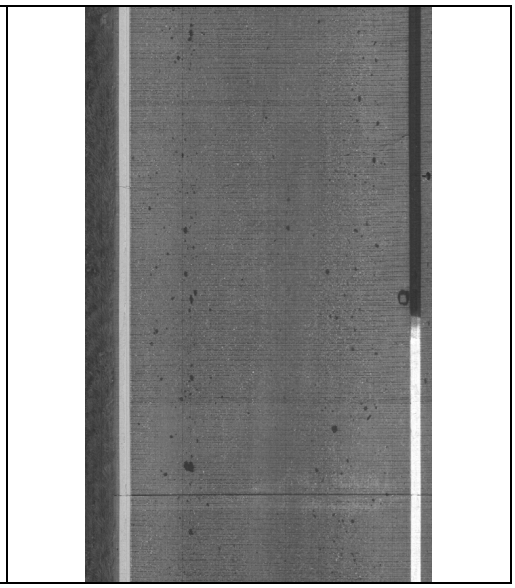

FIGURE 20(c) Sample Concrete Image Collected by MPSV

3.2 Texture Characterization of Digital Pavement Images

A number of image (optical) texture characterization techniques that have applications in pavement image processing will be discussed in this section with their actual applications illustrated in two later sections.

3.2.1 Scaled Scattering Index (SSI) and its Usefulness

The size of a typical texture-wise *homogenous section* or the size of the texture primitives in an image depends on the features of the image and the intensity distribution within the images. The Scaled Scattering Indicator (SSI) (Germain et al., 2000) which quantifies textural properties based on the local differences of a given attribute can be used to determine the approximate homogeneous section size. It is also a useful tool for classification of the extent of randomness of the texture in an image.

The differences in the constituents of asphalt concrete (AC) and Portland cement concrete (PCC) result in distinct pavement surface textures and even within each type the random distribution of material constituents changes the surface texture from one location to another. Consequently, the *optical* texture of pavement images would inherit the same randomness due to the differences in the Bidirectional Reflectance Distribution (BRD) of the pavement *surface* texture.

Depending on the observation scale, the local average intensity differences and local texture orientation respectively represent the homogeneity and anisotropy of the texture of an image. The mean intensity inside a *n x n* observation pixel window centered around the point *(x,y)* is defined as $\alpha_n(x,y)$, which is evaluated as,

$$\alpha_n(x,y) = \frac{1}{n^2} \int_{y-n/2}^{y+n/2} \int_{x-n/2}^{x+n/2} p(u,v)dudv \tag{28}$$

where *u* and *v* are respectively the horizontal and vertical pixel positions inside the window, and $p(u,v)$ is the intensity at the pixel *(u,v)*. For longitudinal (vertical) neighboring windows SSI^2 is calculated by Equation (29).

$$SSI^2(n) = E\left[(\alpha_n(x_0, y_0) - \alpha_n(x_0, y_0 + n))^2\right] \quad (29)$$

where *E* denotes the expected value. Similarly, $SSI^2(n)$ can be computed for transverse (horizontal) neighboring windows as well. The homogeneous texture size can be obtained by the *n* value that corresponds to the Maximum value of SSI^2 *i*n a plot of SSI^2 Vs *n*. Figures 21(a) and 21(b) show the variation of SSI^2 in the longitudinal and transverse directions respectively for asphalt images captured within a narrow band of illumination measured in klux. Curves denoted by FO, FL, 56th and 46th represent images from Fowler Avenue (FO) at 50.2 klux, Fletcher Avenue (FL) at 55.9 klux, 56th Street at 52.5 klux and 46th Street at 54.5 klux respectively in Tampa, FL. It can be seen from Figures 21(a) and 21(b) that for all the cases, the highest SSI^2 was observed at an observation scale of *only 4x4 pixels* indicating a mostly random and heterogeneous optical texture.

Figure 21(c) illustrates the SSI^2 distribution for a concrete pavement on US41 in Port Charlotte, FL. It can be observed from Figure 21(c) that as in the case of asphalt pavements (Figures 21(a) and 21(b)), the major SSI^2 peaks in both transverse and longitudinal directions at an observation scale of 4x4 pixels, which corresponds to the natural texture of the concrete pavement. However, in addition the SSI^2 profile for the concrete pavement in Figure 21(c) also shows a secondary peak at an observation scale of 13x13 pixels. This reflects the artificial line texture (tined finish) apparent in Figure 21(c) which in fact was manually observed to have a period of about 10-15 pixels.

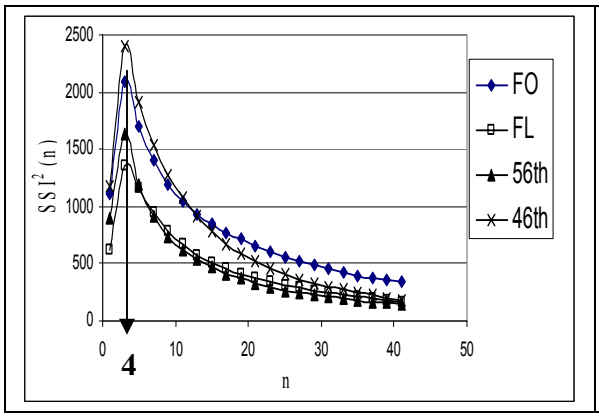

FIGURE 21(a) Variation of SSI^2 in the Longitudinal Direction Vs Observation Scale for Images of Four Types of Asphalt Pavements at Constant Illumination

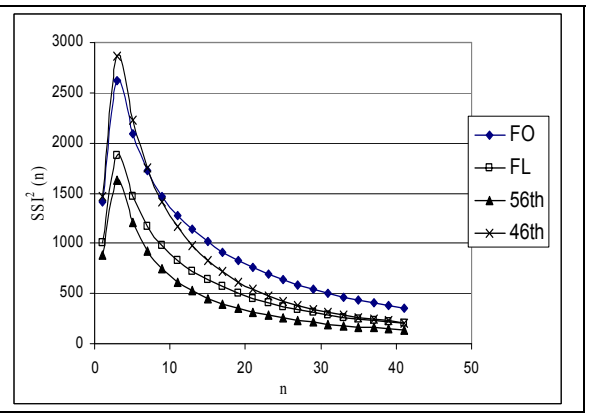

FIGURE 21(b) Variation of SSI^2 in the Transverse Direction Vs Observation Scale for Images of Four Types of Asphalt Pavements at Constant Illumination

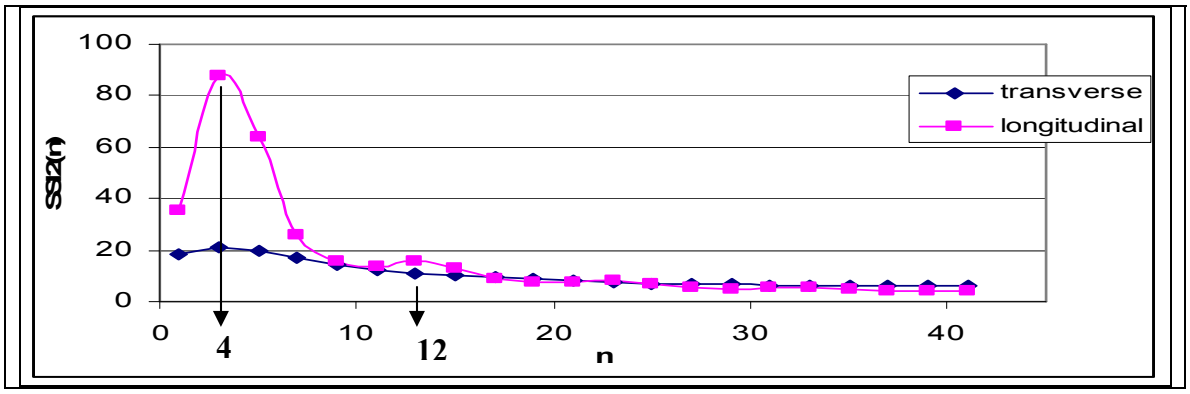

FIGURE 21(c) Variation of SSI^2 Vs Observation Scale for a Concrete Pavement Image on US 41

Different mixtures used for pavement construction produce different SSI values in their images depending on the varying proportions of constituent materials. Hence their texture primitive sizes represented by *SSI* can be used to characterize different pavement mixtures. Furthermore, the concept of *SSI* can also be used as a measure of quality assurance by comparing the *SSI* Vs *n* plot among images of various sections of a newly constructed pavement. Moreover, the *SSI* Vs *n* plot derived from the images captured at

various stages of the life of any pavement can be used to monitor the rate of degradation of that pavement since the degradation caused by the impact of traffic and environmental conditions changes the pavement texture resulting in definitive changes in the *SSI* Vs *n* behavior.

3.2.2 The Concept of Texture Distance

Another image texture based tool that can be used for determining the degree of similarity of optical texture in digital images is the texture distance evaluated between corresponding segments of two or more images. When two image segments are to be matched, the image segment that is used to match is termed the *query image* (Q) and the images that are matched with the query image are called the *compared images* (C). Out of the several images of the same size that are compared with the query image, generally only one exactly matches with the query image, and the latter image is termed the corresponding image. The pixel intensities in the query and the compared images are represented as texture description vectors *T(Q)* and *T(C)* respectively. *T(C)* and *T(Q)* respectively store the 2D pixel intensities of the compared and query images in a 1D array only after an appropriate processor is applied to highlight the desired texture. Then the texture distances between the query image and each compared image are computed for all the regions in the compared image. Finally, the region in the compared image corresponding to the lowest texture distance is selected as the region that matches the query image. Thus the matching region is given by,

$$d_{match}(C_i, Q) = \min \left\| T(C_i) - T(Q) \right\|^2 \tag{30}$$

where *i* (*1,n*) defines a particular region of matching and *n* is the total number of regions in the database image. Unless the query image and the compared *corresponding* image have very specific textures, this method becomes a crude method of determining texture similarity.

The second method of evaluating texture distance is to divide the section of interest in the query image into separate homogeneous grids. Then the texture vectors $(T_g(Q))$ are evaluated separately for each grid. Each compared image is similarly discretized using the same grid size. The texture distance between the corresponding grid cells of the compared and query image is evaluated and their summation is computed as the total texture distance between the query and the compared image sections (Eqn 31).

$$d_{gridded\_texture}(C_i, Q) = \sum_g \hat{d}_{texture}(T_g(C_i), T_g(Q)) \tag{31}$$

where, $\hat{d}_{texture}(T_g(C), T_g(Q))$ is the texture distance between the query image and the compared image *i*, for the grid *g*. Finally, the particular section in the compared image corresponding to the minimum texture distance is selected as the section that matches the query image section. Obviously, a more effective comparison can be made between the textures of two images if the texture distance is computed after highlighting the desired texture feature (edge, spot etc.) using an appropriate texture mask. Hence highlighting of desired pavement texture using specific texture masks will be discussed in the ensuing section.

Although the concept of *minimum texture distance* can be used to find the exact correspondence using two images of the same location collected at different times, if major changes due to distresses or wear have occurred in the selected pavement segments, this concept cannot be used for correspondence. On the other hand the *maximum texture distance* can be used to find the locations where maximum texture changes have occurred. For example, when the texture distance between different segments along the crack are compared with the corresponding segments of the crack collected at a different time, the texture distance for each segment could be different depending on the elongation and widening of that crack. In such cases, the maximum texture distance would represent the section where the maximum changes in texture has occurred due to either elongation or widening of the crack.

3.2.3 Use of Texture Masks

Well defined local masks can be employed to detect areas of digital images that have specific optical texture patterns. Therefore, masking would be a reliable tool for, first highlighting and then identifying features of interest such as edges, spots, ripples etc. in pavement images. Nine standard 5x5 convolution masks have been developed by Laws (Shapiro and Stockman, 2001) using the 5x1 vectors defined in Eqn. (32). They are:

L5 (Level texture) = [1 4 6 4 1] (32a)

E5 (Edge texture) = [-1 -2 0 2 1] (32b)

S5 (Spot texture) = [-1 0 2 0 -1] (32c)

R5 (Ripple texture) = [1 -4 6 -4 1] (32d)

The vectors L5, E5, S5 and R5 yield center-weighted local average, edges, spots and ripples respectively. Then nine different masks can be formed by computing the outer products of each pair of the above vectors. They are designated as L5E5, L5R5, E5S5, S5S5, R5R5, L5S5, E5E5, E5R5 and S5R5. As an example L5E5 is obtained by the product of Eqns. (32a) and (32b):

$$L5E5 = \begin{bmatrix} -1 & -2 & 0 & 2 & 1 \\ -4 & -8 & 0 & 8 & 4 \\ -6 & -12 & 0 & 12 & 6 \\ -4 & -8 & 0 & 8 & 4 \\ -1 & -2 & 0 & 2 & 1 \end{bmatrix} \tag{33}$$

When operating any one of the above masks on an image, the mask is first applied as an intensity multiplier in the neighborhood of every pixel *(i,j)* of the image and then its pixel intensity $P_{i,j}$ is replaced by the resultant intensity $P'_{i,j}$. The masking operation is defined by the following convolution equation.

$$P'_{i,j} = \sum_{l=-2}^{2} \sum_{k=-2}^{2} P_{i+k,j+l} . M_{3+k,3+l} \tag{34}$$

where, *M(k,l)* [k={-2,2}, l= {-2,2}] are the elements of the mask *M*. Then energy maps indicating the prevalence of the specific textures in the original image can be developed by using the updated intensity values obtained on the application of the relevant masks. If desired, the given image can even be clustered into regions of uniform texture using these texture energy maps. However, clustering is generally inapplicable for surfaces with widely varying texture such as pavements.

3.2.4 Method of Homogeneous Coordinates

The texture similarity method operates based on the logic that the minimum texture distance between the query image and the compared *corresponding* image corresponds to areas of similar texture in the two images. For this technique to produce accurate texture matching, both images must have the same orientation and the scale, since matching is performed based on areas demarcated by horizontal (longitudinal) and vertical (transverse) boundaries encompassing a fixed number of pixels. However, during typical project-level pavement evaluation exercises leading to repeated imaging of the same pavement location, the orientation and the scale of the images could change due to the wander of the survey vehicle and the possible changes in camera setting respectively. In addition the minimum texture criterion would not be applicable for cases where the level of distress changes in the corresponding areas. The above limitations can be overcome by replacing the texture similarity technique by the method of *homogeneous coordinates* in matching the correspondences among images collected at different times and illuminations. This method, based on geometrical correspondence only, precludes the need for orientation and scale adjustment in the images. It would also address the inability of the texture similarity correspondence to detect corresponding points on a distressed location that grows in extent or severity or both.

In the method of homogeneous coordinates (Trucco and Verri, 1998), for any point $(x_{1,} y_1)$ of the query image, Equation (35) is used to obtain the corresponding points $(x_{2,} y_2)$ in the compared image.

$$\begin{bmatrix} x_2 \\ y_2 \\ 1 \end{bmatrix} = \begin{bmatrix} r_{11} & r_{12} & r_{13} \\ r_{21} & r_{22} & r_{23} \\ r_{31} & r_{32} & r_{33} \end{bmatrix} \begin{bmatrix} x_1 \\ y_1 \\ 1 \end{bmatrix} \tag{35}$$

The nine unknown components r_{ij} (for *i,j =1,3*) of the rotation matrix (***R***) between the two images can be determined by substituting the coordinates of three known correspondence points (*i=1-3*) in the query image $(x_{1i,} y_{1i})$ and the compared image $(x_{2i,} y_{2i})$, in Equation (35). Then Equation (35) can be used to determine the correspondences $(x_{2,} y_2)$ (in the compared image) for any other specified coordinates $(x_{1,} y_1)$ of the query image. Hence this method provides accurate correspondences of points between two images irrespective of the differences in scales and orientations since the scale and orientation are automatically incorporated in the matrix ***R***. In this dissertation, the method of homogeneous coordinates will be illustrated by its application in locating the correspondences on active cracks in asphalt images.

If a relative rotation exists between the features in the two images, the angle of rotation (θ) between the two images can also be determined by using the components of the matrix ***R*** given in Equation (35) as:

$$\theta = \frac{r_{21}}{r_{11}} \tag{36}$$

3.3 Applications in Pavement Image Correspondence

Tools of texture correspondence of images can be useful in monitoring the changes in pavement characteristics in a variety of applications in pavement evaluation. Although

images captured at different times could have widely varying *total* intensity distributions (histograms), the *relative texture* of a given location in an image with respect to other locations would only change due to the propagation of distresses at that location or wearing of the surface. Therefore tools that predict texture similarities or differences can be used, devoid of the illumination effects, to monitor distress propagation and wearing of pavements using their images captured at different times. Different pavement materials respond to growth of cracks or traffic or environment induced wear at different rates and as part of projects it is necessary to compare the rates of degradation in materials. The rates of crack growth or wear in different pavement surface types can be monitored using correspondence of images. This can be achieved by corresponding images close to the area of interest using texture similarity measures or homogeneous coordinates and then determining the rate of degradation with time. Thus, two ideal applications of these tools would be in the regular monitoring of (1) hairline crack *growth* and (2) wearing of the pavement within a closely monitored section, using a sequence of images collected at different times.

3.3.1 Eliminating the Effect of Illumination and Moisture

If texture matching is to be performed to detect a certain feature (ex. edge texture for detection of cracks), the matching exercise can be made more effective by operating the relevant mask on the image. However, prior to using Laws' texture masks for the texture matching, the effects of illumination must be removed from the query image and the compared image. This is typically achieved by selecting a window size of more or less homogeneous intensity and subtracting the mean of the intensities of this window from

the intensity of its center pixel. Laws' texture method recommends a 15 x 15 pixel window to be considered for this purpose assuming the prominent features of the image to be larger than a 15 x 15 pixel set. However, the basic size of the texture primitives in typical pavements could be smaller than a 15 x 15 window under normal imaging resolutions. Hence an approximately homogeneous section size must be selected for a given pavement surface texture so that the effect of illumination can be removed without altering the features. The SSI concept that was introduced in Section 2.1 becomes useful in the selection of the homogeneous size for a particular image texture. It was shown that the homogenous sections for both asphalt and concrete were 4x4. Since it is practically inconvenient to use 4x4 pixels as the homogeneous section, for all pavement images a 15x15 window suggested in the literature (Shapiro and Stockman, 2001) was used for eliminating the effects of illumination.

Moisture changes the appearance of pavements in terms of color, reflection and transparency characteristics. If the effect of moisture on pavements is more or less uniform in all areas of the studied pavement section in terms of the image intensity variation, then the correction for moisture effects would be similar to the removal of the effect of illumination. However, if moisture is retained only inside cracks or troughs of the pavement, then the intensity variation due to this must be considered. This can be addressed by modeling and observing the intensity variation of images at different moisture contents and removing the effect of moisture prior to processing. However, this cumbersome problem can be avoided if images are obtained after a dry period that allows water to be completely removed from the surface.

3.3.2 Correspondences of Concrete Images

Figure 22(a) shows one segment of a sample concrete image collected on US41 in Port Charlotte, FL using the FDOT MPSV, while Figure 22(b) shows the matched area of the corresponding image collected at the same location during a different run on the same day. The selected window of the first image contains a crack (considered as an "edge") and hence the L5E5 mask was used to determine its corresponding position in the second image (Figure 22(b)). Although the pixel intensities are different in the two instances primarily due to the differences in illumination, this method enables one to detect the exact corresponding location in the second image. Figure 23(a) is a gray scale (intensity of 0-255) plot of the texture distance (Equation 4) between the image in Figures 22(a) and image segments of the same size at different locations of Figures 22(b), with the intensity of a given area in Figure 23(a) setup to be proportional to the texture distance between that area and the query image section. The dark spot (lowest intensity) at the center of Figure 23(a) indicates the area with the minimum distance between the two images, which in fact was verified manually to be the exact matching position.

Figure 24 shows similar results for the same concrete pavement at a different location where the exact identification could be made even in the absence of major identification features such as cracks and isolated defects. It is also evident that the matching can be achieved even with the marked difference in illumination between the images in the two runs. Similar to Figure 23(a), the dark spot at the center of Figure 23(b) shows the area with the minimum texture distance between the two images (Figures 24(a) and 24(b)), which corresponds to the exact matching position.

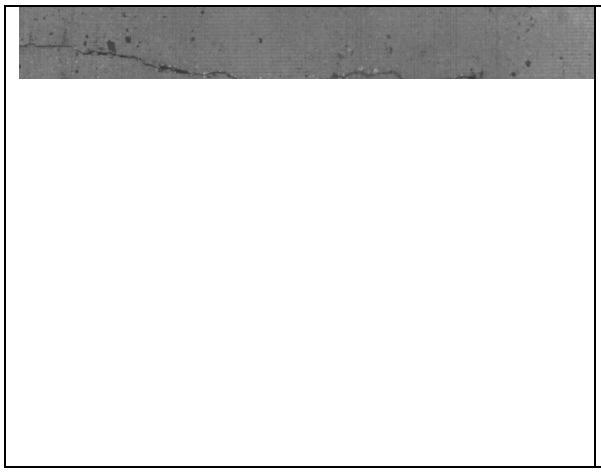

FIGURE 22(a) Query Image of a Cracked Concrete Pavement

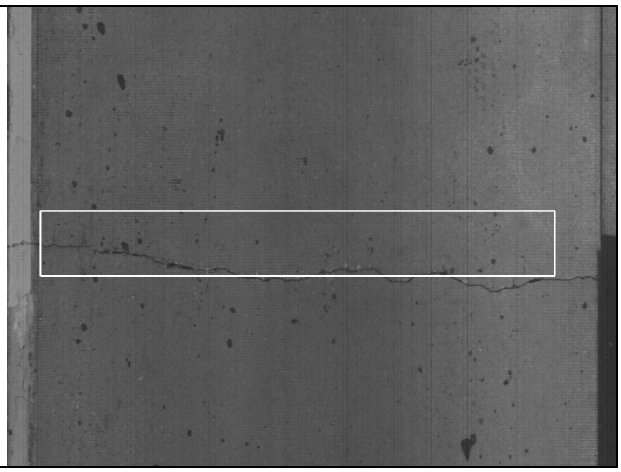

FIGURE 22(b) Compared Image of Figure 22(a) after Matching

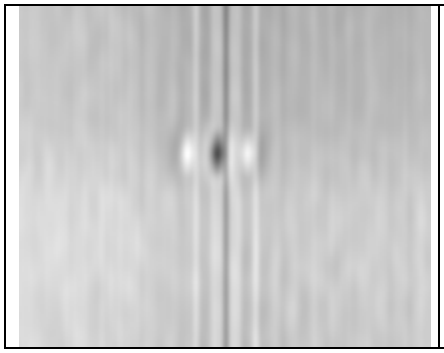

FIGURE 23(a) Display of Distance Measurement for Figure 22

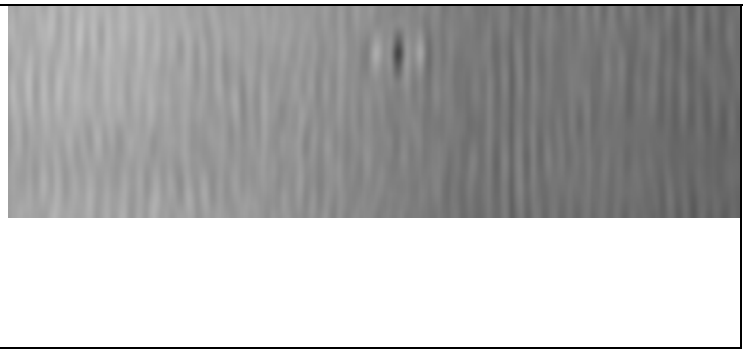

FIGURE 23(b) Display of Distance Measurement for Figure 24

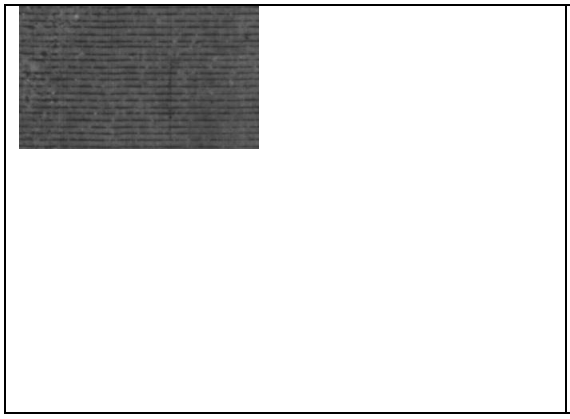

FIGURE 24(a) Query Image of an Uncracked Concrete Pavement

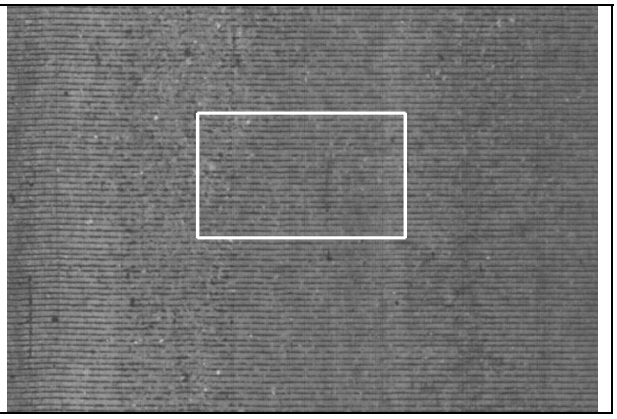

FIGURE 24(b) Compared Image of Figure 24(a) after Matching

3.3.3 Detection of Pavement Wear through Correspondences of Asphalt Images

It is well established that the skid resistance of a pavement depends on the microtexture of the aggregate as well as the macrotexture depth (mean profile depth (MPD)) and wavelength. MPD and wavelength are governed by the size and spacing of the aggregates respectively. Lower MPDs, higher wavelengths and smooth textured aggregates decrease the skid resistance of pavements. Thus pavement wear lowers both microtexture and macrotexture and reduces the skid r esistance of pavements. It was theoretically proved and experimentally verified (Amarasiri et al., 2009) that the pavement surface degradation due to changes in macrotexture and microtexture results in quantifiable changes in the intensity of the corresponding images. It was also found by Amarasiri et al. (2009) that the brightness of an image increases with pavement wear. In a similar study by Khoudeir and Brochard (2004), pavement wear has been attributed to changes in the gray level distribution, absolute value of the gradient, the autocorrelation function, and the distribution of the curvature map of corresponding digital images. Amarasiri et al. (2009) also showed that once an equipment specific correlation is developed between the intensities of images captured at one stage of wearing and the skid friction measurement corresponding to that stage, the intensities of images can alone be used to predict the friction measurements at future stages. The above research findings can be used to determine the degree of wear of pavements at different stages of their life using the intensities of corresponding images. The matching technique developed in the current research would be ideal during such efforts for identifying the location to be monitored for wear at every stage.

However, to compare the image intensity distribution at different times, the exact pavement section has to be corresponded at each time. This can be achieved by using the minimum texture distance criterion to find the corresponding points. Generally changes in texture due to wear are limited to the wheel paths. Hence the minimum texture distance can be an appropriate method to correspond the exact locations of the relatively unaffected neighboring non-wheel path areas of images collected at different times. Then the significant texture changes that occur on the wheel path locations that are visible in the images can be estimated to evaluate the degree of wear.

Figures 25(a) and 25(b) are two images collected from a section of the asphalt pavement in Fowler Avenue, Tampa, Florida on 8th July 2007 and 20th January 2008 respectively. These will be used to illustrate similarity matching and detection of pavement wear. Even after the illumination effects were removed from the two images, locations close to one wheel path of the compared image (around point **B**) showed significant texture changes compared to the point **A** outside the wheel path. Since no significant distress was seen at **B**, it was determined that the relatively high change of the texture would be due to pavement wear. However, in order to evaluate the texture change at **B** accurately, one must locate the point **B** in *both* images.

This is made possible by first corresponding a point outside the wheel path, such as **A** with minimal texture changes, in the two images. When the minimum texture distance criterion was applied to the two images in Figs. 6(a) and 6(b), point **A** is matched exactly as seen in the dark spot in Fig. 6(d). Then, based on the relative positions of **A** and **B,** one

can locate the point **B** in Figs. 6(b) and 6(c). Furthermore, Fig. 6(d) depicts the relative texture distance between the two image segments with the point **A** with no texture change corresponding to the minimum distance. Finally, the texture distance corresponding to the point **B** and hence the degree of wear at **B** can be estimated based on Fig. 6(d). It can be concluded that while the procedure for detection of texture similarity is applicable to locations where no significant changes in texture have taken place between imaging times, it can also be extended to evaluate the wear at neighboring locations.

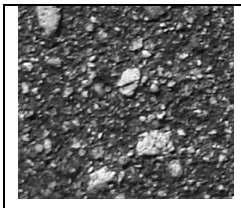

FIGURE 25(a) Query Image of an Asphalt Pavement

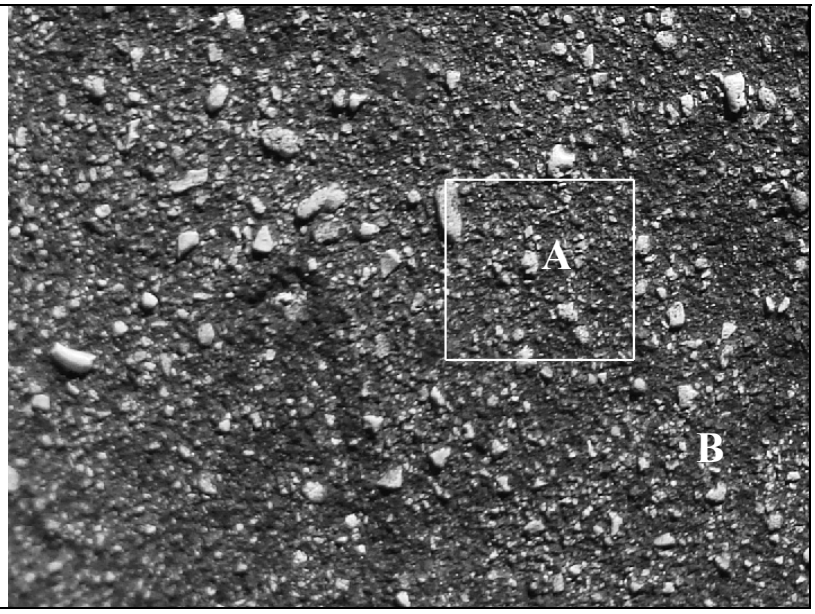

FIGURE 25(b) Compared Image of Figure 25(a) after Matching

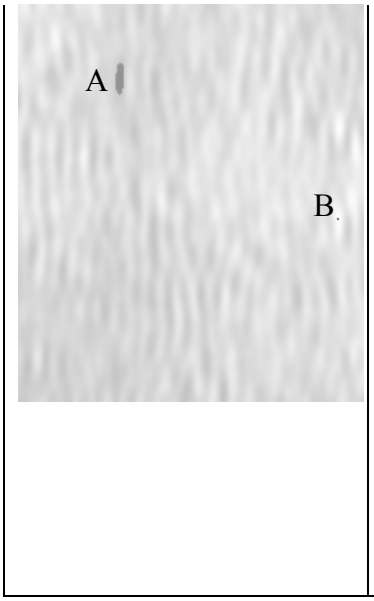

FIGURE 25(c) Display of Distance Measurement for Figure 25(a)

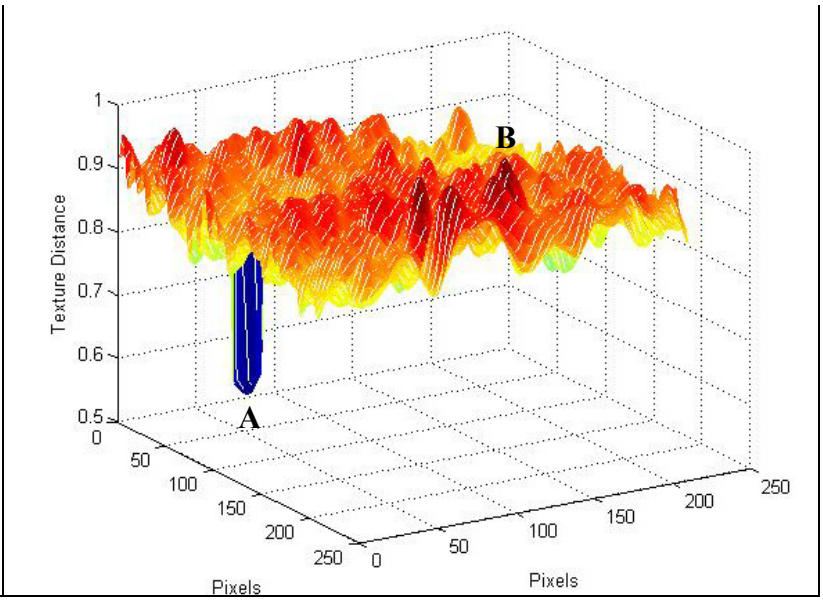

FIGURE 25(d) 3D Display of Distance Measurement for Figure 25(b)

3.4 Application to the Monitoring of Crack Growth

The durability of a pavement depends on the rate of crack propagation. The higher the rate of crack propagation, the faster the rate of pavement deterioration. Hence monitoring of individual cracks at the project level could furnish valuable information on the performance of a given pavement mix or a specific maintenance or rehabilitation technique. These objectives can be achieved by monitoring a few selected representative cracks on the given pavement section.

To formulate a new methodology for monitoring of the growth of selected cracks using the tools described in this dissertation, images of five asphalt pavement locations with different traffic levels (low-high) were selected. At each location, low, medium and high severity cracks were earmarked for growth monitoring. For locations where texture

changes between images were minimal, the minimum texture distance was used for correspondence, while for locations with significant changes in texture, homogeneous coordinates were used. On the other hand, the maximum texture distance was used to find the locations of a crack where maximum texture changes have occurred.

3.4.1 Use of Canny Edge Detector for Crack Tip Identification

In automated pavement evaluation systems, edge detection has been considered as the conventional method for identifying and classifying pavement cracks. Of the common Edge Detectors that are currently used in digital image processing, the Canny Edge Detector (Canny, 1986) is one of the most effective ones used to detect the intensity contrasts (edges). Wang et al. (2007) used a wavelet based technique to detect edge information from pavement surface images. In this work, it was first attempted to use the Canny Edge Detector built in MATLAB to detect the intensity contrasts at the cracks. The parameters to be assigned for the Canny Edge Detector are the contrast threshold intensity for the edges and its standard deviation. Then the edges of images that are above the threshold are detected automatically. Trial threshold values and variances were used to select the optimum identification conditions. In the case of asphalt texture, since the aggregate particle/asphalt binder interface had a higher contrast than the edges of cracks, the edges of the particles were highlighted over the edges of cracks. Figure 26 shows the results of edge detection with a threshold of 0.25 and a variance of 0.1. This analysis demonstrates that the Canny Edge Detector is inadequate for detection of an asphalt pavement crack tip.

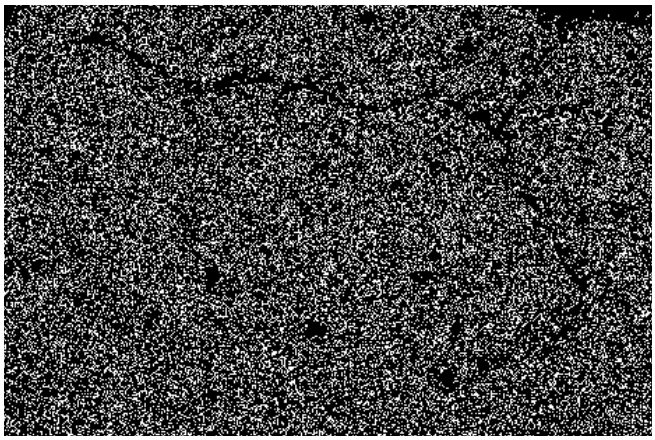

FIGURE 26 Resulting Image of FOM1 after Application of Canny Edge Detector

3.4.2 Application of Homogeneous Coordinates to Study the Pavement Crack Growth

To monitor the growth of a crack two criteria must be available; (1) any common (matching) location on the crack appearing in the initial and the updated images (2) identification of the crack tip location in the two images. Although homogeneous coordinates technique is adequate to determine matching locations on active cracks, in order to locate the crack tip accurately, one also needs an edge detection technique.

3.4.3 Application of Maximum Texture Distance to Study the Pavement Crack Growth

Correspondences between images of cracks which do not change in width can be determined using the minimum texture distance criterion. However, extending crack tips and widening crack locations cannot be matched because of the significant texture changes at the crack tip and widening locations. On the other hand, the combination of the homogeneous coordinates and the maximum texture distance concept satisfy the respective criteria mentioned above for monitoring the growth of an active crack. Thus the above techniques was used to detect the locations of crack tips and widening

locations. Figure 27 shows an image of a cracked pavement section from Fowler Avenue, FL captured on 24th June, 2007. Six sections, 1 through 6, of size 50 x 50 pixels were marked along the crack including the tip of the crack, from left to right. Using the method of homogeneous coordinates the corresponding 50 x 50 pixel sections were detected on the subsequently captured images of the same location (Figures 28(a), 29(a), 29(b)). For each of the six sections on the crack, texture distances between correspondence points were computed after the L5E5 operation.

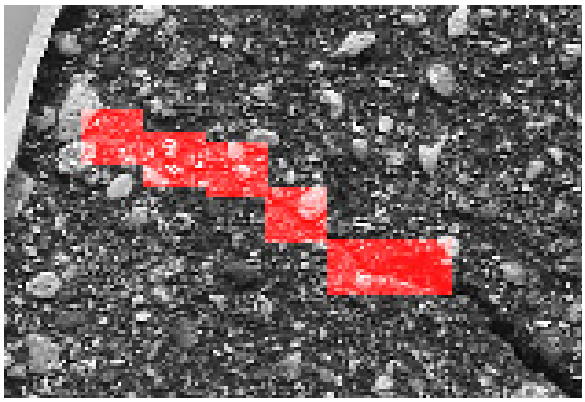

FIGURE 27 Image of Crack FOM1 (June 24, 2007), LM=50.2 klux

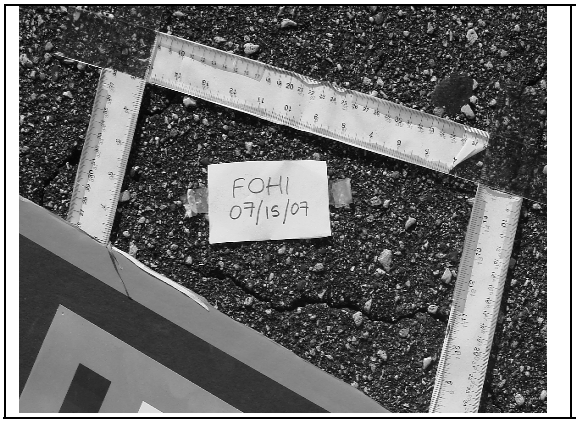

FIGURE 28(a) Image of Crack FOM1 (July 15, 2007), LM = 35.14 klux

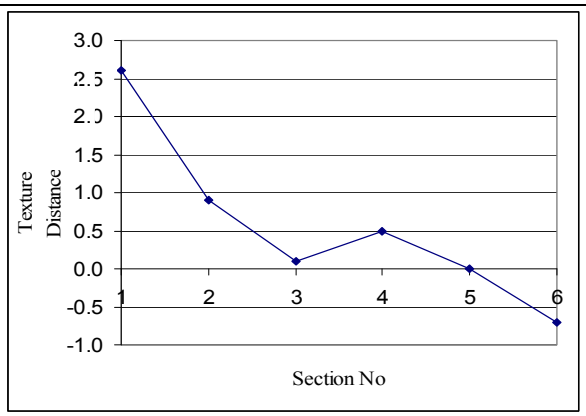

FIGURE 28(b) Texture Distance Between Sections in Figures 27 and 28(a)

FIGURE 29(a) Image of Crack FOM1 (September 16, 2007), LM = 38.97 klux

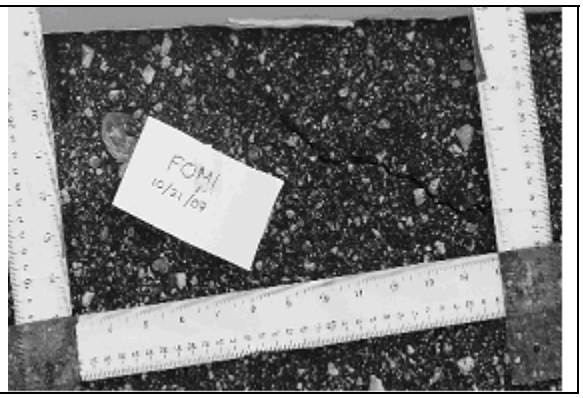

FIGURE 29(b) Image of Crack FOM1 (October 21, 2007), LM = 38.97 klux

Figure 28(b) corresponds to the texture distance distribution in the sections 1-6 in Figure 27 and the corresponding sections in Figures 28(a). From Figure 28(b), it can be noted that the maximum texture distance corresponds to section 1 of Figure 27 where the most significant texture change has occurred. Figure 30 is a plot of the same sections showing how the location of the maximum texture difference between the sections in Figure 27 and the corresponding sections in Figures 28(a), 29(a) and 29(b) changes gradually. It is noted that the section of maximum texture distance moves inside the crack as the crack propagates. When the sections were visually observed, it could also be noted that in addition to its growth in extent, there was also widening of the crack. When the changes in texture due to widening of the crack are higher than those due to the extension of the crack tip, the section corresponding to the maximum texture distance is shifted to the location where the widening of the crack has occurred. Hence the maximum texture distance criterion can be used to detect locations where the most significant changes have occurred on the pavement either due to widening or elongation.

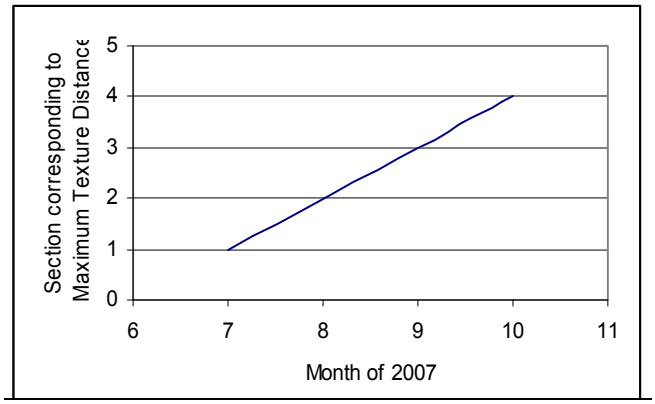

FIGURE 30 Sections Corresponding to Maximum Texture Distance

3.5 Application in Different Types of Defects

The changes in pavement texture caused by different types of defects in response to traffic and environmental conditions have unique characteristics. Therefore, by initially calibrating the texture measurements for the specific changes in image texture associated with given types of defects or rehabilitation such as patching, one would be able to use the images collected at different times to identify the variation in the pavement condition due to the above defects or rehabilitation techniques. This would preclude the necessity for using hazardous manual pavement surveys for such exercises. Such potential applications can be pursued when the image matching procedure described here is made more efficient practically.

3.6 Summary of Developments

1. The minimum texture distance criterion can be used to detect corresponding locations of images where the pavement distress condition does not change within times of capture.
2. When the pavement texture changes significantly due to changes in extent and severity of distress, the minimum texture distance concept must be replaced by the

method of homogeneous coordinates for detecting correspondences within or outside the distressed areas.

3. Detected correspondences between images can be used to monitor progression of wear at project-level pavement investigations.

The method of homogeneous coordinates, L5E5 masking operation and the maximum texture distance criterion can be combined to verify the significant mode of crack growth, i.e. elongation or widening, depending on whether the location of the maximum texture distance moves out of the crack or inside the crack.

CHAPTER 4 : USE OF DIGITAL IMAGE MODELING FOR EVALUATION OF CONCRETE PAVEMENT MACROTEXTURE AND WEAR

4.1 Importance of Surface Macrotexture Evaluation in Pavement Management

A major task of pavement management is to ensure adequate skid-resistance (friction) on all pavements in a network. Gradual degradation of skid-resistance on highways and runways can be attributed primarily to pavement texture changes due to traffic induced wear. Therefore, a safe level of skid resistance can be ensured by regularly monitoring pavement texture and taking corrective measures to restore degraded texture in a timely manner. Pavement friction is known to originate from two levels of texture; (1) macro-texture (depths from 0.5 to 20 mm and widths from 0.5 to 50 mm) and (2) micro-texture (depths from 0.001 to 0.5 mm and widths less than 0.5 mm) (Table 4 ISO 1997).

TABLE 4 Classification of Texture Based on Wavelengths (ISO, 1997)

Type	Wavelength (mm)	Description of texture
Micro-texture	$\lambda<0.5$	Formed by either fine aggregate particles (sand) or surface roughness of the large aggregate
Macro-texture	$0.5<\lambda<50$	Same order of size as coarse aggregate or tire tread elements
Mega-texture	$50<\lambda<500$	Same order of size as tire/road contact area
Unevenness	$500<\lambda$	Surface roughness that affects the ride comfort

4.1.1 Objectives of the Investigation

In the preliminary study reported in this dissertation, first the geometrical reflection properties of macrotexture would be used to model the digital image formation of pavement surfaces of uniform color. Second, the above imaging model would be used to identify (1) the changes in optical properties of digital images that reflect pavement wear and (2) the optimum specular setting required by the imaging system to detect the above changes. Then a simple experimental study would be set up to verify the theoretical findings. Finally, it would be illustrated how the detectable changes that occur in the optical properties of digital images due to the pavement wear can be correlated to degradation of macrostructure and consequent loss of skid-resistance.

4.1.2 Advances in Surface Characterization Using Digital Images

The identification of object characteristics from their images has been made possible by recent advances in the image processing technology. Tamura et al. (1978) modeled optical texture of a physically textured object using its reflection properties and illustrated how it facilitates image classification, image segmentation, and image encoding. Optical texture models have also been used to recreate depth and orientation of objects and to generate desired synthetic image textures by adjusting model parameters (Tamura et al. (1978)). It was shown by Shapiro et al.(2001) that the optical texture of pavement images can also be formed from image primitives of varying shape or by using stochastic assumptions. In the above work, pavement macrotexture and microtexture were considered to be composed respectively of relatively large and small optical texture primitives. The intensity of each pixel in the image space has also been considered a

random variable within a range of intensities defined by the neighboring pixels. Consequently, this relationship of interdependence of intensities has been modeled using the Markov random field theory to determine the pavement image texture parameters and hence evaluate the specific parameters relevant to pavement friction (Rado (1994)). Rado (1994) used the above model to correlate the macrotexture to image intensities of local neighborhoods using actual images of pavements and the corresponding mean texture depths measured from those pavement profiles.Consequently, this relationship of interdependence of intensities has been modeled using the Markov random field theory to determine the pavement image texture parameters and hence evaluate the specific parameters relevant to pavement friction (Rado (1994)). Rado (1994) used the above model to correlate the macrotexture to image intensities of local neighborhoods using actual images of pavements and the corresponding mean texture depths measured from those pavement profiles.

More recently Khoudeir and Brochard (2004) have studied the changes in image properties due to wearing of pavement surfaces based on the statistical properties of the image gradient, the curvature map of the gray level images, and the derivative of the autocorrelation function of several lines of the images. However in Khoudeir and Brochard (2004) work, the intensity of light reflection in a given direction was considered to be governed by the reflected angle only thus neglecting its significant dependence on the incident angle and the surface properties. In the work presented in this dissertation the intensities of incident and reflected light as well as the reflection properties of surfaces of uniform color are used in modeling the wearing of pavement macrotexture.

4.2 Modeling of the Pavement Image Formation Process

4.2.1 Selection of Surface Parameters for the Bidirectional Reflection Distribution Function (BRDF) Model

The Ward's reflection model described in Section 2.1.3 with the same parameters was used in this analysis also. In this analysis α was computed from the variation of surface slopes in the neighborhood surrounding the nodal point of interest. For the assumption of local specularity to be valid in the neighborhood of any node and the value of α to capture the microtexture, the nodal spacing was selected as 0.025 mm in both x and y directions (Table 3. Although theoretical modeling of the texture imaging can reach the microtexture level, the image resolution achieved by state-of-the-art pavement cameras is only 1mm. Thus, any refinement in the fineness of the nodal mesh beyond 0.5 mm would only make the computation of nodal α values more accurate and produce images that show more texture details than real images. Since the reflection at each local node is considered to be specular, ρ_s and ρ_d are assigned values of 1.0 and 0 respectively.

4.2.2 Simulation of the Pavement Texture Profile

In the modeling of images of pavement macrotexture, the pavement profiles were represented in terms of 3-D sine functions. This representation can be justified based on the principles of Fourier decomposition, whereby most pavement texture profiles can be approximated with a series (n) of finite 3-D sine waves varying in wavelengths and amplitudes as shown in Eqn. (37).

$$z = \sum_{i=1}^{n} amp_i \sin\left(\frac{2\pi x}{\lambda_i} + \frac{2\pi y}{\lambda_i}\right) \tag{37}$$

where λ_i and amp_i are the respective wavelength and amplitude of the i^{th} component.

4.2.3 Evaluation of the Reflectance of the Pavement Surface

The texture profile of the imaged pavement and the locations of the light source and the camera were defined using a 3D cartesian coordinate system (Fig. 31). Then the BRDF variation of the surface due to the direct illumination from the light source can be computed, disregarding the inter-reflection and illumination from other sources such as sunlight. Part of the light from the illuminating source gets reflected from every point on the pavement such as R (x,y,z), scatters due to the diffusivity caused by the slope variance (α) of the neighborhood of R and reaches different locations of the camera lens. Therefore, BRDF of R with respect to a number of small elements (ΔA_c) that constitute the camera lens area (A_c) must be evaluated and integrated to determine the average radiance from R with respect to the camera. It has been shown in the Appendix A that the average BRDF at R with respect to the entire camera can be determined as,

$$\rho(x,y,z)_{avg} = \left[\frac{1}{A_C}\iint_{r,\phi}\frac{\rho_d}{\pi} + \rho_s \frac{1}{\sqrt{\cos\theta_i \cos\theta_r}} \frac{\exp\left[-\tan^2\delta/\alpha^2\right]}{4\pi\alpha^2}\Delta A_C\right] \tag{38}$$

where, $\hat{h}$ = Unit vector bisecting the incidence and reflection directions (Fig. 1)

$\hat{n}$ = Unit vector normal to the surface at R (Fig. 1)

$\cos\delta = \hat{h}.\hat{n}$, $\cos\theta_i = \overrightarrow{RL}_u.\hat{n}$ and $\cos\theta_r = \overrightarrow{RP}_u.\hat{n}$

$\overrightarrow{LR}_u$ = Unit vector in the direction of incidence (Fig. 31)

$\overrightarrow{RP}_u$ = Unit vector in the direction of reflection (Fig. 31)

The appropriate expressions for the above vectors are also derived in the Appendix A. The BRDF at any point on the surface (i.e, R) with respect to camera aperture segments of 0.5 mm and 30^0 increments in the radial and angular directions respectively, can be evaluated numerically using Equation (38). The incident light from the source does not reach certain locations on the surface due to occlusion by the surface profile and similarly the reflected light from certain other locations is prevented from reaching the camera. Both of the above conditions were incorporated when the BRDF for imaged surface was evaluated using Equation (38).

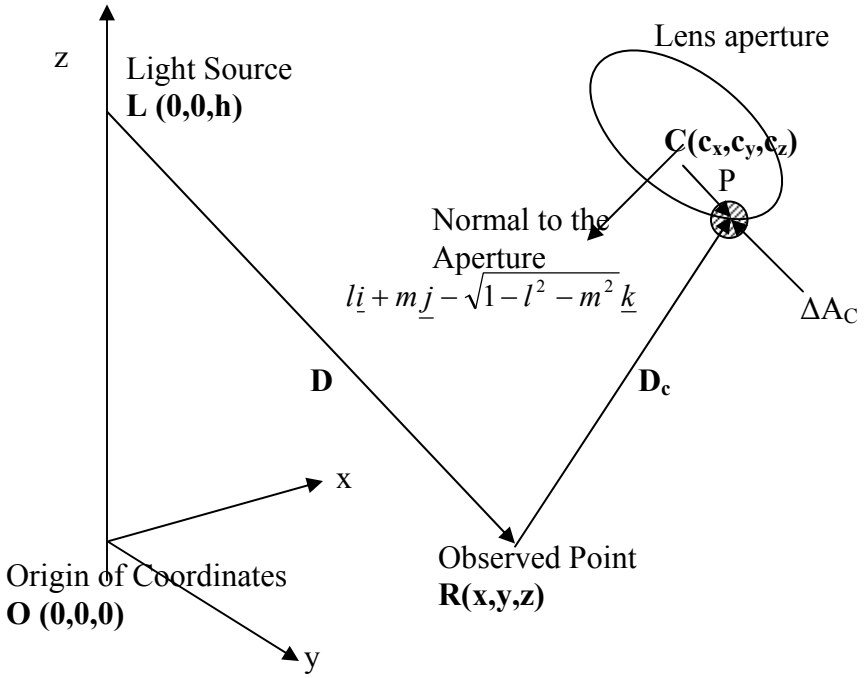

FIGURE 31 Illustration of the Imaging System Setup

4.2.4 Conversion of Pavement Radiance to Image Intensity

The image of a pavement feature is formed when the light reflected from that feature (object) enters the camera lens and refracts on to the CCD sensor. A schematic diagram of the optics of image formation is shown in Figure 32. The relationship (Eqn. 39)

between the radiance from any surface point (R) and the intensity of its image (ΔE) has been derived in the Appendix B.

$$\Delta E = \rho h^2 L^* \cos\theta_i . A_L . \frac{\cos\theta_L}{D^4} . \frac{\cos^3\theta_c}{f^2} . \Delta A_C \tag{39}$$

Where f, ρ, L^*, and θ_c are the focal length of the lens, BRDF at R with respect to one camera element ΔA_C, intensity of irradiance immediately below the light source (at Q), and the angle between the normal to the camera aperture and the line RC, respectively. The remaining symbols in Eqn. (39) are illustrated in Fig. 32.

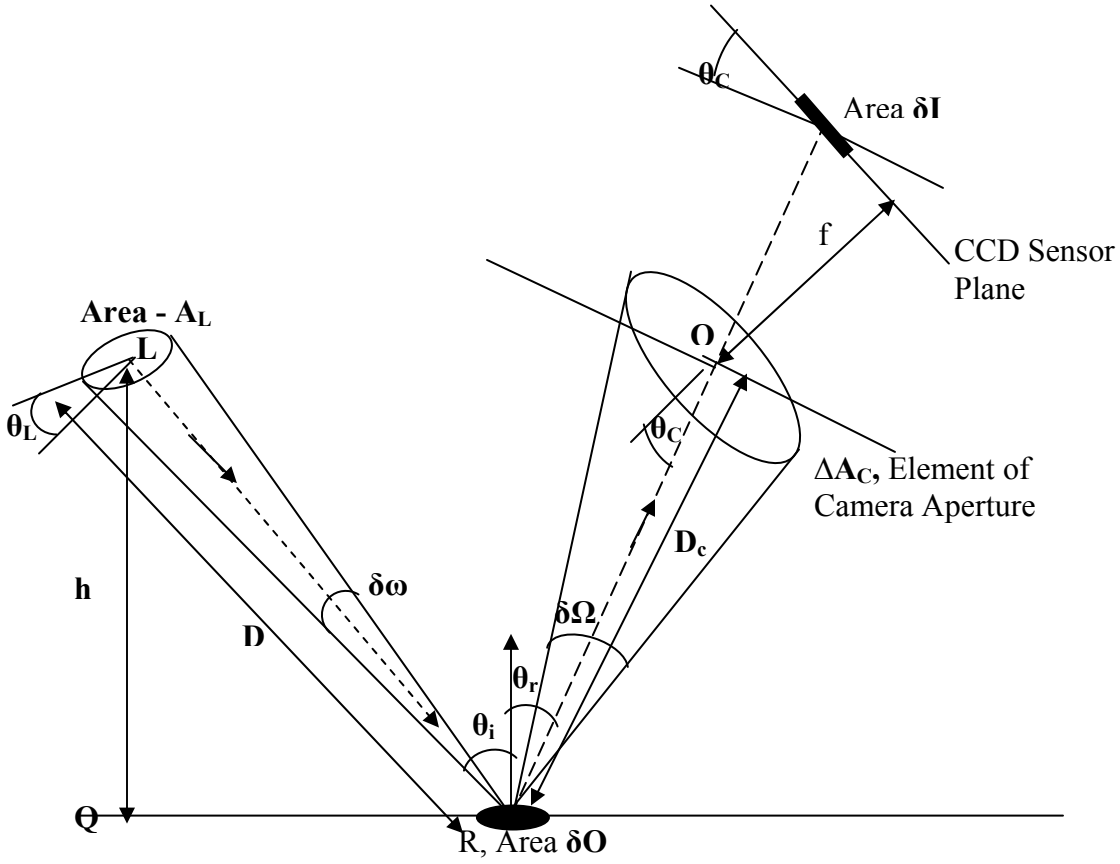

FIGURE 32 Illustration of the Image Formation Process

If the light source and the camera are placed at a relatively large height compared to the dimensions of the imaged area, θ_L and θ_C would not change significantly within one image. Furthermore, since h, L*, A_L and f are constants, Eqn. (39) can be re-written as,

$$\Delta E = K\rho\cos\theta_i \cdot \frac{1}{D^4}\Delta A_C \tag{40}$$

where K includes the constant quantities in Eqn. (39). Finally, the total intensity E of the image formed by the surface point R due to light entering the *entire* lens (of area A_c) can be determined by combining Eqns. (38) and (40) as

$$E = K\frac{\cos\theta_i}{D^4}A_C\rho(x,y,z)_{avg} \tag{41}$$

Therefore, Eqns. (38) and (41) can be used to obtain the pixel intensity distribution in the pavement surface image.

4.3 Experimental Verification of the Image Formation Model

The accuracy of the image formation model developed in Section 2.0 was verified experimentally using a single wavelength periodic surface (n=1, λ_1=6mm and amp_1=3mm in Eqn. (37)) molded from clay. The light source was set up above the molded surface with the normal to its surface intersecting the profile at a horizontal distance of 380 mm from it. The camera was placed 500 mm away from the light source and oriented in such a way that the normal lines to the camera aperture and the light source intersected the pavement profile at the same location. Then the surface was imaged at two different camera heights of 305 mm and 610 mm. The actual and simulated images corresponding to the two conditions are shown in Figures 33(a)-(f).

When comparing Figs. 33(a) with 33(b) and Figs. 33(d) with 33(e), it can be observed that the images created by the BRDF model (Eqns. (38) and (41)) resemble those of the actual surface. Furthermore, the images of the same surface mathematically simulated under the same lighting and imaging conditions using the Phong (1975) model programmed in a widely used computer graphics software, *Maya 7*, are also shown in Figs. 33(c) and 33(f). It is seen that Figs. 33(b) and 33(e) compare reasonably well with Figs. 33(c) and 33(f) as well. The pixel intensities of the synthetic (modeled) image closer to the camera were seen to be higher (Fig. 33(b)) as in the case with its experimental counterpart (Fig. 33(a)). However, Figs. 33(b) and 33(e) show that there is a sharp intensity reduction from the peak of the profile in the modeled images whereas the intensities of the experimental counterparts (Figs. 33(a) and 33(d)) decrease gradually from the peak. This can be attributed to the fact that the exact sinusoidal shape described by Eqn. (37) could not be achieved due to a minor flattening effect produced at the peaks during molding of the clay surface.

FIGURE 33(a) Actual Image of the Profile Taken at 305 mm Above the Surface

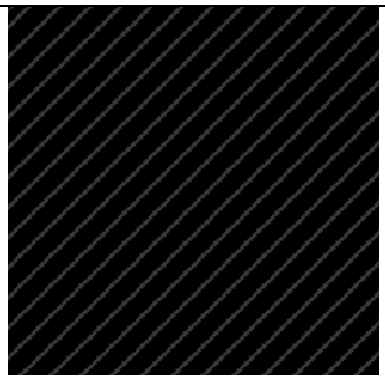

FIGURE 33(b) Modeled (Ward) Image of the Simulated Profile Corresponding to Figure 33(a)

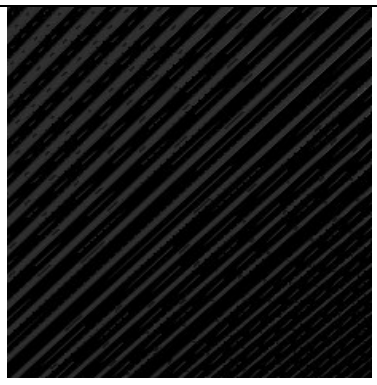

FIGURE 33(c) Modeled (*Maya*) Image of the Simulated Profile Corresponding to Figure 33(a)

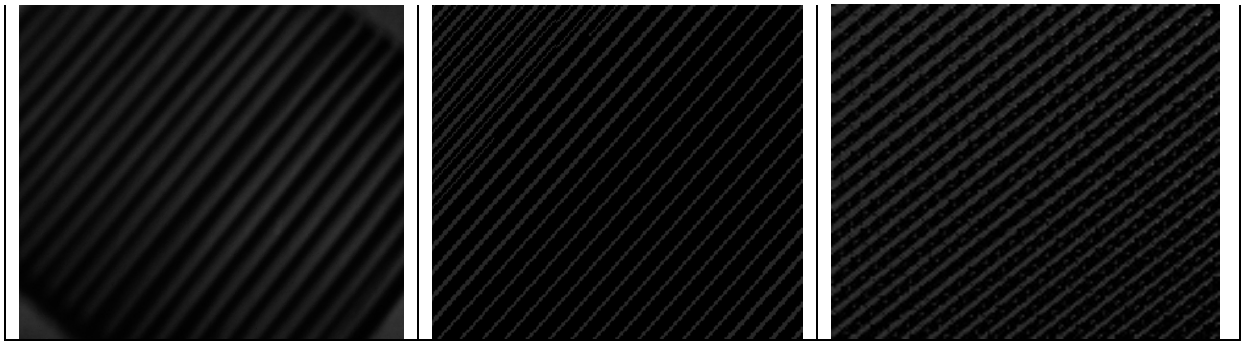

FIGURE 33(d) Actual Image of the Profile Taken at 610 mm Above the Surface

FIGURE 33(e) Modeled (Ward) Image of the Simulated Profile Corresponding to Figure 33(d)

FIGURE 33(f) Modeled (*Maya*) Image of the Simulated Profile Corresponding to Figure 33(d)

4.4 Application of the Image Model in Detection of Wear

In the next phase of the study, the new reflection model was applied to detect the degradation of texture in pavements. For this purpose, a 0.05m x 0.05m segment of a pavement surface was modeled mathematically with the light source and the camera placed on opposite sides of the normal to the center of the surface, 0.05 m apart from each other at heights of 0.5m and 1 m respectively above the modeled surface (Fig. 34(a)). Possible optimum locations of two such imaging systems in a potential field implementation of this technique are shown in Fig. 34(b). As implied in Fig. 34(b) the pavement wear detection can be limited to the wheel path areas where wearing of pavement texture due to traffic is predominant. Using the above setup, the reflection model described in Section 2.2 was used to create the corresponding images of the mathematically represented original and worn profiles, as described later in Section 4.2.

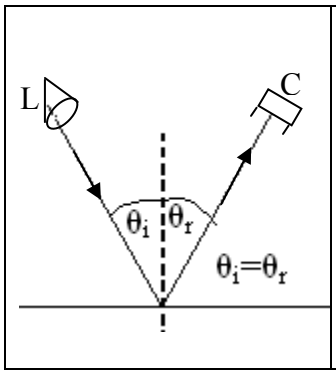

FIGURE 34(a) Specular Setup of the Imaging System

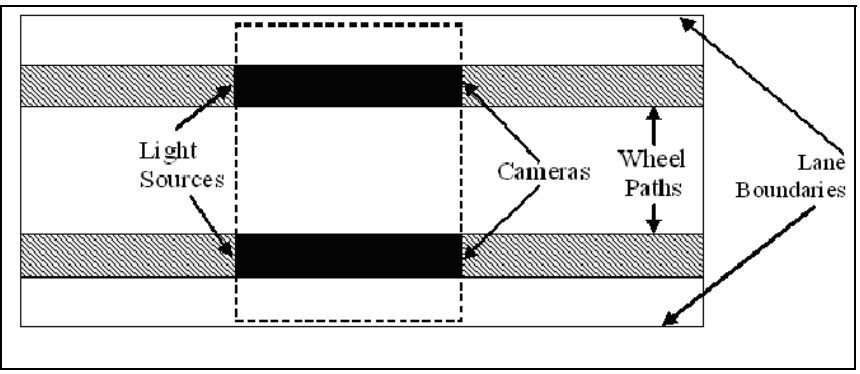

FIGURE 34(b) Optimum Arrangements of Light Source, Camera and Imaged Section

4.4.1 Tools for Assessing Pavement Wear Using Digital Images

Several image characteristics can be used for differentiation of digital images of new and worn out pavements and subsequent identification of the extent of degradation of texture and frictional properties. The normalized pixel intensity histogram of a digital image which depicts the statistical distribution of pixel intensities on the gray scale of 0 to 255 provides the simplest tool to compare and contrast images. Khoudeir and Brochard (2004) (Section 1.3) have used specific statistical properties and the autocorrelation function for this purpose. Alternatively, an appropriately defined *brightness* function of an image can also be employed as a more reliable measure for comparison of images. However, the perceived *brightness* of a given gray-scale intensity cannot be defined in a clear-cut manner due to the vagueness of intermediate intensities between black and white. To address this issue and define a reliable *brightness function*, researchers (Cheng et al., 1999) have considered image *brightness* as a fuzzy set.

The membership function ($\mu_{bright}(x)$) of the brightness fuzzy set can be defined in the gray intensity scale of 0 to 255 with three parameters ***a, b,*** and ***c***. As illustrated in Fig. 35, the

intensities less than ***a*** have zero membership and the intensities higher than ***c*** have a membership of 1, in the brightness fuzzy set. The degree of brightness for the intensities between ***a*** and ***c*** would vary gradually from 0 to 1. This variation can be represented using a standard S function described in Eqn. (42) (Cheng et al., 1999).

$$\mu_{bright}(x) = \begin{cases} 0, & x \le a \\ \dfrac{(x-a)^2}{(b-a)(c-a)} & a \le x \le b \\ 1 - \dfrac{(x-c)^2}{(c-b)(c-a)} & b \le x \le c \\ 1 & x \ge c \end{cases} \tag{42}$$

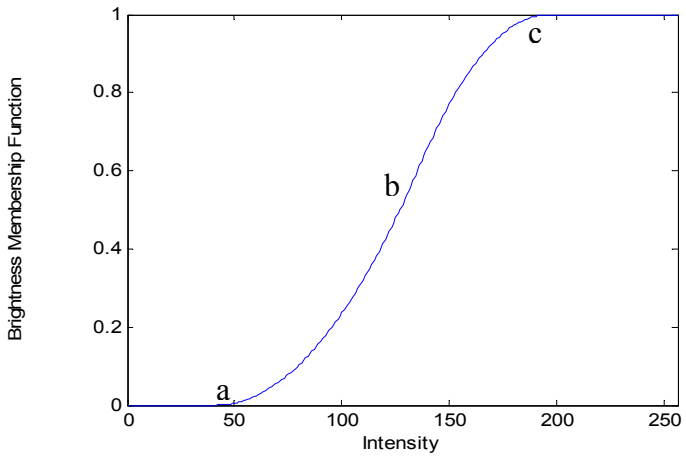

FIGURE 35 Illustration of the Brightness of Gray-Scale Intensities

Then the *brightness* of an image can be expressed as a probability measure as follows

$$P(bright) = \sum_{x=0}^{255} \mu_{bright}(x).p(x) \tag{43}$$

where *p(x)* is the probability of occurrence of any given intensity *x* in the evaluated image as displayed in its normalized histogram. The optimum values for parameters *a, b* and *c* can be found by maximizing the entropy of *brightness* (*H(bright)* in Eqn. 44) of a selected *standard* image.

$$H(bright) = -P(bright)\log(P(bright)) - (1 - P(bright))\log(1 - P(bright)) \tag{44}$$

In the current investigation a standard gray-scale target (Edmund, 2003) consisting of 17 evenly spaced patches with intensities between 0 and 255 (Fig. 36) was used as the standard image. With *p(x)* (Eqn. (43)) determined from the normalized intensity distribution of an image of the standard gray-scale target, the maximization of the brightness entropy function (Eqn. (44)) yielded the optimum *a, b* and *c* values of 45, 135 and 195, respectively. Then, the brightness evaluation of any other image can be performed using Eqn. (43) with *p(x)* obtained from its intensity histogram and $\mu_{bright}(x)$ evaluated from Eqn. (42) using the optimum *a, b* and *c* values determined above.

FIGURE 36 Standard Fifteen-Wedge Grayscale Target (Edmund, 2003)

4.4.2 Detection of Surface Wear Based on Image Brightness

4.4.2.1 Case 1 – Modeling of Single Sine Wave Profiles

The effect of texture wear on the *brightness* of the original and worn out images was investigated by modeling the images of different texture levels using the reflection model in Equations (41) and (44) under the light source and the camera positions illustrated in Figure 34(a). The brightness of the modeled images of single sine wave surface profiles (Equation 37) with predefined amplitudes (MTD) varying from 1 mm to 5 mm and wavelengths (average texture spacing) varying from 1 mm to 10 mm were determined using Equation (43) and plotted in Figure 37. From Figure 37 it can be observed that for a

constant wavelength the image brightness increases with decreasing mean texture depth (MTD) while for a constant MTD, the brightness increases with increasing wavelength. In both cases the increase in brightness can be attributed to the smoothening of the profile. Based on the above preliminary observations it was decided that the consideration of the brightness of pavement images captured under the specific conditions defined in this study (Fig. 34) could be pursued to detect surface wear.

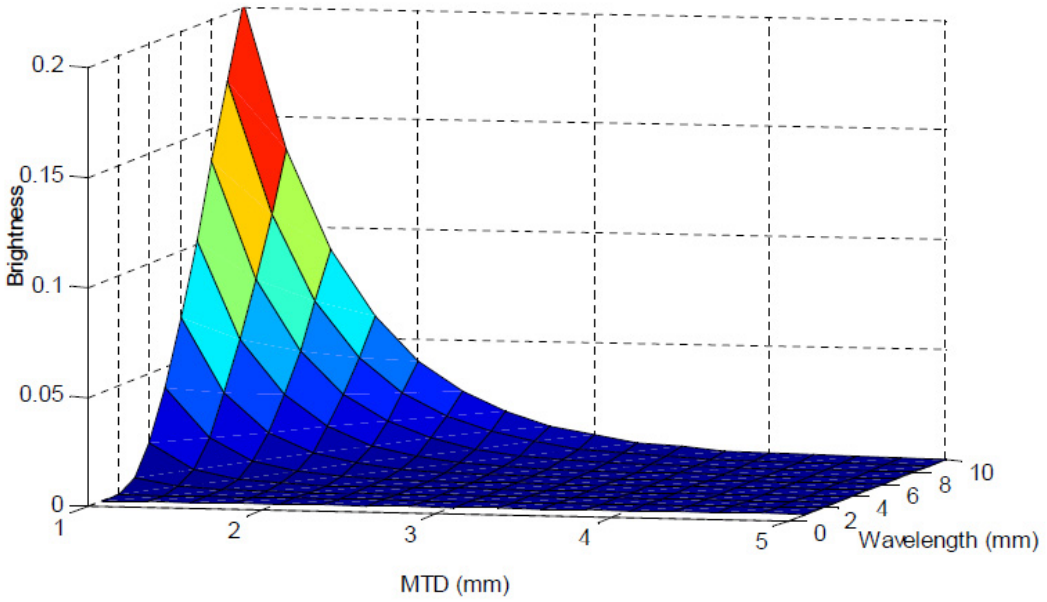

FIGURE 37 3-D Plot of Brightness Variation with Wavelength and MTD

4.4.2.2 Case 2 – Modeling of Complex Pavement Surface Profiles

In the next phase of modeling, two different and more complex profiles were composed of multiple sine waves to closely represent actual texture profiles of relatively rough and relatively smooth pavements. In both profiles the wavelengths were set to be 24, 12, 8, 6 and 4 mm. The wavelength to amplitude ratios (a_i in Equation 45) of the rougher profile were set to be 10, 8, 5, 3 and 2 respectively, while a_i for the smoother profile was set at a

constant value of 10 for all the wavelengths. Then the above profiles can be expressed mathematically as,

$$z = \sum_{i=1}^{5} (\lambda_i / a_i) \sin\left(\frac{2\pi x}{\lambda_i} + \frac{2\pi y}{\lambda_i}\right) \tag{45}$$

where

λ_i is the wavelength of ith sine curve (i = 1,5 mm)

a_i is the wavelength(λ_i) to amplitude (amp_i) ratio of ith sinusoidal curve

Three stages of wearing were simulated on the computer by degrading the portion of their profiles above the mean levels by 2%, 4% and 6% of the original profile heights respectively. The original and the worn surfaces of the smooth and rough profiles are shown in Figures 38(a) and 38(b) respectively. Figures 39(a) and 39(c) show the respective images of the original profiles shown in Figures 38(a) and 38(b) modeled using Eqns. (38) and (41), while Figures 39(b) and 39(d) show the modeled images of their 6% worn counterparts. The pair-wise comparison of Figure 39(b) with Figure 39(a) and Figure 39(d) with Figure 39(c) shows an increase in image brightness due to wearing. Fig. 40 is a plot of the brightness Vs the MTD for both pavement surfaces under different stages of wearing. It can be observed from Figure 40 that the images of the smoother surface are significantly brighter than those of the rougher surface at all stages of wearing. Furthermore, Fig. 40 shows the clearly increasing trends of brightness of both profiles as wearing proceeds. The above observations further support the increasing trend of brightness that was observed in Figs. 37 due to smoothening of single sine waves. In summary, the results indicated in Figs. 37-40 demonstrate the viability of setting up an optical imaging system in the manner specified in Fig. 34 to identify the level of macrotexture degradation on a pavement.

4.4.3 Experimental Verification of Image Brightness Variation due to Wearing

In the final phase of the investigation, the theoretical relationship between image brightness and the extent of wear developed in Section 4.2 was experimentally verified using a 460 mm diameter laboratory concrete specimen made to be compatible with the Circular Track Meter (CTM) (ASTM E 1845-01). The above concrete specimen was grooved at uniformly spaced intervals to obtain the textured surface seen in Fig. 41(a). Then, four 50x50 mm sections evenly spaced out along the CT meter track were earmarked on it as test sections where the experimental results could be averaged to remove any bias due to texture variation. These individual sections were then imaged using the same optical settings used in the theoretical study. Later, the surface of the concrete specimen was gradually worn with sand paper and the worn sections were re-imaged under the same lighting conditions. The CT meter profiles for the original and worn profiles are shown in Figure 42 from which the average MTD can be calculated at each wearing stage as shown in Table 5.

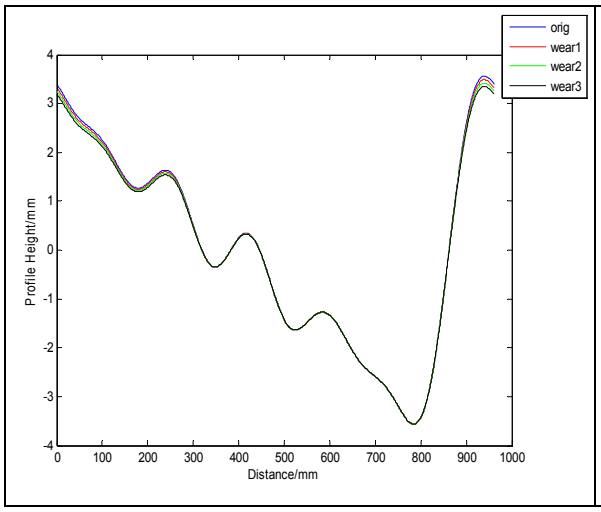

FIGURE 38(a) Wearing of Smooth Profile

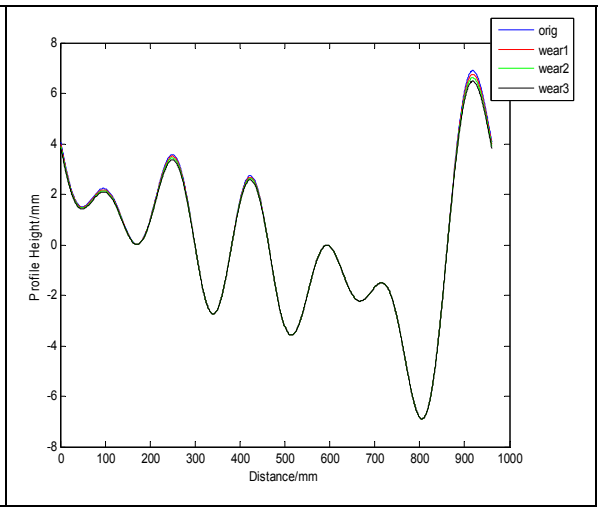

FIGURE 38(b) Wearing of Rough Profile

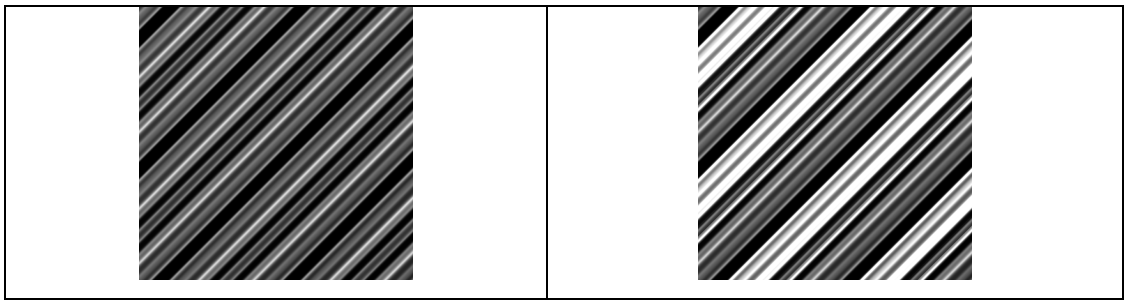

FIGURE 39(a) Synthetic Image for the Original Profile of Figure 38(a)

FIGURE 39(b) Synthetic Image for the Worn Profile (Wear 3) of Figure 38(a)

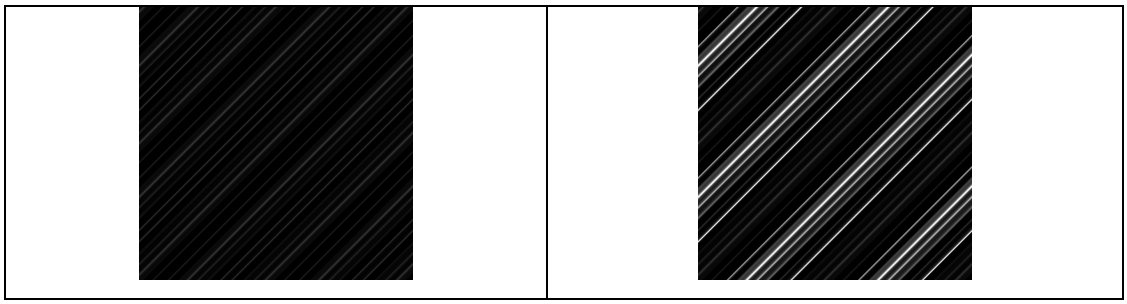

FIGURE 39(c) Synthetic Image for the Original Profile of Figure 38(b)

FIGURE 39(d) Synthetic Image for the Worn Profile (Wear 3) of Figure 38(b)

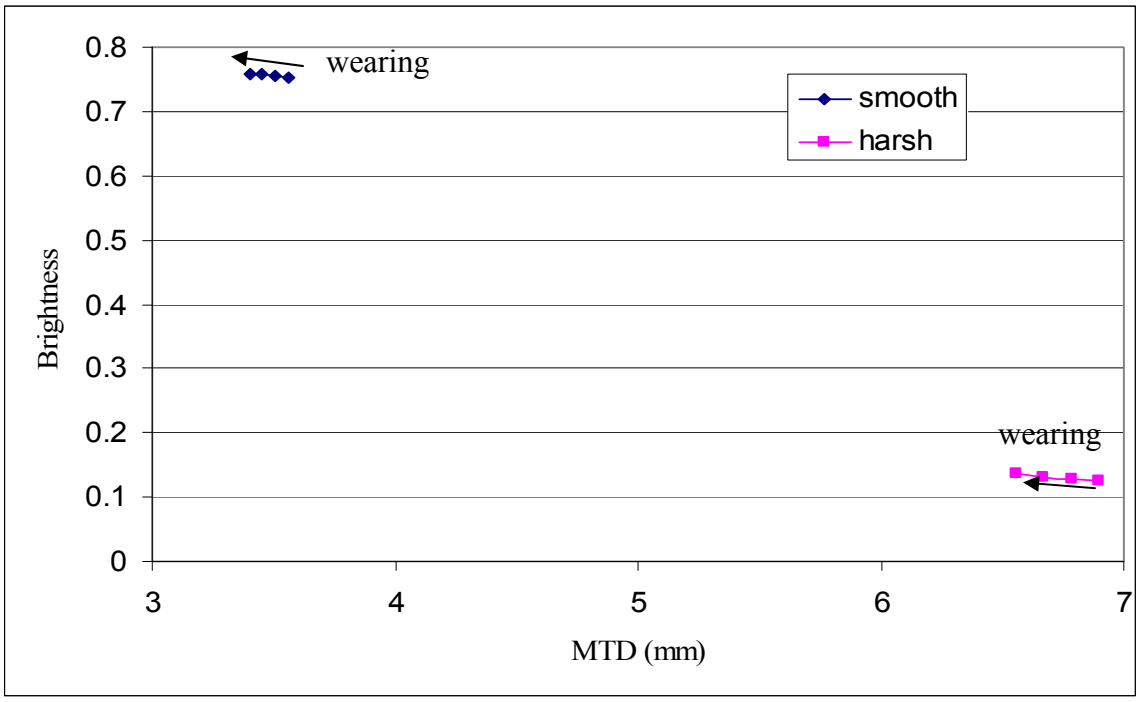

FIGURE 40 Brightness Variation of Smooth and Rough Pavement Surfaces due to Wearing (Theoretical Modeling Results)

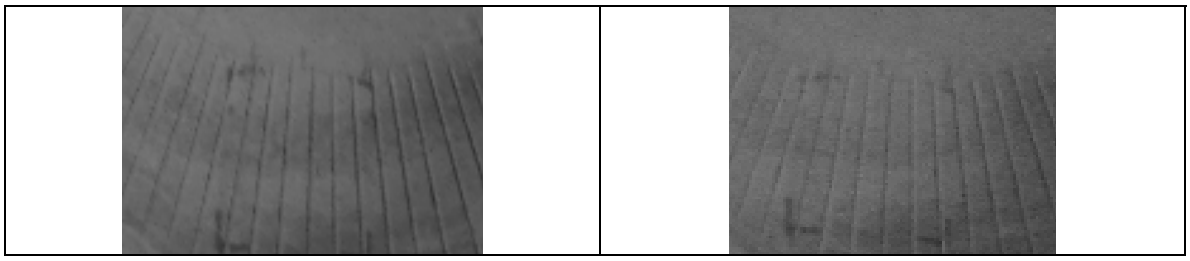

FIGURE 41(a) Original Image of the 50mm x 50 mm Section

FIGURE 41(b) Image of Section in Figure 41(a) after Wearing

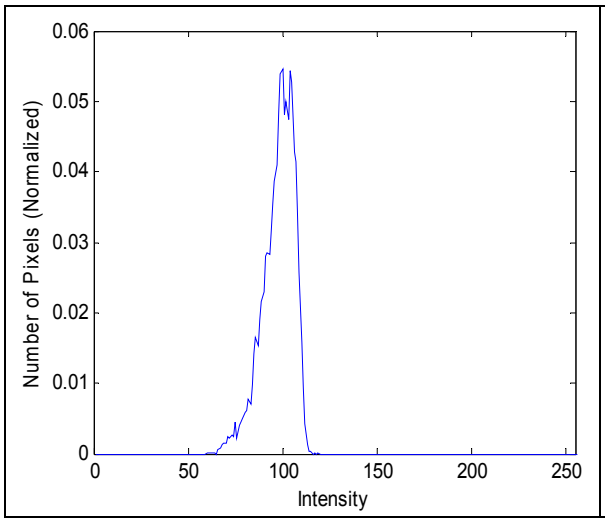

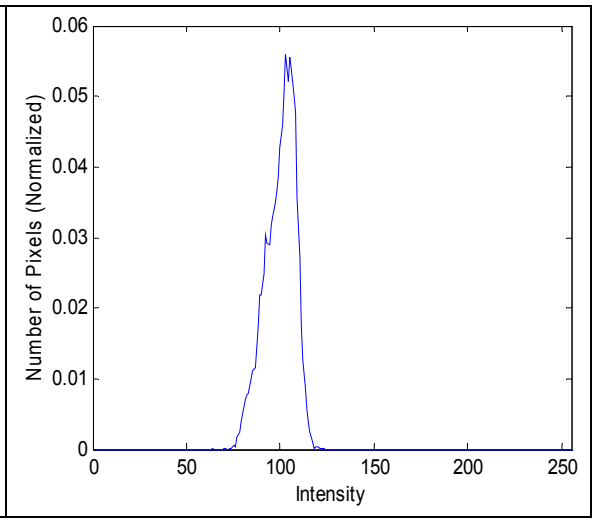

FIGURE 41(c) Image Histogram for Original Section Shown in Figure 41(a)

FIGURE 41(d) Image Histogram for Worn Section Shown in Figure 41(b)

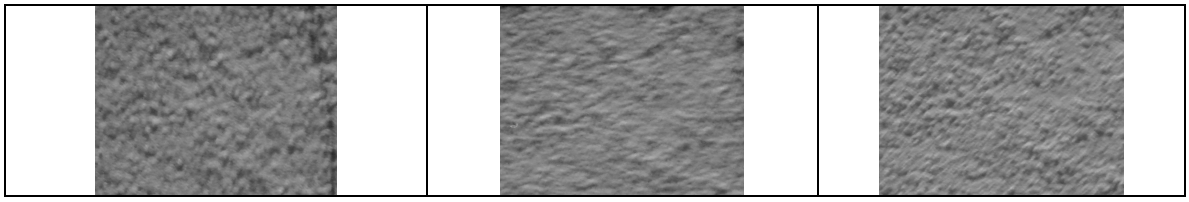

FIGURE 41(e) Original Pavement (Brightness = 0.3102)

FIGURE 41(f) After Stage 1 Wearing (Brightness = 0.3680)

FIGURE 41(g) After Stage 2 Wearing (Brightness = 0.3852)

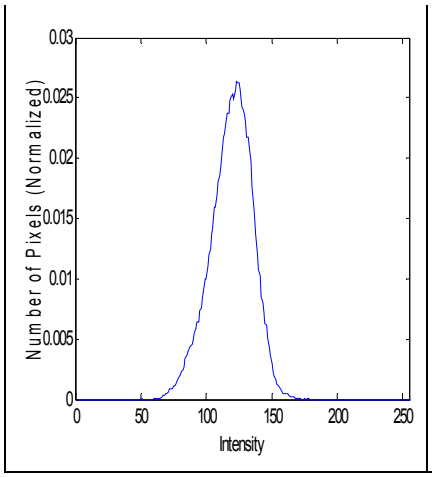

FIGURE 41(h) Image Histogram for Original Section Shown in Figure 41(e)

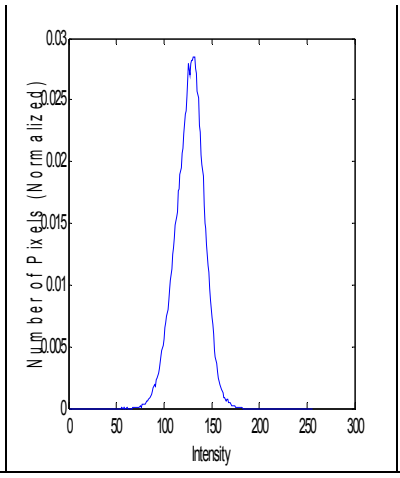

FIGURE 41(i) Image Histogram for Worn Section Shown in Figure 41(f)

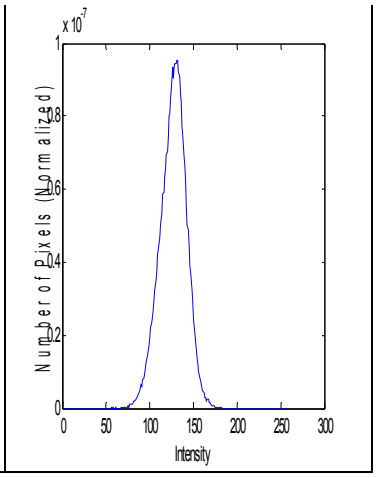

FIGURE 41(j) Image Histogram for Worn Section Shown in Figure 41(g)

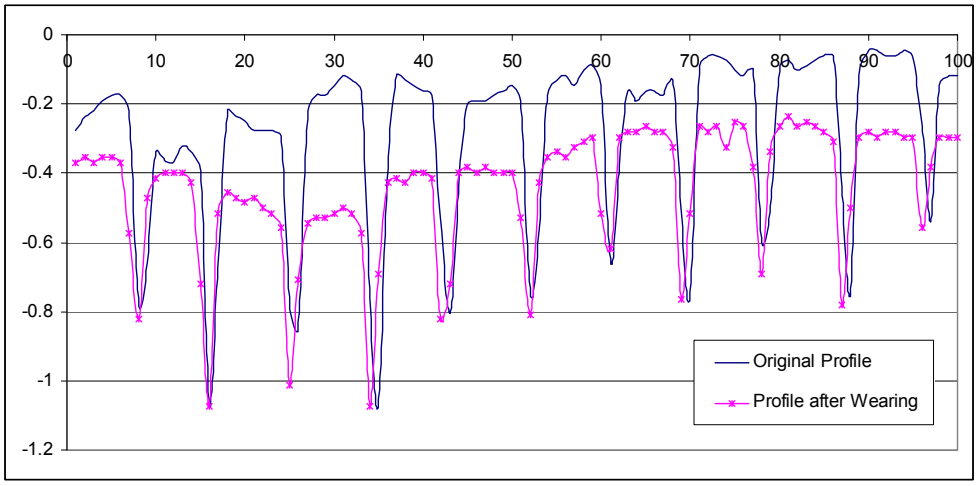

FIGURE 42 Circular Track Meter Results Showing the Variation of Cement Surface Profile due to Wearing

Images of the original and worn conditions of one of the four selected sections are shown in Fig. 41 with the corresponding intensity histograms. Comparison of the image histograms of Figures 41(c) and 41(d) show how the overall image intensities have increased slightly due to wearing. The computed average brightness values of the images are also shown in Table 5. From the results in Table 5 and the corresponding plot in

Figure 43, it can be observed that the brightness of the images of the four sections have increased due to wearing. Hence it can be concluded that the theoretically predicted increase in image brightness due to wearing is supported by the above experimental results.

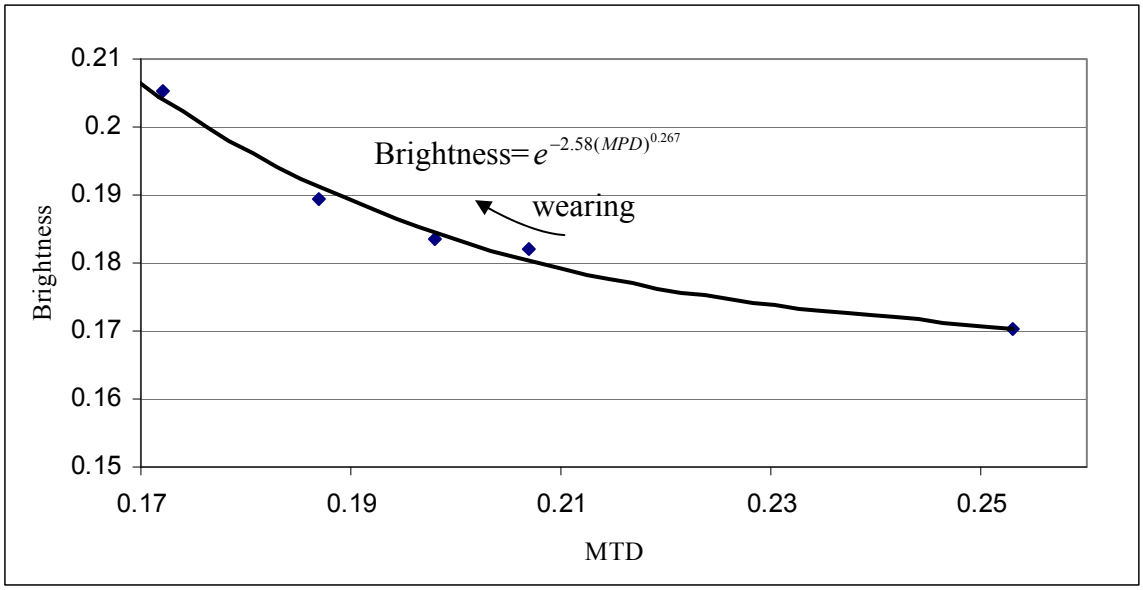

FIGURE 43 Variation of Brightness with MTD

4.4.4 Application of Image Brightness to Evaluate Pavement Friction

The experimental relationship obtained in Fig. 43 between the image brightness and MTD of a given surface can be calibrated using Equation (46).

$$B = e^{-k(MTD)^n} \tag{46}$$

where k and n are assumed to be constants for given pavement and lighting conditions. For the specific Brightness Vs MTD data set in Fig. 43, one obtains,

$$B = e^{-2.58(MTD)^{0.247}} \tag{47}$$

On the other hand, the Skid Number (SN) (ASTM E 1960-03) of a pavement can be evaluated using as,

$$SN = SN_0 e^{-\frac{sV}{S_p}} \quad (48)$$

where, s and V are the slip ratio and the speed of measurement. SN_0 is the friction measurement corresponding to static conditions. For the Locked-Wheel Friction Testers (LWST) (ASTM E 274-06) and DFTs (ASTM E 1911-09a), s=100%. Also, S_p, the speed constant, can be related to the Mean Profile Depth (MPD) as,

$$S_p = a + b(MPD) \quad (49)$$

where a and b are constants dependent on the method used to evaluate macrotexture. For the CT meter measurements, ASTM E 1960-03 recommended values are a=14.2 and b=89.7.

TABLE 5 Brightness Variation due to Wearing

Surface Description	Mean Texture Depth (MTD) – mm	Brightness of Images
Originally grooved	0.253	0.1702
After wearing stage 1	0.207	0.1821
After wearing stage 2	0.198	0.1834
After wearing stage 3	0.187	0.1894
Smooth surface	0.172	0.2053

If it is assumed that MTD and MPD of a profile to be approximately the same, the skid-number (SN) of a pavement measured with the LWST or DFT can be related to the

brightness of the corresponding images by combining Equations (46), (48) and (49) as follows

$$SN = SN_0 e^{\left[-b\left(\frac{-\ln B}{k}\right)^{1/n} - a\right]^{V}} \quad (50)$$

Finally, Equation (50) can be used to calibrate the relationship between the predicted SN at different stages of wearing of a given concrete pavement and the brightness (B) of the corresponding images. As an example, let the LWST measured SN of the initially unworn concrete specimen for which the image Brightness and MTD variation is defined in Fig. 43 (with k=2.58 and n=0.267), be 42. Then the variation of SN with the brightness of images captured at different stages of wear shown in Table 5 can be evaluated using Eqn. (50). This variation is illustrated in Figure 44 for the standard measurement speed of 65 km/hr.

The above example illustrates the need for calibrating Equation (50) to determine the specific values of SN_0, k and n applicable for a given pavement and a lighting system, prior to field implementation of the developed methodology on that pavement. Two initial LWST measurements and brightness evaluations of the corresponding images would suffice for this purpose.

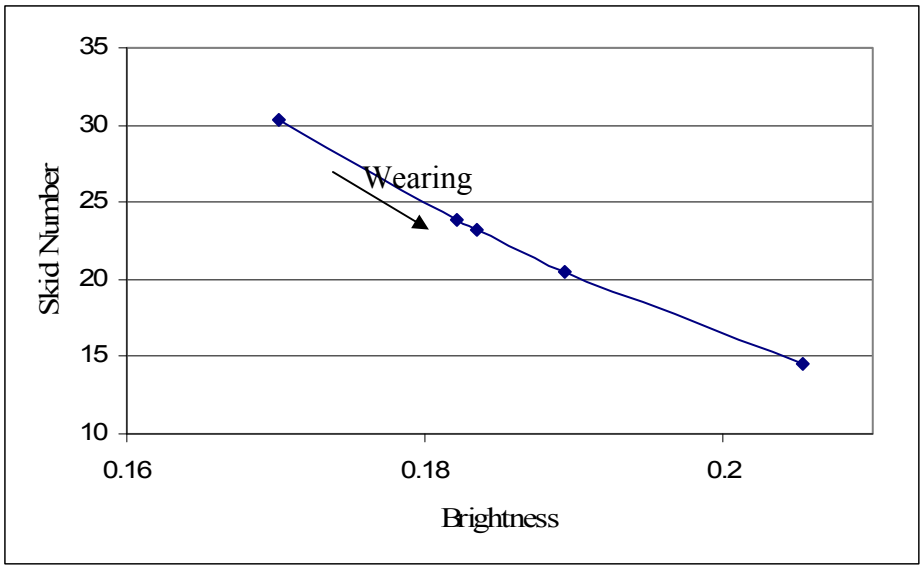

FIGURE 44 Variation of Skid Number with Brightness

4.5 Limitations of the New Technique

A limitation of the developed technique is its inapplicability on wheel paths where the deposition of tire rubber camouflages the texture, thereby offsetting increase in brightness in the images due to wear. In addition, the images created using the geometrical and reflection models could differ from the actual images due to camera artifacts and other types of noise. Hence the images collected from survey vehicles have to be pre-processed to remove any noise before they are used to detect the changes in brightness. Another possible limitation could be the complexity of the actual illumination conditions at the time of image capture. This effect can be especially pronounced when images are collected during daytime in the presence of sunlight and inter-reflections from other sources which are not considered in the modeling. However, this issue can be overcome by imaging during the night time when the imaged pavement surface would be illuminated mostly under the influence of the probe light attached to the evaluation

vehicle. Finally, in this preliminary analytical investigation and its companion experimental verifications, the image intensity contrasts were predicted based on the surface relief variations only, thus disregarding effects of color variation introduced in the radiant light by different constituent materials. This issue would be critical in the application of this technique to detect wear in asphalt pavements in particular, which constitutes aggregate and binder with contrasting colors. However, this technique can be refined further to incorporate color variations in the BRDF models (Amarasiri et al., 2010).

CHAPTER 5: CONCLUSIONS

In the first part of the study, variations in Bidirectional Reflectional Distribution Function (BRDF) at surface discontinuities were used to model digital images of longitudinal and transverse cracks and joints in concrete pavements. Ward's isotropic model was chosen to express the BRDF because of its simplicity and the parameters that are physically meaningful. The theoretical formulation was simplified by assuming homogeneity and isotropy in concrete pavement surfaces and regular geometry in surface discontinuities. It was shown that the reduction in pixel intensities which produces a color contrast at the discontinuities could be modeled successfully in order to obtain information on the depth of cracks. For calibration and experimental verification of the model, experimental cracks of varying severity and depths were formed in a concrete pavement. In the calibration process, the model parameters (diffusive and specular reflectances and the local slope variation) were determined by comparing the pixel intensity distributions of the modeled cracks and joints with their experimental counterparts. It was found that invariant model parameters could be used to model cracks and joints on a given concrete pavement. The calibrated model was able to produce additional images of cracks and joints that resembled their experimental counterparts to a reasonable degree in terms of both contrast in appearance and pixel intensity distributions within cracks. Another attractive feature of the new formulation is that the maximum pixel intensity reduction within a crack could be expressed in terms of the crack width and depth using an analytical relationship. It was also illustrated how this analytical relationship provides a convenient

basis for predicting the crack depths based on crack widths and the pixel intensity contrast within the crack, thus precluding the need for time consuming processing. In the present study only crack widths up to 10 mm were modeled. Obviously one can foresee no issue with cracks of higher widths. Infact, even a better accuracy in predicting the depth of relatively wide cracks is speculated. However, for crack widths smaller than 1 mm (hairline cracks), identification depends on the resolution of the camera and the accuracy would be lower due to lower contrast in intensities within an adequate width. In order to obtain more accurate results the assumption of homogeneity must be replaced with means of modeling the random variation in reflection properties particularly inside the cracks. The new technique shows definitive potential as an expedient tool for evaluation of shallow crack depths useful in rehabilitation decision-making and differentiation of cracks from other surface irregularities in open graded surface courses and joints in concrete pavements. Hence it would readily supplement the existing crack evaluation software as an additional tool.

In the second part of the study accurate monitoring of the development of pavement distress such as cracking and wear was identified as vital in project level pavement evaluations. This is especially the case when a significant change in the crack rating or skid number is observed in a given pavement section between two consecutive surveys, or when the durability of different surface mix types have to be compared. However, for these applications to be efficiently implemented, the same image sections collected at different times must be matched manually or automatically.

The optical texture characteristics of pavement images change due to the formation of new distresses and growth of existing distress. Since manual correspondence at pixel level would be extremely tedious, tools for evaluating optical texture changes in pavement images would be quite useful in pavement management. Prior to texture distance computations, appropriate texture masks have to be applied to highlight the prominent texture features. When texture measures are computed, determining the approximate size of the texture primitives of a pavement is important. In this regard, the application of the Scaled Scattering Index (SSI) in determining the size of a homogeneous section was illustrated. SSI produced consistent results for both asphalt and concrete pavements showing that the primitive texture size is 4x4 pixels. In addition, the SSI relationship correctly reflected the artificial line texture that occurred every 10-15 pixels in concrete pavements. However, it was found that the use of a 15x15 pixel window was more practical than a 4x4 window for masking operations.

The concept of *minimum* texture distance was shown to be effective in matching areas in images where no significant texture changes have occurred. It was also demonstrated that the correspondence (matching) of images can be used to monitor pavement wear on an accurate basis. The investigation also revealed that when locating corresponding points on the distressed areas, homogeneous coordinates concept can be used effectively, irrespective of the likelihood of significant texture changes. The concept of *maximum* texture distance was shown to be effective in identifying the significant mode of crack growth; elongation or widening. In contrast to existing computational techniques that classify cracks and evaluate them in relatively large pavement sections based on

AASHTO and other standard protocols, the newly introduced computational techniques would be useful in fine monitoring of limited distressed pavement sections required in project-level and quality assurance investigations.

In the third part of the study, a pavement image modeling technique was developed to demonstrate that changes in pavement macrotexture and skid resistance can be monitored using quantifiable optical properties of digital images captured by a well designed imaging system at an optimum location relative to the pavement. In this technique, the simplified Bidirectional Reflection Distribution Function (BRDF) model with physically meaningful parameters was used to transform the macrotexture of a pavement surface to the corresponding images captured by a digital area-view camera. This modeling technique was first verified by matching the theoretically simulated images of a single wavelength 3-D sinusoidal surface with those of a geometrically similar experimentally molded surface. Next the images of a family of 3-D single sine waves with varying amplitudes and wavelengths were modeled to explore specific image characteristics that would detect surface smoothening caused by changes in the mean texture depth or the texture spacing (wavelength). The above investigation was also extended to include appropriate combinations of 3D sine curves that resemble actual pavement surfaces with different macrotexture levels. Modeling of surface wear consistently revealed monotonic increases in the *brightness* of the corresponding images.

Modeling results were verified experimentally using a concrete specimen compatible in size with the Circular Track Meter (CTM) and worn out in stages using sandpaper.

Processing of the images of the original and worn specimens confirmed the definitive increase in image *brightness* due to wearing. It was demonstrated that once the brightness variation trend of the images corresponding to initial stages of wearing of a given pavement is established, the model can be calibrated to determine the extent of pavement wear at any future stage based on evaluating the brightness of the relevant images. In addition, the conventional correlation between the skid number and MTD of a pavement was employed to illustrate how the new technique can be extended to predict the degradation of skid resistance, based on evaluating the brightness of pavement images. Meanwhile, the use of devices such as Locked-wheel skid testers is impractical for periodic *network level screening* of highway pavements for inadequate skid resistance. On the other hand, with further refinement of the methodology introduced in this study, if the evaluated brightness of pavement images routinely collected by various transportation agencies can be used to predict the degradation of skid-resistance of pavements, it would provide a valuable tool for network-level screening. Furthermore, since this texture modeling technique can reach even the microtexture of pavements, it can be employed to investigate the types of information on pavement microtexture that could also be revealed by enhancing the camera resolution.

REFERENCES

1. AASHTO (2001), "Standard Practice for Quantifying Cracks in Asphalt Pavement Surface" (No. PP 44-01), American Association of State Highway and Transportation Officials, April, Publication No. HM-20-COM

2. Amarasiri S.P., Gunaratne M., Sarkar S. and Nazef A. (2007). "Characterization of the texture properties of pavement images as an aid to automated comprehensive pavement evaluation." Presented at the *Transportation Research Record*.

3. Amarasiri S.P., Gunaratne M., and Nazef A. (2009). "Differentiation of cracks from surface irregularities in Open graded friction course (OGFC) Pavements using digital image modeling" Presented at the *Transportation Research Record*.

4. Amarasiri S., Gunaratne M., Sarkar S and Nazef, A. (2009) "Use of Optical Reflection Properties and Digital Images for Evaluation of Pavement Macrotexture and Wear", In review by the ASCE Journal of Transportation Engineering.

5. Ayenu-Prah, A. and N. Attoh-Okine (2008) "Evaluating Pavement Cracks with Bidimensional Empirical Mode Decomposition", Journal on Advances in Signal Processing, Vol 2008

6. ASTM Standard E 1845-01 "Standard Practice for Calculating Pavement Macrotexture Mean Profile Depth" ASTM International, West Conshohocken, PA.

7. ASTM Standard E 1911-09a "Standard Test Method for Measuring Paved Surface Frictional Properties Using the Dynamic Friction Tester", ASTM International, West Conshohocken, PA.

8. ASTM Standard E 1960-03 "Standard Practice for Calculating International Friction Index of a Pavement Surface", ASTM International, West Conshohocken, PA.

9. ASTM Standard E 274-06 Standard Test Method for Skid Resistance of Paved Surfaces Using a Full-Scale Tire, ASTM International, West Conshohocken, PA

10. ASTM Standard E 303-93 "Standard Test Method for Measuring Surface Frictional Properties Using the British Pendulum Tester", ASTM International, West Conshohocken, PA.

11. Balmer, G. G. (1978). "Pavement texture: Its significance and development." *Transportation Research Record. 666*, Transportation Research Board, Washington, D.C., 1-6.

12. Britton, S.C., Ledbetter, W.B., and Gallaway, B.M. (1974). "Estimation of skid numbers from surface texture parameters in the rational design of standard reference pavements for test equipment calibration." *J. Test. Eval.*, 2(2), 73-83

13. Canny J, 1986, A computational approach to edge detection. *IEEE Trans. Pattern Analysis Mach. Intell. PAMI-8* 6, November, pp. 679–697

14. Cheng, H.D., Chen, J.R., Glazier, C., and Hu, Y.G. (1999). "Novel approach to pavement distress detection based on fuzzy set theory." *J. Comput. Civ. Eng.,* 13(4), 270-280.

15. Cheng, H.D., Wang, J.L., Hu, Y.G. (2001) "Novel approach to pavement cracking detection based on neural network" *Assessing and Evaluating Pavements*, Issue 1764, pp. 119-127.

16. Chou J, W.A O'Neill, and H.D. Cheng (1994) "Pavement Distress Classification using Neural Networks", Systems, Man, and Cybernetics, "Humans, Information and Technology'., 1994

17. Cook R.L. and Torrance. K. E. (1981) Reflectance Model for Computer Graphics. Computer Graphics, 15(3), Proceedings, Annual Conference Series, ACM SIGGRAPH, pp. 307-316.

18. DSC 111 (2008). http://www.laserfocusworld.com/display_article/318554/12/none/none/News/ROAD-MONITORING:-Laser-system-monitors-slipperiness-of-roadway

19. Edmund Industrial Optics (2003), Large Garyscale target, http://www.edmundoptics.com/onlinecatalog/displayproduct.cfm?productID=1329.

20. Ergun, M., Lyinam, S., and Lyinam, A.F. (2005). "Prediction of road surface friction coefficient using only macro- and microtexture measurements." *J. Transp. Eng.,* 131(4), 311-319

21. Gang W., Liang X., and He A.Z. (2007) "The FRIT-based image enhancement algorithm for faint pavement cracks", *Lasers in Engineering*, Volume 17(5-6), pp. 295-310

22. Gendy A El, and Shalaby A. (2007). "Mean Profile Depth of Pavement Surface Macrotexture Using Photometric Stereo Techniques", *Journal of Transportation Engineering*, Vol. 133, No. 7, pp. 433-440.

23. Germain C, Da Costa J.P., and Baylou, P. (2000) "Multiscale Estimation of Textural Features. Application to the Characterization of Texture Anisotropy", *Proceedings of the International Conference of Pattern Recognition*, IEEE Computer Society Washington D.C., Volume 3, pp 923-926.

24. Gould D (2003). "Complete Maya Programming: an extensive guide to MEL and the C++ API", Morgan Kaufman Publishers

25. Gunaratne M., Amarasiri S and Nasseri, S. (2008) "Investigation of Automated and Interactive Crack Measurement Systems", Final Report Submitted to the Florida Department of Transportation, Project No. BD-544-36

26. He X.D., Torrance K.E., Sillion F.X., and Greenberg D.P. (1991) A Comprehensive Physical Model for Light Reflection. Computer Graphics, 25(4) Proceedings, Annual Conference Series, ACM SIGGRAPH, pp. 175-186.

27. Huang, Y. and Xu B. (2006). "Automatic Inspection of Pavement Cracking Distress", *Journal of Electronic Imaging*, 15(1)

28. International Organization for Standardization (ISO) (1997). "Characterization of pavement texture by use of surface profiles Part 1: Determination of mean profile depth," *International Standard No. 13473-1*.

29. Jeyisanker K., (2009). "Analysis of Water Seepage through Earthen Structures Using the Particulate Approach", Doctoral Dissertation, University of South Florida.

30. Joshi S., Sancheti S., and A. Goyal (2007) Specular and diffuse measurements of multipath from various terrain surfaces at 35 GHz, The Institution of Engineering and Technology, Antennas Propag., 1, (2), 496-500.

31. Kautz J., and M. D. McCool (1999) Interactive rendering with arbitrary BRDFs using separable approximations, Eurographics Rendering Workshop, pp. 247:260.

32. Khoudeir M. and Brochard J. (2004). Roughness Characterization through 3D Textured Image Analysis: Contribution to the Study of Road Wear Level, Computer-Aided Civil and Infrastructure Engineering, Vol. 19, pp 93-104

33. Lee, H., and J. Kim. (2005) Development of a Crack Type Index, *Transportation Research Record 1940*, TRB, Washington, D.C., pp. 99-109.

34. Leu, M.C., and Henry, J.J. (1978). "Prediction of skid resistance as a function of speed from pavement texture." *Transportation Research Record. 666*, Transportation Research Board, Washington, D.C., 7-13.

35. Liu F., Xu G, Yang Y, Niu X, and Y Pan (2008) "Novel Approach to Pavement Cracking Automatic Detection Based on Segment Extending" International Symposium on Knowledge Acquisition and Modeling, IEEE, pp. 610-614

36. LRIS (Laser Road Imaging System). (2008). http://www.ino.ca/medias/pdfs/publications/technical/3D-sensors/LRIS_Laser_Road_Imaging_System_PRM-080048.pdf

37. Marschner S.R., Westin S. H., Lafortune E. P. F., and Torrance K. E. (2000). "Image-based bidirectional reflectance distribution measurement", Applied Optics 39:16.

38. Mei X., Gunaratne M., Lu J.J., and Dietrich B. (2004) "Neural Network for Rapid Depth Evaluation of Shallow Cracks in Asphalt Pavements" Computer-Aided Civil and Infrastructure Engineering, Volume 19, Issue 3, pp. 223-230.

39. Mraz A, Gunaratne M., and Nazef A. (2005). "Guidelines for performance assessment of digital imaging systems used in highway applications", *ASCE Journal of Transportation Engineering*, Vol. 131, No. 6, June.

40. Mraz A., Amarasiri S.P., Gunaratne M., and Nazef A. (2006). "An Innovative Method for Enhancing Pavement Crack Images." Presented at the *Transportation Research Record*.

41. National Optical Institute, 2008, LRIS (Laser Road Imaging System) http://www.ino.ca/medias/pdfs/library/technical/3D-sensors/Laser_Road_Imaging_System_LRIS.pdf

42. Ngan A., Durend F. and Matusik W. (2005). "Experimental analysis of BRDF models," in *Eurographics Symposium on Rendering,* Eurographics Association, pp. 117-126

43. Peterson, W.D., and Uddin W., (1994), "Proposal of Universal Cracking Indicator for Pavements (with Discussion and Closure)", *Transportation Research Record 1455,* TRB, National Research Council, Washington D.C., pp. 69-75

44. Phong B.T. (1975) Illumination for Computer Generated Images. Communications of the ACM, 18(6):311-317, June.

45. Rado Z. (1994). A Study of Road Surface Texture and its Relationship to Friction, Doctoral Dissertation, Pennsylvania State University, PA.

46. Rusinkiewicz S. (1998) A new change of variables for efficient BRDF representation, Eurographics Rendering Workshop, pp. 11:22.

47. Shapiro L.G., and Stockman G.C. (2001), *Computer Vision*, Prentice Hall.

48. Tamura H., Mori. S, and Yamawaski T. (1978). Textural features corresponding to visual perception, IEEE Trans. Syst., Man, Cybern., vol. C-24, pp. 460-473.

49. Trucco E., and Verri A. (1998), *Introductory Techniques for 3-D Computer Vision*, Prentice Hall.

50. Wang, K.C.P. (2000) Design and Implementation of Automated Systems for Pavement Surface Distress Survey, *Journal of Infrastructure Systems,* ASCE, Vol. 6, No. 1, pp. 24-32.

51. Wang K.C.P. (2007) “Automated Pavement Distress Survey Through Stereovision”, *NCHRP Innovations Deserving Exploratory Programs Annual Report*, pp 83

52. Wang K.C.P, Hou Z., Watkins Q.B, and Quichiquilla S.R. (2007). Automated Imaging Technique for Runway Condition Survey, presented for the Worldwide Airport Technology Transfer Conference

53. Wang K.C.P., Li Q, and Gong W.G. (2007) “Wavelet-based Pavement Distress Image Edge Detection with a Trous Algorithm”, *Transportation Research Record*, Issue 2024, pp 73-81.

54. Ward, G.J., (1992) Measuring and Modeling Anisotropic Reflectance, SIGGRAPH

55. Zhou J, Huang P.S., and Chiang F.P. (2006) “Wavelet-based pavement distress detection and evaluation” *Optical Engineering*, 45(2), Art. No. 027007

APPENDICES

Appendix A Derivation of BRDF for an Aerial-View Camera

From Fig. 31, the incident light vector at R can be determined as

$$\overrightarrow{LR} = -x\underline{i} - y\underline{j} + (h-z)\underline{k} = D.\overrightarrow{LR}_u \tag{A1}$$

where ***D*** is the distance LR and $\overrightarrow{LR}_u$ is the unit vector. In order to compute the irradiance (incident light) on the camera, a transformation can be used to convert the aperture from a 3D plane circle in the (x,y,z) system to a 2D circle in the (x', y', z') system as shown in Figure A1.

If z' is normal to the aperture of the lens, then the camera plane can be identified by the unit vector $\bar{k}$ along z' defined by two of its directional cosines *l* and *m* as;

$$\bar{k} = l\underline{i} + m\underline{j} - \sqrt{1-l^2-m^2}\,\underline{k} \tag{A2}$$

Then the unit vector $\bar{i}$ can be selected such that x' axis lies on the xy plane that intersects the circle. Since $\bar{i}$ and $\bar{k}$ are perpendicular to each other (i.e. $\bar{i}.\bar{k} = 0$), the transformed $\bar{i}$ can be expressed using the original $\underline{i}$ and $\underline{j}$ as

$$\bar{i} = \frac{m}{\sqrt{l^2+m^2}}\underline{i} - \frac{l}{\sqrt{l^2+m^2}}\underline{j} \tag{A3}$$

Also since the third unit vector $\bar{j}$ is perpendicular to both $\bar{i}$ and $\bar{k}$ (i.e. $\bar{j} = \bar{k} \times \bar{i}$), the transformed $\bar{j}$ can be expressed using the original $\underline{i}$, $\underline{j}$ and $\underline{k}$ as

$$\bar{j} = -\frac{l\sqrt{1-l^2-m^2}}{\sqrt{l^2+m^2}}\underline{i} - \frac{m\sqrt{1-l^2-m^2}}{\sqrt{l^2+m^2}}\underline{j} - \left(\frac{l^2}{\sqrt{l^2+m^2}} + \frac{m^2}{\sqrt{l^2+m^2}}\right)\underline{k} \tag{A4}$$

Appendix A (Continued)

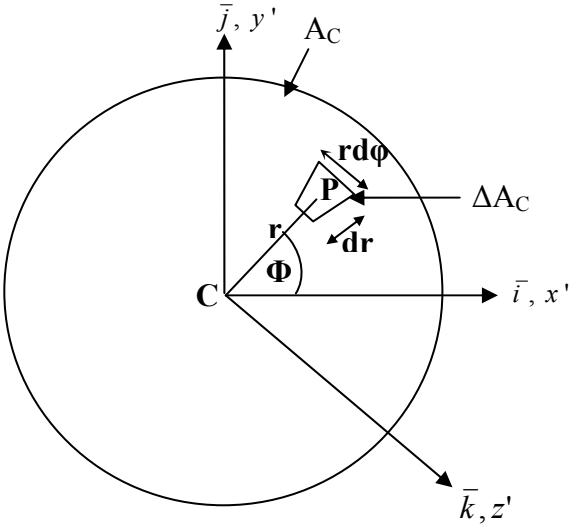

FIGURE A1 Polar and Cartesian Coordinate Systems for the Camera Aperture

Using the transformation defined by Eqns (A2)-(A4), the vector $\overrightarrow{CP}$ (Figure A1) can be represented in the (x,y,z) coordinates as,

$$\overrightarrow{CP}=\left(\frac{mr\cos\varphi}{\sqrt{l^2+m^2}}-r\sin\varphi\frac{l\sqrt{1-l^2-m^2}}{\sqrt{l^2+m^2}}\right)\underline{i}-\left(\frac{lr\cos\varphi}{\sqrt{l^2+m^2}}+r\sin\varphi\frac{m\sqrt{1-l^2-m^2}}{\sqrt{l^2+m^2}}\right)\underline{j}-r\sin\varphi\sqrt{l^2+m^2}\,\underline{k} \quad \text{(A5)}$$

Let the vector joining R and the center of the camera C (Figure A1) be,

$$\overrightarrow{RC}=C_x\,\underline{i}+C_y\,\underline{j}+C_z\,\underline{k} \quad \text{(A6)}$$

Since,

$$\overrightarrow{RP}=\overrightarrow{RC}+\overrightarrow{CP}$$

The reflected light from R to P can be represented by the following vector

$$\overrightarrow{RP}=\left(C_x+\frac{mr\cos\varphi-r\sin\varphi l\sqrt{1-l^2-m^2}}{\sqrt{l^2+m^2}}\right)\underline{i}+\left(C_y-\frac{lr\cos\varphi-r\sin\varphi m\sqrt{1-l^2-m^2}}{\sqrt{l^2+m^2}}\right)\underline{j}+\left(C_z-r\sin\varphi\sqrt{l^2+m^2}\right)\underline{k} \quad \text{(A7)}$$

Appendix A (Continued)

$\mathrm{RP} = D_C.\overrightarrow{RP}_u$

where $\boldsymbol{D_c}$ is the distance RP and $\overrightarrow{RP}_u$ is the unit vector. Then using the unit vectors in the $\overrightarrow{RP}$ and $\overrightarrow{LR}$ directions, the half vector between the incident and the reflected light (Figure 1) is defined by,

$$\vec{h} = \overrightarrow{RP}_u + \overrightarrow{LR}_u = \hat{h}.\left|\vec{h}\right| \tag{A8}$$

If the unit normal to the pavement texture profile at point $R(x, y, z)$ is specified using two known directional cosines N_x and N_y as follows,

$$\hat{n} = N_x \underline{i} + N_y \underline{j} + \sqrt{\left(1 - N_x^2 - N_y^2\right)}\underline{k} \tag{A9}$$

Then, the angular parameters required for Ward's BRDF expression (Eqn. (3)) to be applied at the surface location R can be determined as,

$$\cos\delta = \hat{h}.\hat{n} \tag{A10}$$

$$\cos\theta_i = \overrightarrow{LR}_u.\hat{n} \tag{A11}$$

$$\cos\theta_r = \overrightarrow{RP}_u.\hat{n} \tag{A12}$$

Finally, by applying Eqn. (3a) to an element of area ΔA_C of the aperture, the average BRDF at R with respect to the entire camera can be determined as,

$$\rho(x,y,z)_{avg} = \left[\frac{1}{A_C}\iint_{r,\phi}\frac{\rho_d}{\pi} + \rho_s\frac{1}{\sqrt{\cos\theta_i\cos\theta_r}}\frac{\exp\left[-\tan^2\delta/\alpha^2\right]}{4\pi\alpha^2}\Delta A_C\right] \tag{A13}$$

where $\Delta A_c = r(dr)(d\varphi)$ (Fig. A) and A_c is the area of the camera aperture.

Appendix B Relationship Between the Photo Intensities of Objects and their Images

In Fig. 32, δO is the area of the neighborhood of R from which light is reflected to the corresponding area δI of the image. The flux leaving the pavement surface area δO toward the camera is given by

$$F = L_R \delta O \delta\Omega \tag{B1}$$

where L_R is the radiance at δO. The solid angle subtended by ΔA_c on R can be expressed as,

$$\delta\Omega = \Delta A_c \frac{\cos\theta_r}{D_C{}^2} \tag{B2}$$

If no loss of photo energy is assumed within the camera, and the intensity caused by the light refracted within the element ΔA_c at the image area δI is ΔE, then

$$F = \Delta E . \delta I \tag{B3}$$

Substituting from Eqn. (B3) in Eqn. (B1),

$$\Delta E \delta I = L_R \delta O \delta\Omega \tag{B4}$$

Using Eqn. (B2), Eqn. (B4) can be rewritten as

$$\Delta E \delta I = L_R (\delta O) \Delta A_c \frac{\cos\theta_r}{D_C{}^2}$$

Or

$$\Delta E = L_R \frac{\delta O}{\delta I} \Delta A_c \frac{\cos\theta_r}{D_C{}^2} \tag{B5}$$

Appendix B (Continued)

From basic optics it follows that the light originating from an object δO and passing through the center of the camera lens (C) continues without refraction to form its image δI . Hence the solid angles subtended at the camera center C by δO and δI are equal and opposite. Then, by evaluating each solid angle one obtains,

$$\frac{(\delta O)\cos\theta_r^{/}}{D_C^{/\,2}} = \frac{(\delta I)\cos\theta_C}{(f/\cos\theta_C)^2}$$

Or

$$\frac{\delta O}{\delta I} = \frac{\cos^3\theta_C . D_C^{/\,2}}{f^2\cos\theta_r^{/}} \tag{B6}$$

where θ_C is the angle between the normal to the aperture at C and the line CR (Figure 32) and $\theta_r^{/}$ is the angle between the normal to the modeled surface and CR. Since the camera lens is relatively small in area, it can be assumed that $\theta_r^{/} = \theta_r$ and $D_C^{/} = D_C$. Therefore, by substituting in Eqn. (B5) from Eqn. (B6)

$$\Delta E = L_R . \frac{\cos^3\theta_C}{f^2} . \Delta A_C \tag{B7}$$

From Equation (1a) the reflected radiance L_R and the incident radiance L' can be related by,

$$L_R = \rho L' \cos\theta_i \Delta\omega \tag{B8}$$

where $\Delta\omega = A_L . \frac{\cos\theta_L}{D^2}$ and θ_L is the inclination of the face of the light source to the plane normal to RL

Appendix B (Continued)

Furthermore, since the attenuation of radiance is inversely proportional to the square of the distance,

$$L' = \left(\frac{h^2}{D^2} \right) L^* \tag{B9}$$

where L* is the radiance on the surface immediately below the light source Q. By combining Eqns. (B7), (B8) and (B9) one obtains,

$$\Delta E = \rho h^2 L^* \cos\theta_i . A_L . \frac{\cos\theta_L}{D^4} . \frac{\cos^3\theta_c}{f^2} . \Delta A_C \tag{B10}$$

Appendix C Use of Field Permeability Values in the Modeling of Transient and Steady-State Unconfined Seepage from a Pond into a Saturated Particulate Soil

In the conventional seepage models, the dynamic flow of water through soil pores is commonly idealized using the Darcy's law. Experimental studies show that Darcy's law may not be suited to model transient conditions and high fluid velocities that develop under excessive hydraulic gradients. Hydraulic infrastructure like retention ponds and canals almost always operate under transient flow conditions. Hence, the conventional method of analysis based on steady state seepage in a continuum must be replaced by an alternative approach that can model the transient flow that precedes the eventual steady state flow. Furthermore, seepage models for granular media must incorporate the discrete particulate nature of the soil skeleton.

Thus a confined seepage model for particulate media has been (Jeyisanker,2009) extended to analyze transient and steady-state *unconfined* seepage in a granular soil. The soil skeleton was modeled with discrete spherical particles randomly selected from a known particle size distribution (PSD) using Monte-Carlo simulation and packed to achieve a desired *in-situ* relative density. This model was used specifically to study the seepage flow from a pond into a saturated coarse-grained soil. The interstitial pore water flow initiated by sudden filling of the pond was modeled using the standard Navier-Stokes (NS) equations modified to incorporate drag forces acting on water due to soil particles. The NS equations were discretized using finite differences in time and applied to discrete elements of the soil skeleton in a staggered spatial grid. The time variation of the seepage domain was demarcated using the velocity gradient at the phreatic line.

Appendix C (Continued)

The time variation of the pond level, the phreatic line and the seepage quantity were visualized. In addition, the model prediction of the recovery time and the geometry of the phreatic surface were compared to other solutions based on continuous media and the Darcy's law.

Recovery time is defined as a length of time required for the design treatment volume in a pond to subside to the normal level or bottom of the pond. The developed model was used by the author to predict the accurate recovery time for the case study used in (Jeyisanker,2009) for a saturated particulate medium with a permeability of 6 cm/sec. The prediction results are shown in Figure C1.

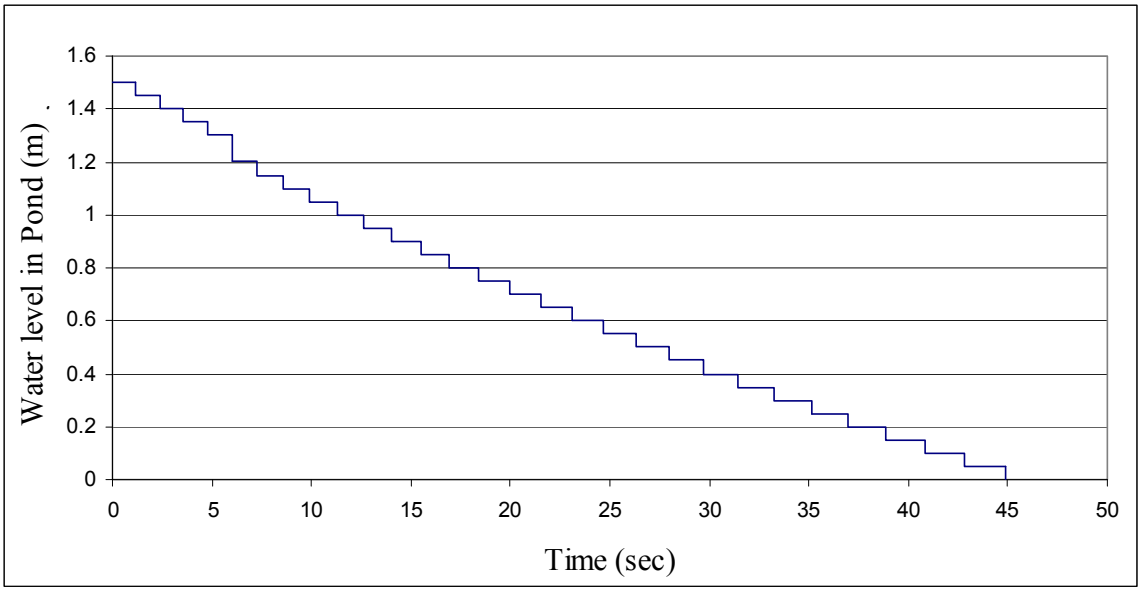

FIGURE C1 Prediction of Recovery Time from Numerical Model

Appendix C (Continued)

It is noticed from Figure C1 that the recovery time is 45 seconds for the above foundation soil. Since it is impractical to construct a retention pond in a foundation soil with such a short recovery time, to improve this soil, it was mixed with concrete and investigated as a foundation soil. Several such samples of the mixture were tested in the laboratory for permeability values. The tested samples were of ages 7, 14 and 28 days. The results were based on randomly selected population of 100 samples. The results showed that the average permeability of the 7 day, 14 day and 28 permeability values were 1.77×10^{-7} cm/sec, 3.58×10^{-7} cm/sec and 1.73×10^{-8} cm/sec respectively. The obtained values showed that there was a significant decrease in the permeability over that of the original foundation soil. Thus the recovery time of the pond would be expected to increase to more realistic values needed for retention ponds.